

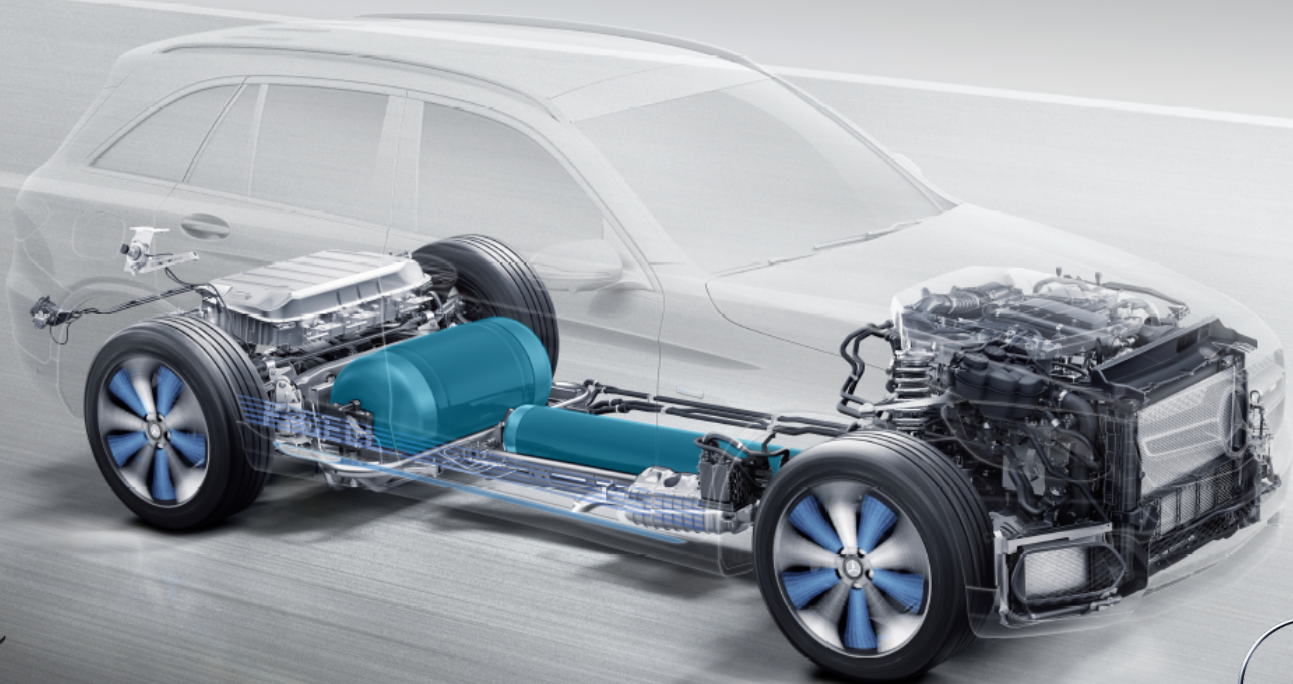
Combined Acoustic and Optic Characterization of Damage Mechanisms in Internally Pressurized Composite Pressure Vessels

Eleonora Cesari

MSc Thesis

Aerospace Engineering

Aerospace Structures and Materials



Combined Acoustic and Optic Characterization of Damage Mechanisms in Internally Pressurized Composite Pressure Vessels

by

Eleonora Cesari

to obtain the degree of Master of Science
at the Delft University of Technology,
to be defended publicly on Wednesday July 8, 2020 at 9:30 AM.

Student number:	4728084	
Project duration:	June 1, 2019 – July 8, 2020	
Thesis committee:	Dr.ir. R. de Breuker,	TU Delft
	Dr.ir. D. Zarouchas,	TU Delft
Supervisors:	Dr.ir. J.M.J.F. van Campen	TU Delft
	Dipl.-Ing. M. Nebe	Daimler AG

This thesis is confidential and cannot be made public until July 8, 2023.

An electronic version of this thesis is available at <http://repository.tudelft.nl/>.

Abstract

To achieve CO₂ emissions reductions, the automotive industries are moving towards more sustainable solutions. One of those are fuel cell electric vehicles (FCEVs) which rely on the chemical reaction of hydrogen to produce electricity. The hydrogen is stored in a gaseous and compressed form in composite pressure vessels (CPVs) which must be subjected to numerous tests for the certification. The end-of-line (EOL) test is a pressurization up to 105 MPa, compulsory for each tank before in-service life. This test could be used to quality assure the component and to verify the state of the CPV. Knowledge regarding damage formation and progression during a CPV pressurization must be obtained for the purpose. The goal of the research is to study which damage mechanisms take place and how their characteristics change when analyzing different layups. This is done pressurizing vessels with different stacking sequences in a specially designed testing chamber. During the test, optic and acoustic data are recorded. The acoustic emissions of the CPVs are detected using 120 sound pressure sensors and processed using a delay-and-sum beamforming algorithm. The optic data are analyzed with digital image correlation (DIC). The results show that only one damage mechanism takes place in the investigated pressure range (5-105 MPa). This has been identified as interfiber-fracture (IFF), happening both in the hoops and helical layers. Computer tomography scans have been used to validate the results. It is discovered that the grouping and the positioning of the hoop and helical layers has a significant influence on the acoustic behavior of the vessel. All the specimens of a layup follow a specific acoustic pattern: they have similar characteristics that can be used to associate a specimen to an analyzed stacking sequence. It has been shown that DIC has limited suitability regarding IFF detection in the hoop layers. It can identify IFF only if the hoops are the outermost plies of the laminate. However, it seems promising to predict the formation of other damage mechanisms such as IFF in the superficial helicals and delaminations. The findings contribute to a deeper understanding of the damage mechanisms taking place during an EOL pressurization. They also clarify the influence of the stacking sequence on the damage characteristics.

Preface

The current thesis has been developed to fulfill the graduation requirements of the MSc program in Aerospace Engineering (track of Aerospace Structures and Materials) at TU Delft. The research has been performed in collaboration with Daimler AG starting in June 2019. During the project I carried out detailed research on composite pressure vessels. The results are presented in the report. All this would not have been possible without the help and support of some people that I would like to thank.

First of all I would like to thank my supervisor Julien van Campen for his support through the entire process. His feedbacks and ideas have always been a valuable guidance during the project. I also want to thank Martin Nebe and Clemens Braun, the two people that gave me the opportunity to join the project. I want to express my gratitude for the knowledge they were continuously sharing and their endless patience. Their passion and commitment made me feel part of the team since the first day. I want to thank them also for the amazing atmosphere they were creating inside and outside the office and for all the laughs.

I also want to thank TU Delft and Daimler AG for making all of this possible and giving me the chance to use their facilities and resources. I want to mention Rolf Schaller, Raffaele Monda and the technicians from Daimler AG for the help in the preparation of the specimens and for performing the scans with the computer tomography.

My sincere gratitude also goes to my colleagues for the continuous support and help and the amazing moments spent together. A special thank goes to Ana for being an example and by my side in all the circumstances. You are an amazing friend. I want to also thank Tom, Daniel, Benoît, Alex, Antonio and Alejandro: the Catan games, the episodes of “The 100”, the takeaway pizzas and the fun we had at the Oktoberfest made my time in Stuttgart unforgettable. I also owe my thankfulness to my classmates in Delft and in particular to the amazing studying team for making the assignments funnier and for the international dinners we were organizing in Delft.

My biggest and most sincere gratitude goes to my family, for always believing in me. I want to thank my parents for giving me the opportunity to follow my dreams and letting me study and do my master at TU Delft. My grandma, cousin, aunt, uncle and Antonella that have always been a great support for me. And Andrea, my boyfriend, for pushing me beyond my limits and supporting me in all my decisions. I want to thank him for believing in me even when I did not and for the example he has always been for me. I also want to thank his family for making me feel part of it even these years that I was not physically close to them.

Last but not least I want to thank my friends and old classmates Fede, Fedo, Ado Jack, Fra, Jampa, Gamu and Sambu for being there with me even if hundreds of kilometers were separating us. To all these people and many others that helped me and shared a part of the path with me, thank you.

Eleonora Cesari
Delft, July 2020

Contents

List of Figures	ix
List of Tables	xiii
List of Symbols and Abbreviations	xv
1 Introduction	1
2 Literature Review	3
2.1 Composite Pressure Vessels	3
2.1.1 Definitions	3
2.1.2 Manufacturing	4
2.1.3 Application in Automotive Field	6
2.2 Structural Mechanics and Damage Mechanisms	7
2.2.1 Structural Analysis Calculations	7
2.2.2 Damage Mechanisms in Composite Materials	8
2.2.3 Damage Inspection	10
2.3 Strain Analysis	11
2.3.1 Fiber Bragg Grating	11
2.3.2 Digital Image Correlation	11
2.4 Acoustic Emissions Analysis	13
2.4.1 Acoustic Emissions	13
2.4.2 Damage Differentiation at Laminate Level	15
2.4.3 Damage Differentiation using AE Analysis in CPVs.	17
2.5 Research Questions and Objective	20
3 Methodology	21
3.1 Manufacturing	21
3.1.1 CPV	21
3.1.2 Manufacturing Process	22
3.1.3 Layups	23
3.2 Testing Facility	24
3.3 Test Preparation.	25
3.3.1 Vessel Preparation	25
3.3.2 Optical System Preparation	27
3.3.3 Acoustic System Preparation	29
3.3.4 Hydraulic System Preparation	30
3.4 Data Acquisition and Post-Processing.	30
3.4.1 Data Acquisition Process.	30
3.4.2 Optical Data Post-Processing	30
3.4.3 Acoustic Data Post-Processing	33
3.5 Damage Inspection	38
4 Results and Discussion	41
4.1 Acoustic Behavior.	41
4.1.1 Layup C	41
4.1.2 Layup F	44
4.1.3 Layup A	46
4.1.4 Layup D	49
4.1.5 Layup B	50
4.1.6 Discussion	53

4.2	Damage Differentiation Combining Acoustics and Visual Inspections	54
4.2.1	Considerations about the Time Interval of the Beamforming	54
4.2.2	Layup D	56
4.2.3	Layup B	58
4.2.4	Layup A	60
4.2.5	Layup F	62
4.3	Damage Inspection	64
4.3.1	Layup B	64
4.3.2	Layup A	64
4.3.3	Layup F	66
4.4	Damage Detection using DIC	67
4.5	Positioning and Grouping Effect	71
4.5.1	Positioning.	72
4.5.2	Grouping.	73
4.6	Final Discussion	76
5	Conclusion	81
6	Future Work	83
A	Nomenclature at Daimler AG	87
	Bibliography	89

List of Figures

2.1	Section of a CPV.	3
2.2	Vessel types [9].	4
2.3	Vessel sections nomenclature.	5
2.4	Layer types.	5
2.5	Wet winding and prepreg or towpreg winding techniques.	5
2.6	Calculated burst pressures for increasing wall thickness [12].	8
2.7	Representation of interfiber-fracture in the 90° plies [30].	9
2.8	Fiber-matrix debonding and fiber pull-out.	9
2.9	Representation of a CT station [30].	10
2.10	Cross sectional view of a tested specimen with different damage mechanisms obtained with CT [40].	10
2.11	Comparison between pressure profile and FBG data [44].	11
2.12	Facets in their original and deformed state [30].	12
2.13	Progression of a delamination and formation and saturation of matrix cracking detected using DIC [39].	13
2.14	Detection of matrix cracking using 2D DIC [55].	13
2.15	Burst and continuous type AE [62].	14
2.16	Acoustic emission features [62].	14
2.17	Summary of the results found in literature regarding damage differentiation in composite laminates using the amplitude of the AEs.	16
2.18	Interfiber-fracture due to transversal tension [30].	16
2.19	Delay-and-sum beamforming principle in time domain[42].	18
2.20	Localized and actual position of the fiber bundle breakage [8].	19
3.1	Liner dimensions.	21
3.2	Manufacturing setup.	22
3.3	Curing cycle.	23
3.4	Nomenclature of the layups of the investigation.	24
3.5	Testing facility in the Daimler plant, Untertürkheim, Germany [8].	25
3.6	Steps for the preparation of the vessel.	26
3.7	Example of speckle pattern on a CPV and quality check.	26
3.8	Example of vessel with chalk powder.	27
3.9	Steps for the preparation of the optic system.	27
3.10	Calibration panel.	28
3.11	Calibrated and not calibrated sensors.	28
3.12	Calibration body.	29
3.13	Steps for the preparation of the acoustic system.	29
3.14	Data acquisition process.	30
3.15	Steps for the processing of the optic data.	31
3.16	Pictures of six stereo-systems positioned.	31
3.17	Global coordinate system.	32
3.18	Example of a point component taken from the boss of a CPV.	32
3.19	Local coordinate system.	32
3.20	Full-field strain measurement of outer meridional strain.	33
3.21	Part of the boss used for the comparison.	33
3.22	Steps for the processing of the acoustic data.	34
3.23	Multiple peaks detected on the same emission.	35
3.24	Example of peaks detected by the PeakFinder tool.	35
3.25	Vessel mesh and emission localization example.	36

3.26 Transformation of 3D map into 2D.	37
3.27 Example of representation of the acoustic emissions in a 2D map.	37
3.28 Example of representation of the acoustic emissions with respect to its axial position and the internal hydraulic pressure of the CPV.	38
3.29 From the acoustic file to the MATLAB output.	38
3.30 Angle scale in the boss of the CPV.	39
4.1 Acoustic file of vessel C in the hydraulic pressure range 5-105 MPa.	42
4.2 Localized emissions plots for layup C.	43
4.3 Acoustic file of vessel F in the hydraulic pressure range 5-105 MPa.	44
4.4 Localized emissions plots for layup F	45
4.5 Presence of bubbles at the bottom transition zone of layup F	46
4.6 Bottom transition zone of layup F before and after the occurrence of the initial acoustic emissions.	46
4.7 Acoustic file of vessel A in the hydraulic pressure range 5-75 MPa.	47
4.8 Localization of the first detected emission for the examined vessel of layup A.	48
4.9 Localized emissions plots for layup A.	48
4.10 Acoustic file of vessel D in the hydraulic pressure range 5-105 MPa.	49
4.11 Localized emissions plots for layup D.	50
4.12 Variation of A_{max} , $P_{AE,start}$ and N_{hits} with different hydraulic pressure rates of layup B.	51
4.13 Acoustic file of vessel B in the hydraulic pressure range 5-105 MPa.	52
4.14 Localized emissions plots for layup B.	53
4.15 Example of microphones triggering for emission 4 of layup D.	55
4.16 Emission 4 of layup D: IFF location and beamforming with different time intervals.	55
4.17 Same low amplitude emission beamformed with different time intervals.	56
4.18 Acoustic file of vessel D in the hydraulic pressure range 5-105 MPa.	56
4.19 Layup D at different stages of the pressurization.	57
4.20 Beamformed emission and corresponding damage creation.	57
4.21 Acoustic file of vessel B in the hydraulic pressure range 5-105 MPa.	58
4.22 Layup B at different stages of the pressurization.	59
4.23 Beamformed emission and corresponding damage of an acoustic source of low pressure amplitude of layup B.	60
4.24 Acoustic file of vessel A in the hydraulic pressure range 5-75 MPa.	61
4.25 Layup A at different stages of the pressurization.	61
4.26 Surface comparison of layups B and A.	62
4.27 Acoustic file of vessel F in the hydraulic pressure range 5-105 MPa.	63
4.28 Layup F at different stages of the pressurization.	63
4.29 CT results of a specimen taken from a vessel with layup B after an EOL pressurization up to 105 MPa.	65
4.30 CT results of a specimen taken from a vessel with layup A after an EOL pressurization up to 75 MPa.	65
4.31 CT results of one specimen taken from a vessel of layup F after an EOL pressurization up to 105 MPa.	66
4.32 Axial displacement of the top bearing during pressurization test.	68
4.33 Full-field strain measurement of outer meridional strain of layup D at different pressure stages.	69
4.34 Full-field strain measurement of outer meridional strain of layups B, C, A and F respectively after IFF formation.	70
4.35 Full-field strain measurement of outer meridional strain of layups B, C, A and F at the maximum internal pressure.	70
4.36 High strain spot in the transition zone of layup A.	71
4.37 Pictorial representation of the seven layups of the investigation.	72
4.38 Comparison of A_{max} and $P_{AE,start}$ with different positioning of the block of hoop layers.	72
4.39 Comparison of A_{max} and $P_{AE,start}$ in vessels with different amount of hoop layers.	73
4.40 Comparison of A_{max} and $P_{AE,start}$ in vessels with different groups of helical and hoop layers.	74
4.41 Transverse failure index simulated for each couple of hoops of layup F with continuum shell approach.	75
4.42 Transverse failure index simulated for each couple of hoops of layup F with solid elements.	76

4.43 CT results of a specimen after an EOL pressurization up to 105 MPa.	77
4.44 A_{max} and $P_{AE,start}$ of the totality of the analyzed vessels.	79
A.1 Daimler AG nomenclature of the layups.	87

List of Tables

2.1	Difference in maximum sound pressure amplitude with respect to the number of hoop layers [42].	19
3.1	Material properties	22
3.2	Layups under investigation.	23
3.3	Acoustic parameters used in the PeakFinder tool.	35
3.4	Data of the specimen scanned with the CT method.	39
4.1	Maximum sound pressure amplitude recorded in the pressure range [5 - 105] MPa, hydraulic pressure corresponding to the first detected emission and detected peaks for layup C.	42
4.2	Maximum sound pressure amplitude recorded in the pressure range [5 - 105] MPa, hydraulic pressure corresponding to the first detected emission and detected peaks for layup E.	45
4.3	Maximum sound pressure amplitude recorded in the pressure range [5 - 75] MPa, hydraulic pressure corresponding to the first detected emission and detected peaks for layup A.	48
4.4	Maximum sound pressure amplitude recorded in the pressure range [5 - 105] MPa, hydraulic pressure corresponding to the first detected emission and peaks detected for the only vessel tested with layup D.	49
4.5	Maximum sound pressure amplitude recorded in the pressure range [5 - 105] MPa, hydraulic pressure corresponding to the first detected emission and detected peaks for layup B.	52
4.6	Hits detected by the PeakFinder tool when using thresholds I and II and percentage increase.	60
4.7	Maximum and residual axial displacement of the top bearing during a pressurization test.	68
A.1	Stacking sequence and nomenclature in the thesis and at Daimler AG.	87

List of Symbols and Abbreviations

Abbreviations

AE	Acoustic Emission
ASTM	American Society for Testing and Materials
BEV	Battery Electric Vehicle
BP	Burst Pressure
CAD	Computer-Aided Design
CCD	Charge Coupled Device
CFRP	Carbon Fiber Reinforced Plastic
CLT	Classical Lamination Theory
COPV	Composite Overwrapped Pressure Vessel
CPV	Composite Pressure Vessel
CT	Computed Tomography
DIC	Digital Image Correlation
EOL	End-Of-Line
ESG	Electrical Strain Gauges
FBG	Fiber Bragg Grating
FCEV	Fuel Cell Electric Vehicle
fps	frames per second
FRP	Fiber Reinforced Plastics
IFF	InterFiber-Fracture
MFP	Maximum Fuelling Pressure
NDE	Non-Destructive Evaluation
NDI	Non-Destructive Inspection
NDT	Non-Destructive Testing
NWP	Nominal Working Pressure
RGB	Red, Green and Blue
rpm	rounds per minute
SEM	Scanning Electron Microscopy
SHM	Structural Health Monitoring
UD	Unidirectional

Symbols

α	Winding angle
Δ_i	Time delay
ϵ_i	Strain in i direction
\hat{f}	Time function
μ	Average value
μ_f	Friction coefficient
ν	Poisson's ratio
σ_{\perp}	Transversal tension
τ_i	Absolute run-time
θ	Tangential coordinate
A_{max}	Maximum sound pressure amplitude in the pressure range 5-105 MPa
C	Number of circuits
c	Speed of sound
E	Elastic modulus
f_{μ}	Transverse force of fiber path
f_i	Time function of sensor i
f_n	Normal force of fiber path
G_{xy}	Shear modulus
k_g	Geodesic curvature
k_n	Normal curvature
M	Number of microphones
N_{θ}	Tangential membrane load
N_z	Axial membrane load
N_{hits}	Number of peaks
P_0	Internal pressure
$P_{AE,max}$	Internal pressure of the peak with maximum amplitude
$P_{AE,start}$	Internal CPV pressure at which the first emission above 2 Pa is recorded
r	Radial coordinate
r_0	Cylinder inner radius
r_1	Meridional radius of curvature of a dome
r_2	Circumferential radius of curvature of a dome
r_i	Distance between sensor and source
R_m	Radius of the mandrel

R_p	Radius of the pole opening
S	Shear strength
s	Standard deviation
t	Time
w_i	Microphone shading weight
w_{tow}	Tow bandwidth
X_t	Tensile strength parallel to the fibers
Y_t	Tensile strength perpendicular to the fibers
z	Axial coordinate



Introduction

Due to the current restrictions regarding CO₂ emissions [1] and the predicted increase in global passenger vehicle fleet by 2050 [2], the automotive industries need to move their focus towards more sustainable solutions. One of those are battery electric vehicles (BEVs). Aside the advantages, they present some important disadvantages, such as long recharging time and limited driving range [3]. Fuel cell electric vehicles can overcome those limitations, having a refueling time that varies between 3 to 5 minutes and a driving range up to 600 km [2]. They also show a higher energy per unit weight when compared to BEVs [4]. However, the absence of mass production and complexity of their power system cause higher operating costs, nearly twice those of BEVs [5]. The power system is formed by two main parts: the stack (where the reaction takes place) and the hydrogen storage component. The latter is a composite pressure vessel, made of fiber reinforced plastics (FRPs) (usually carbon), wrapped around a metallic or polymeric liner [6]. The hydrogen is stored in the tanks in a gaseous and pressurized state. The CPV has a key role and it is subjected to strict safety regulations [7]. Each vessel must overcome the end-of-line pressurization before its in-service life. The manufacturer needs to quality assure the component and this compulsory test can be used for the purpose. The state of the CPV can be studied during this first pressurization.

The aim of the current research is to gain knowledge about damage formation and progression of CPVs when internally pressurized during the EOL test. The effects of different stacking sequences on damage detection are also evaluated. The research is performed in the testing facility of Daimler AG, situated in the Fuel Cell department in the Untertürkheim plant, in Germany [8]. Vessels with different stacking sequences are pressurized. Optic and acoustic data are recorded during the test and post-processed using respectively digital image correlation and delay-and-sum beamforming. Acoustic and optic features are analyzed and it is studied how different stacking sequences influence them. It is also clarified whether the combination of the two chosen experimental characterization systems is suitable for the purpose and to which extent.

The current report is divided into six chapters, being the first the current one. In Chapter 2 the literature reviewed to develop the research questions is presented. A general description of CPVs is given, followed by some remarks regarding structural analysis and damage mechanics of these components. Strain and acoustic emission analysis are explained and some applications for laminates and vessels are highlighted. Lastly, the aim of the current project and the research questions are expressed. In Chapter 3 the methods used during the thesis are explained. The manufacturing technique, the testing facility and the data acquisition and post-processing are described in detail, followed by the illustration of the inspection method. In Chapter 4 the acoustic and strain results are presented and discussed. In Chapter 5 the main conclusions are drawn and the research questions are answered. Chapter 6 contains ideas regarding how to continue the current research and which other aspects might be interesting to analyze to gain a deeper knowledge.

2

Literature Review

The aim of the current chapter is to provide an overview of the literature that has been reviewed to develop the current research project. It is studied to which extent research on the topic has already been performed and which findings could be beneficial for the current project. Limitations of other existing studies have also been analyzed. They are used to point out which knowledge is still missing on the examined topics. The research questions have been shaped accordingly.

2.1. Composite Pressure Vessels

In this paragraph, some definitions and nomenclature regarding pressure vessels are provided. The two main winding techniques are explained, as well as layer types and path trajectories. The use of CPVs in fuel cell vehicles is highlighted and the tests needed for certification purposes are described.

2.1.1. Definitions

Pressure vessels are containers designed for storage purposes. They are mainly used for liquid and gaseous substances, usually kept in a pressurized state. They can be divided in five types [9] according on the materials used to produce their parts. They are formed by a liner, two bosses and the overwrapping material. The liner is the most internal part and it is the actual fluid container due to its permeability purposes. In case of filament wound vessels, it also acts as mandrel during the manufacturing. The overwrapping material, where present, is used as reinforcement to carry the loads. The bosses (usually placed at two opposite sides) are responsible for filling and emptying the vessel thanks to specific valves incorporated inside them.



Figure 2.1: Section of a CPV.

In Figure 2.1 is represented a section of one of the sub-scale vessels used for the current investigation. The three forming parts can be easily identified. This vessel is a type IV and presents a polymeric liner which is not contributing to support the internal pressure. 99% of the load is carried by the fibers of overwrapping material, while the matrix is responsible for the remaining 1% [6, 10]. Vessels of this type are used in the automotive industry for portable light weight applications. All the existing vessel types are represented in Figure

2.2.

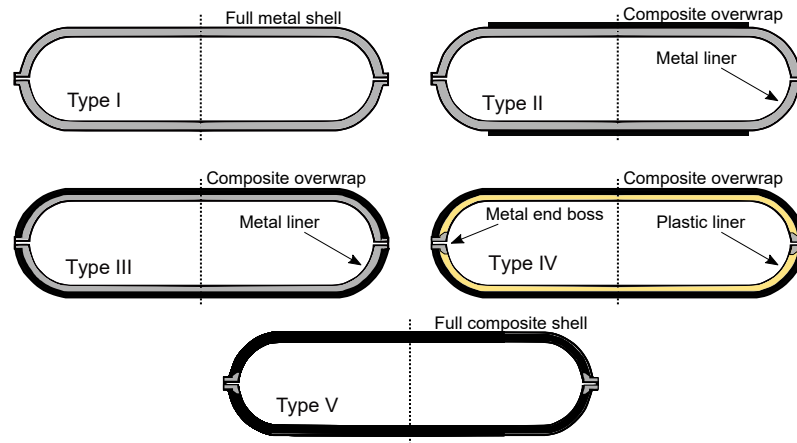


Figure 2.2: Vessel types [9].

Vessels of type I are completely metallic (generally steel) and are mainly used in the chemical industry. Types II have a reinforcement in the cylindrical section which is made of continuous filaments impregnated in resin. These are mainly used when high pressures are needed in stationary applications. Type III vessels, also known as composite overwrapped pressure vessels (COPVs), have a metallic liner, which has a sealing purpose. In this case, it also partially contributes to withstand the loads. Tanks of type III and IV are used in the automotive industries due to their low weight. Type V vessels do not have a liner, but only overwrapping material [9, 11].

Cylindrical vessels are the most common but not the only existing ones. Another example are spherical vessels. They have the lowest membrane stress on the walls when compared to vessels with same weight and different shapes [9]. Their main disadvantage is the significant volume, which makes them not suitable for all the situations. For these applications (being automotive one of those), cylindrical vessels are used. The side heads have semi-spherical or domed shapes to reduce stress concentrations. The pressure vessels of the current investigation have the latter configuration. It is possible to identify three sections of the vessel according to their geometry: cylindrical, domes and transition zones. The latter ones are the areas that link the cylindrical section with the dome regions, as shown in Figure 2.3. This nomenclature will be used in the present thesis.

2.1.2. Manufacturing

The overwrapping material of the CPVs is formed by continuous filaments (mainly carbon or glass fibers) impregnated in a resin (usually epoxy). The filaments are united in tows of variable bandwidths and wrapped around the liner. This manufacturing technique is called filament winding. It is possible to wind three types of layers, which vary according to their orientation [10]. These layers are shown in Figure 2.4 and are circumferentials (or hoops), helicals and polars. Circumferential or hoop layers are theoretically wound at 90° with respect to the vessel longitudinal axis. A slightly smaller angle is usually chosen, to avoid the perfect overlapping of the tows. They are wound only in the cylindrical section of the vessel and are responsible to carry the tangential loads. Helical layers are wrapped around the entire length of the vessel with an angle between 0° and 90° . They withstand both axial and tangential stresses in a percentage that depends on the winding angle. Parnas and Katirci [12] have theoretically evaluated that it is possible to build a thick vessel using only a single orientation of these layers, without hoops. The optimal winding angle is between 52.1° and 54.1° according to the materials used. Polar layers are a particular case of helicals: they are wound with the lowest possible angle, thus from pole to pole [13]. They are mainly used for carrying axial loads due to their configuration.

Filament winding is used to produce open cylinders or closed hollow structures (such as CPVs). The process



Figure 2.3: Vessel sections nomenclature.

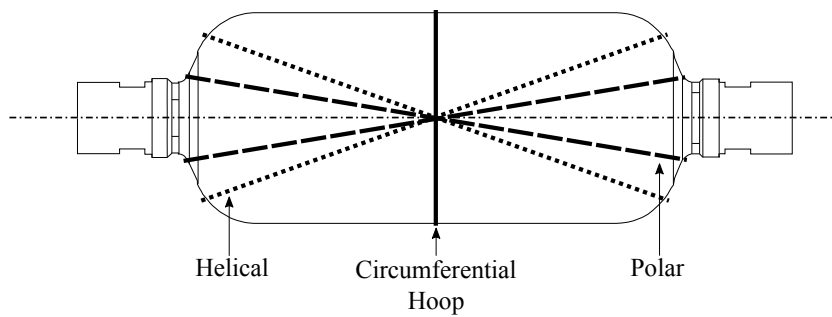


Figure 2.4: Layer types.

consists on the deposition of the fibers on a rotating mandrel which usually also displaces longitudinally. In some cases it only rotates and the rollers and the guide (shown in Figure 2.5) move horizontally. For types III and IV tanks, the metallic or plastic liner replaces the mandrel, thus the fibers are laid directly on it. The most used winding techniques are two: wet and prepreg winding [13], represented in Figure 2.5. Their differences depend on the fibers and resin used. In the wet winding technique, the fibers and the resin come separately

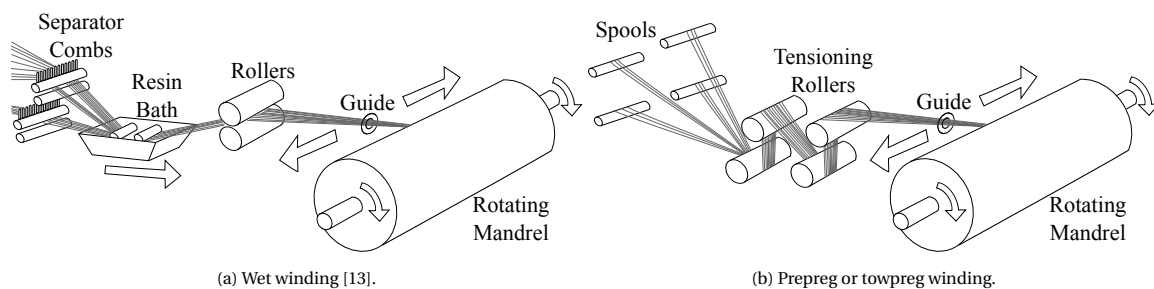


Figure 2.5: Wet winding and prepreg or towpreg winding techniques.

and are merged during the winding (Figure 2.5a). The fibers get impregnated passing through a resin bath just before being placed. In Figure 2.5b, prepreg or towpreg winding is represented, in which the resin bath is absent. The fibers come already pre-impregnated in form of spools, thus the impregnation phase is not needed. This allows a controlled resin content in opposition of wet winding. In the latter, the resin content is strongly dependent on the resin bath. Towpreg winding also has a higher placing rate making the total process faster. In wet winding the resin excess that does not stick on the fibers gets deposited on the floor and on the rollers. A constant cleaning process is thus required, while it is unnecessary when using towpregs. The main disadvantages of prepreg winding are the costs of the material and the need to store them in freezers.

This limits their shelter life which gets further reduced if they are kept at ambient temperatures [14].

During the winding, the fibers are organized into tows. Two or multiple tows can also be placed next to each other to further speed the process. To wind a helical or polar layer, the tows are placed at one side of the mandrel. This will start rotating and at the same time either the mandrel itself or the guide will move longitudinally. The fibers get deposited on the mandrel at the predefined orientation α , called “winding angle”. When the tows reach the opposite side of the mandrel with respect to the starting point, a “passage” has been wound. After the first passage, the displacement is stopped while the rotation is still activated. The latter stops when the tows are placed with the position and orientation needed to start the second passage. At this point the mandrel or the guide will displace in the opposite direction, until reaching again the starting position. When it is done, a “circuit” has been wound. The process is continued until it is reached the desired degree of coverage. The circuits (C) needed to obtain the full coverage can be calculated with equation 2.1.

$$C = \frac{2\pi R_m \cos \alpha}{w_{tow}} \quad (2.1)$$

where R_m is the radius of the mandrel, α is the winding angle and w_{tow} the total bandwidth of the tows [15]. For the circumferential layers, a coverage of 100% is not possible to reach, unless a tube is wound. When manufacturing a pressure vessel, it is not feasible to wind hoop layers in the dome regions due to their complex shape and curvature.

The different trajectories along which the tows can be placed are called winding paths. They must be carefully defined because the structural performance of the vessel is highly dependent on those. They must be precisely calculated in particular in the domes, where a double curvature is present. The winding paths are of two types: geodesic and non-geodesic. A geodesic path is defined as the connection of two points on the surface with the shortest possible trajectory [16, 17]. When the fibers are placed on the mandrel following a geodesic path, they do not tend to move, thus they are in a slip-free condition. The Clairaut law is used to define geodesic trajectories:

$$\sin \alpha = \frac{R_{op}}{r} \quad (2.2)$$

where α is the winding angle, R_{op} is the radius of the polar opening and r is the radial coordinate of the vessel at the specified point [16, 18]. Geodesic paths offer a good stability, in particular in areas with single or double curvatures. However, they limit the design possibilities, in particular in the domes. In the majority of the cases, they do not allow to have a component with the best structural performance. Non-geodesic paths can overcome this limitation [18]. They are defined as trajectories that deviate from the geodesic ones. The tows placed following these paths are not in a slip-free condition and tend to move. Friction is used to keep them in place and the slippage tendency must be lower than the friction coefficient (μ_f). The latter is defined as the ratio between the transverse force of the fiber path and the normal one [16–18], as expressed in equation 2.3.

$$\mu_f \geq \frac{f_\mu}{f_n} = \frac{k_g}{k_n} \quad (2.3)$$

where k_g and k_n are the geodesic and normal curvature respectively. The non-geodesic trajectories can be described as follows:

$$\frac{d\alpha}{dz} = \mu \left[\frac{\sin(\alpha) \tan(\alpha)}{r} - \frac{\frac{d^2r}{dz^2}}{1 + \left(\frac{dr}{dz}\right)^2} \cos \alpha \right] - \frac{dr}{dz} \frac{\tan(\alpha)}{r} \quad (2.4)$$

where z is the axial coordinate of the mandrel contour, r is the radial and α the winding angle [17]. Tension is usually applied on the fibers to avoid slippage or loose tows during winding. This helps to obtain a correct placing and pattern [19]. Towpreg winding offers the possibility to wind non-geodesic paths due to the tack of the tows. When using wet winding, the design possibilities are limited due to bands slippage.

2.1.3. Application in Automotive Field

Fuel cell vehicles are a valid solution to reduce emissions in the automotive field. They are characterized by two main parts: the stack and the hydrogen container. The fuel cell is based on a chemical reaction that

transforms the stored hydrogen into electricity [20]. The only byproducts given are heat and water [21].

Hydrogen is characterized by high energy density by weight and low energy density by volume. For this reason, it is stored and transported in a pressurized form. In automotive applications, it is kept in gaseous state and its nominal working pressure (NWP) in type IV CPVs is 70 MPa. The tank, responsible for the hydrogen storage at high pressure levels, is a key component of the FCEV. It is subjected to strict regulations set by the European Commission. Each CPV, before in-service life, must be subjected to end-of-line test: a pressurization up to 1.5 its NWP, thus 105 MPa [7]. The same regulation also predefines the minimum burst pressure (BP). For CFRPs overwrapping of type IV CPVs it is 2.25 the NWP: each tank must burst at a pressure of 157.5 MPa or higher. In case of glass fiber overwrap, the BP is 3.5 times the NWP, thus 245 MPa. The tank is subjected to continuous pressurizations and depressurizations due to refueling and driving. Fatigue tests have also been imposed by the European Commission. The regulations states that a vessel can be certified if it withstands 1,000 cycles without bursting or leaking [7]. Regulations also apply for the refueling phase. The maximum fueling pressure (MFP) is calculated as 1.25 times the NWP, thus 87.5 MPa [22].

2.2. Structural Mechanics and Damage Mechanisms

2.2.1. Structural Analysis Calculations

The understanding of the stress state of the CPV can be used to predict the formation of damage. Multiple methods have been used to calculate the different loads of pressure vessels. Some of them can be integrated with failure criteria to give critical pressures for damage formation. Each of the methods has different assumptions and accuracies, from which the applicability is in some cases limited. The four most common will be briefly explained, considering their limits and relevance.

Netting Theory

Netting theory is a relatively simple method that can be used in the preliminary design phase of overwrapped cylindrical structures. It can be used to calculate the number of plies needed to withstand predefined loads, given the fiber orientations. It assumes that the loads are totally carried by the fibers and the resin is not taken into account. No interaction between the layers is considered. It can only be applied to tubes which are considered to be subjected only to membrane loads. Shear and out-of-plane bending loads are not taken into account [23]. These assumptions make netting theory useful for a rough estimation of fiber failure, but only in the vessel cylindrical section.

Superposition of Membrane and Bending Loads with Moments

A pressure vessel is a closed structure and the influence of the domes must be considered during the calculations. In some researches [24, 25], the cylinder and the domes have been considered as separate thin isotropic entities that have later been "attached". The membrane loads are calculated for both parts using shell analysis. For a thin internally pressurized cylinder, the axial (N_z) and tangential (N_θ) membrane loads are well known and are respectively

$$\begin{aligned} N_z &= \frac{P_0 r_0}{2} \\ N_\theta &= P_0 r_0 \end{aligned} \quad (2.5)$$

where P_0 is the internal applied pressure and r_0 the inner radius of the tank [23]. The ellipsoidal domes are considered as shells of revolution with double curvature, which membrane loads can be described as

$$\begin{aligned} N_z &= \frac{P_0 r_2}{2} \\ N_\theta &= \frac{P_0 r_2}{2} \left(2 - \frac{r_2}{r_1} \right) \end{aligned} \quad (2.6)$$

where r_1 and r_2 are the principal radii of curvature of the dome, meridian radius and circumferential radius respectively. In the connection point of dome and cylinder, a discontinuity of the loads is present. Since the parts are attached, the displacements must be equal. A shear force and a bending moment must occur to solve the mismatch. This method can be used to obtain meridional and circumferential stresses in the vessel's dome and cylinder. The equations so obtained are valid only for thin isotropic structures.

Classical Lamination Theory

It is well known that composite materials are anisotropic, thus the previously described method has some limitations when applied on CPVs. These can be overcome with classical lamination theory (CLT). The plane-stress assumption makes it applicable only on thin structures and neglects the out-of-plane stresses. Perfect bonding between the layers is assumed, which results in continuous displacements through the thickness. The Kirchhoff-Love assumptions of deformation are also valid. The first one states that each straight line normal to the mid-plane stays normal and straight after deformation. The second that the laminate thickness is unchanged after the deformation. This method can be used to calculate the stresses along the vessel length to which failure criteria can be applied. This makes possible to obtain information regarding for example, critical pressure for interfiber-fracture [26] or burst pressures [12]. The CLT results could be inaccurate if applied to the CPVs used in the automotive field. Due to the important pressure they must withstand, they usually have thick walls. For this reason, the thin wall assumption of the CLT could be incorrect. Parnas and Katirci [12] used CLT and a plane-strain model to predict the burst pressure of CPVs with different wall thicknesses. As shown in Figure 2.6, the two methods provide similar results until the ratio between external and internal radii of the cylinder of the vessel is below 1.1. When this ratio increases, the predictions deviate from one another, and the CLT is highly conservative.

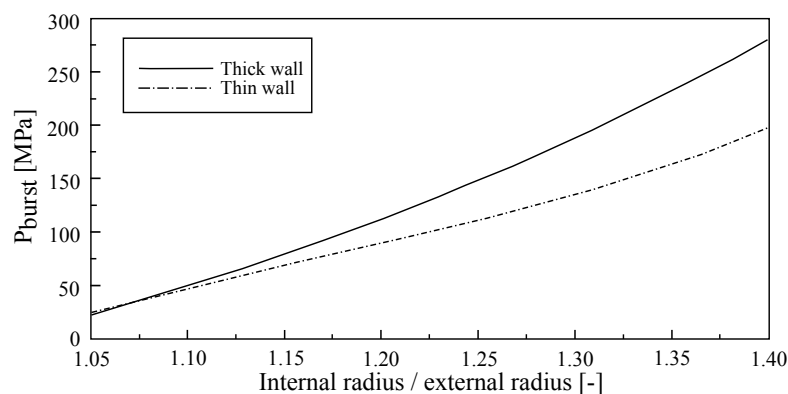


Figure 2.6: Calculated burst pressures for increasing wall thickness [12].

3D Elasticity Theory

3D elasticity theory could be a suitable method to account for the vessel thickness. Xia et al. [27] developed an exact solution for wound tubes with flat closed ends, based on 3D anisotropic elasticity. They assume that the cylinder is loaded axisymmetrically, thus the stresses and strains are independent from the hoop coordinate. It was assumed that radial displacements do not depend on the axial direction and vice versa. They obtained the exact solutions for stresses and deformations in internally pressurized thick tubes. These results could be used to gain knowledge regarding critical pressure for interfiber-fracture (IFF) or fiber failure in the cylindrical section, after applying failure criteria. They concluded that stresses and deformations are highly dependent on the vessel stacking sequence. The current solution considers the wall thickness, but it is only valid in the cylindrical section. No information about the domes is provided.

2.2.2. Damage Mechanisms in Composite Materials

Fiber reinforced materials have specific types of failure mechanisms, all of them with different characteristics. They involve matrix, fibers or both.

Fiber Failure

Fiber failure is one of the most important and severe failure mechanisms for the materials. It takes place when one or more fibers break. When few fibers fail, the loads get redistributed in the laminate, in particular in the neighboring areas. This leads to additional stresses on the surrounding fibers and consequent ruptures [28]. When a large number of loaded fibers fails, the structural failure will take place [29, 30]. This damage happens for example when tension is applied in the fibers direction [30].

Matrix Cracking / Interfiber-Fracture

Matrix cracking or interfiber-fracture is another damage mechanism that characterizes composite materials. It takes place when a crack gets formed in the resin. It is defined as “[...] formation of cracks in the matrix region between the fibers and along the interface between fiber and matrix” [30]. When it forms, it usually runs through the entire thickness of the ply and it quickly propagates through the laminate unless it gets stopped, for example, by a change in layers orientation [31]. An example is represented in Figure 2.7. Cracks usually

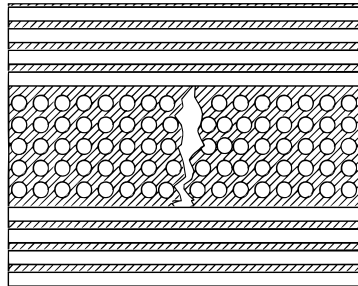


Figure 2.7: Representation of interfiber-fracture in the 90° plies [30].

start in location where stress concentrations are present. They could be voids, inclusions, air bubbles, etc. [29]. This type of failure is usually not a major damage and it is mainly responsible for the stiffness degradation of the structure. The amount of cracks increases with the loading until when it reaches a saturation state [32]. This damage can be extremely severe when a unidirectional (UD) specimen is loaded with transversal tension. For this case it can cause ultimate failure [30].

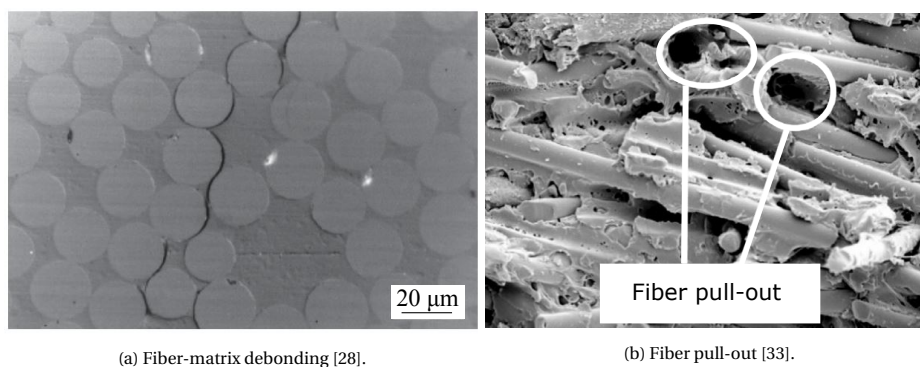
Delaminations

A delamination is a damage mechanism that takes place when adjacent plies in a laminate separate due to a crack formed at their interface [28]. It is different from IFF because the orientation of the fracture surface is opposite with respect to the thickness direction [30]. Delaminations grow through the specimen width [29]. They can be formed at the free edges or caused by defects, stress concentrations or impacts. Delaminations can sometimes grow and link two or more IFF cracks [28].

Matrix-Fiber Debonding and Fiber Pull-Out

Matrix-fiber debonding is a damage mechanism characterized by the failure of the adhesion between the two elements. An example is shown in Figure 2.8a. This failure mechanism is very detrimental for the structure, because the interface between fibers and resin is responsible for transferring the loads [28]. When the debonding takes place in multiple adjacent fibers, it can evolve and form IFF [29].

Fiber pull-out is a particular case of fiber-matrix debonding. It happens when the matrix-fiber adhesion is completely lost and the fiber gets pulled out of its socket in the resin. An example is shown in Figure 2.8b.



(a) Fiber-matrix debonding [28].

(b) Fiber pull-out [33].

Figure 2.8: Fiber-matrix debonding and fiber pull-out.

2.2.3. Damage Inspection

When testing a complex structure damage can be not easy to identify. This is the case when it takes place, for example, inside the structure or the laminate. Some techniques allow damage inspection in these situations.

One of the most used non-destructive inspection (NDI) methods is computer tomography (CT) which allows to have a 3D visualization of the structure. Multiple measurements from different angles are taken with x-rays and combined in a second step. A representation of a CT station is shown in Figure 2.9. Each picture taken

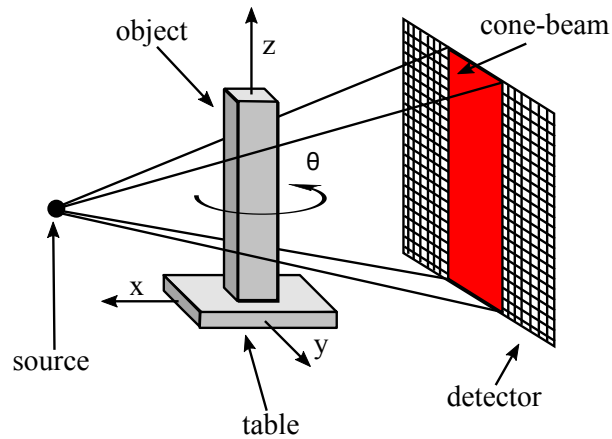


Figure 2.9: Representation of a CT station [30].

is a 2D projection of the part and it is called “slice”. All the slices get combined using image processing and reconstruction algorithms to create a 3D representation of the scanned object [34]. This technique was invented in 1973 by Hounsfield, to be used in the medical field [35]. When performing a CT scan, the part gets irradiated with x-rays which will get absorbed and attenuated. The attenuation is recorded by the detectors and it is proportional to the volumetric density of each component of the part [36]. From 1984 CT has been adapted for the industry needs such as high accuracy and necessity to obtain quantitative (not only qualitative) results. The system has a high adaptability: it can be used to inspect parts that vary from few millimeters to meters. The resolution is inversely proportional to the specimen dimension: the smaller the specimen, the higher is the resolution. Another advantage is that nearly no preparation is needed. The part to analyze must be cut only if needed (for example for resolution reasons). It is then usually glued on the surface where it is scanned to avoid movements during the scanning process.

CT has been extensively used as NDI technique applied to composite materials [37–42]. It is suitable to detect different damage mechanisms and laminate characteristics, such as porosity [30, 41, 42]. An example is represented in Figure 2.10. Here matrix cracking and delaminations can be detected. If the damage size is

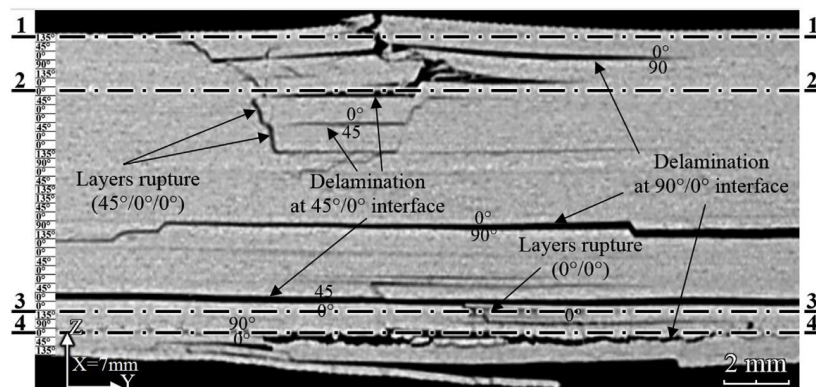


Figure 2.10: Cross sectional view of a tested specimen with different damage mechanisms obtained with CT [40].

smaller than the chosen resolution, it might be not detected and identified [41].

2.3. Strain Analysis

As already explained in Paragraph 2.1.3, CPVs must fulfill strict regulations. The manufacturing company could use the EOL test to gather information regarding the component quality. The test itself does not give any outcome unless some experimental characterization methods are implemented. The EOL pressurization test could be used to gain knowledge about damage formation, progression and differentiation in type IV CPVs subjected to internal pressure. The influence of the stacking sequence on the damage formation and progression can also be studied. The most suitable NDT (non destructive testing) techniques to obtain the data needed for the purpose must be found. Deformation measurement systems can be an example. Some examples that can be found in literature make use of fiber Bragg gratings (FBGs), electric strain gauges (ESGs) and DIC.

2.3.1. Fiber Bragg Grating

FBG systems use optical fibers to measure parameters such as strains and displacements. The optic fibers are usually embedded in the structures during manufacturing and provide punctual information. The embedment in CPVs can be challenging when wet winding is used [43]. The sensors tend to move due to the low viscosity of the resin and can easily get damaged when tension is applied to the fibers during winding. When they are placed on the surface, they provide accurate results. The outputs have been compared, for example, to the applied pressure profile [44] (Figure 2.11) or to strain gauges results. Some errors might arise if there is a misalignment between the location of the FBG and ESG sensors [45].

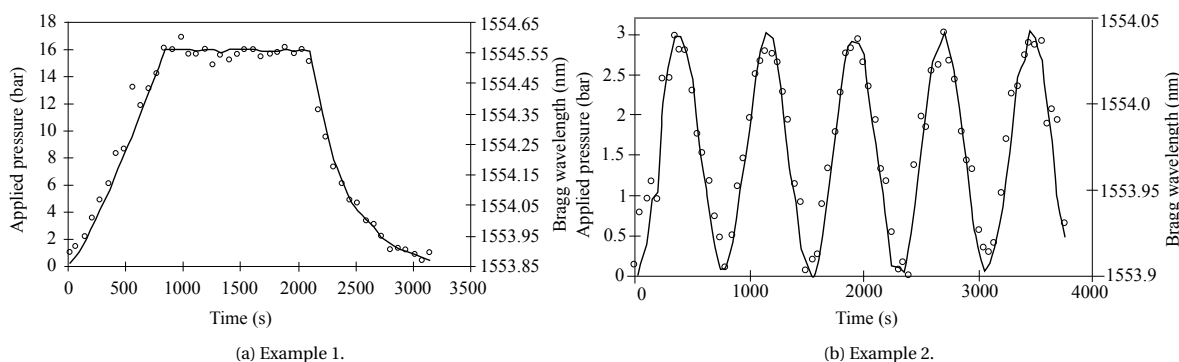


Figure 2.11: Comparison between pressure profile and FBG data [44].

It can be concluded that FBGs can be used, for example, for structural health monitoring (SHM). They are not suitable for the purpose of the thesis because they provide limited information regarding damage creation, differentiation and full-field deformations.

2.3.2. Digital Image Correlation

To have a full-field overview of the structure another characterization method must be selected. Yao et al. [46, 47] performed 2D and 3D digital image correlation on one side of a carbon fiber reinforced plastic (CFRP) vessel. They averaged the calculated superficial strains and compared them with the results obtained with ESGs applied on the same surface. The calculated error was below 5% for the 2D analysis and below 6% for the 3D. They concluded that DIC is “[...] reliable for deformation measurement of a composite pressure vessel in real engineering applications.” [46].

DIC is a contactless optical technique that provides full-field deformation of a structure or an object. It was developed in 1982 by Peters and Ranson. They compared small areas of pictures of unloaded and loaded structures using ultrasonic waves [48]. The technique progressed with Sutton and other researchers that started using pictures optically recorded [49]. DIC analysis consists in the comparison of consecutive pictures taken during the loading or unloading of a structure. The measured area is divided into smaller parts called facets or subsets. The comparison is accomplished measuring the changes in the stochastic pattern previously applied on the surface. An example can be seen in Figure 2.12. The strains are later calculated

using continuum mechanics laws [48, 50, 51]. The applied pattern is usually speckled and it is added before

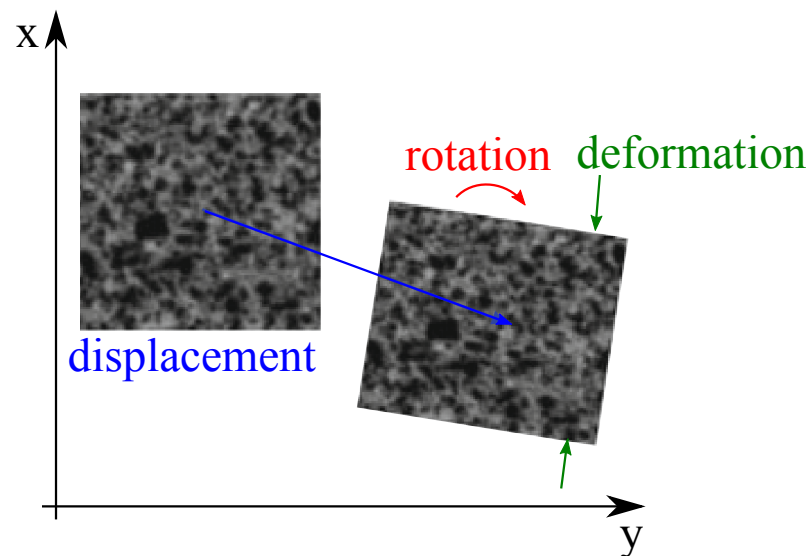


Figure 2.12: Facets in their original and deformed state [30].

testing on the surface to measure. It must be random and unique, not reflecting and with an evident contrast between the black and white part. Its coarseness depends on the cameras resolution, their distance from the part and the measuring volume [51]. It is applied with a spray or with a brush according to the needed coarseness. For the data acquisition, CCD (charge-coupled-device) cameras are mainly used. When a single camera is implemented, 2D data can be obtained, while with a couple of cameras, 3D deformations can be calculated. The first picture is taken when the specimen is still unloaded and is set as reference. The following pictures are captured during the loading and contain the information needed. The main advantage of this system is the possibility to obtain full-field deformation of the specimen. It is able to detect locally varying strains and displacements independently to the sensors location and without the need of contact [52]. The disadvantage is the need of application of the speckled pattern and the calibration of the cameras. The latter step is required to determine the intrinsic and extrinsic parameters of the sensors [51].

Yao et al. [46, 47] have proven that DIC is suitable for full-field strain and deformation investigations on CPVs. The ability of this system to detect damage and to differentiate it must be studied. This was partially proven by Rodrigues et al. [53] and Gasior et al. [54]. They both implemented defects, the first in vessels made of low carbon steel and the second in commercial type IV CPVs. They concluded that the system was able to detect and localize the simulated defects. DIC can be used to detect programmed defects in pressure vessels. It must be clarified whether it is able to identify the formation of damage and differentiate it during the first pressurization.

DIC has been used to detect and differentiate damage also at laminate level. Djabali et al. [39, 40] used it to collect strain data in thick specimens subjected to three point-bending tests. Figure 2.13 shows the strains through the thickness of the specimen at increasing bending loads. It is possible to detect the formation and propagation of the delamination (left side) as well as of transverse cracks (right side). This is an interesting outcome for the thesis investigation. However, it must be considered that filament wound structures like CPVs are closed structures. The visualization of the laminate through the thickness is not possible.

The possibility to detect damage formation analyzing the surface of the specimen must be studied. Tensile tests on laminates with multiple layups have been performed by Oz et al. [55] using 2D DIC. They confirmed the detectability of some types of damage but this was highly layup-dependent. When matrix cracking was formed on the top surface (for example testing a specimen with layup $[(90^\circ)_2/(-45^\circ)_2/(0^\circ)_2/(45^\circ)_2]_s$), it was possible to detect the IFF taking place in the top layers. This is shown in Figure 2.14. When the 90° layers were positioned at a different depth in the laminate (for example in layup $[(-45^\circ)_2/(0^\circ)_2/(45^\circ)_2/(90^\circ)_2]_s$), it was not possible to visualize IFF with DIC. Delaminations between the 90° and the 45° plies could be observed ana-

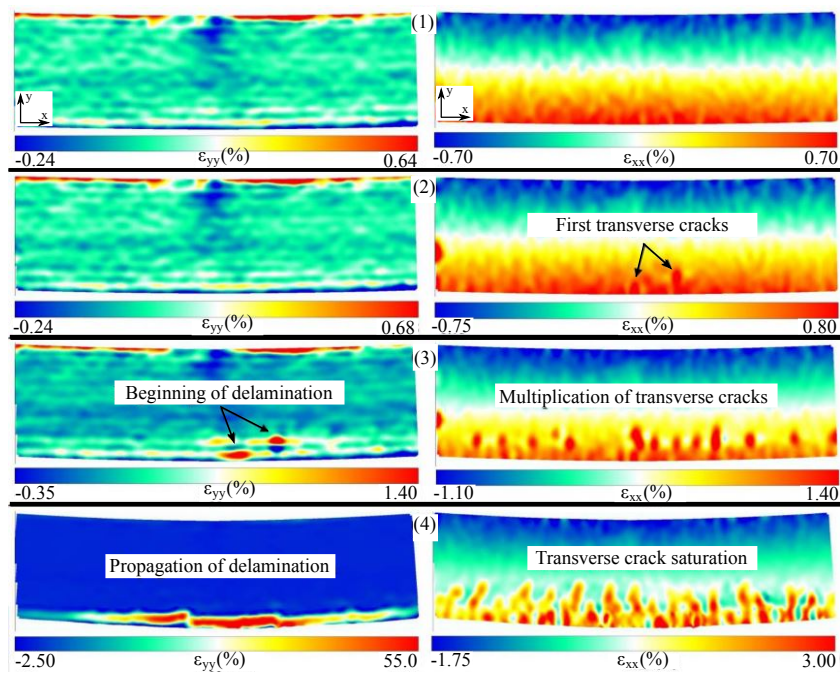


Figure 2.13: Progression of a delamination and formation and saturation of matrix cracking detected using DIC [39].

lyzing the latter layup.

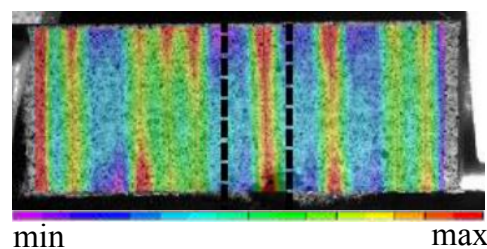


Figure 2.14: Detection of matrix cracking using 2D DIC [55].

It can be concluded that DIC is suitable to identify damage formation in laminates, but the type of damage detected is highly dependent on the layup [55].

2.4. Acoustic Emissions Analysis

The ability of DIC to identify and differentiate all damage types in CPVs is not proven yet. It might be beneficial to combine this optical NDT technique with another one, for example with acoustic analysis.

2.4.1. Acoustic Emissions

Research on acoustic analysis started in the 1920s and the first instrumentations used are from the 1930s [56]. Acoustic analysis is based on acoustic emissions (AEs). They are defined as “the class of phenomena whereby transient elastic waves are generated by the rapid release of energy from localized sources or sources within a material, or the transient elastic wave(s) so generated” [57]. When specimens or structures are loaded, they first deform elastically until when they reach the limit at which cracks take place. They cause a stress redistribution and a quick strain energy release. This generates an elastic wave that propagates through the structure. If the energy reaches certain magnitudes, the wave emits into air and can reach audible levels. This event is an acoustic emission [56]. One of the most important developments in the AEs analysis field was carried out

in the 1950s by Joseph Kaiser. He discovered what was later called Kaiser effect while testing different metals. When loading a specimen the second time, AEs could not be detected until the previous loading level was reached [58, 59]. Multiple studies were performed in the following years and AE analysis gained importance as non-destructive evaluation (NDE) technique [56, 58, 59]. It started being applied to FRPs in the 1970s and this led to the discovery of the Felicity effect [58]. This can be described as the opposite of the Kaiser effect: AEs are recorded before reaching the previous stress level [60].

Acoustic emissions can be distinguished into two types: continuous and burst or transient, as shown in Figure 2.15. Burst emissions take place when damage is formed. They have recognizable characteristics that can be attributed to a specific source type. Emissions of continuous type correspond to a superposition and merge of single burst signals. They usually take place when the damage progression in the material is fast or are caused by friction of already existing fracture surfaces. When multiple waves overlap it is not possible to identify useful parameters to characterize the source [30, 59, 61]. An acoustic emission of burst type is rep-

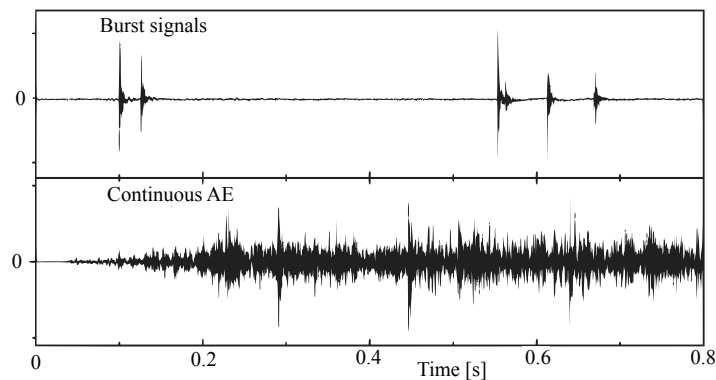


Figure 2.15: Burst and continuous type AE [62].

resented in Figure 2.16 and it is characterized by multiple features that have been defined in a standard, the ASTM E1316 [57].

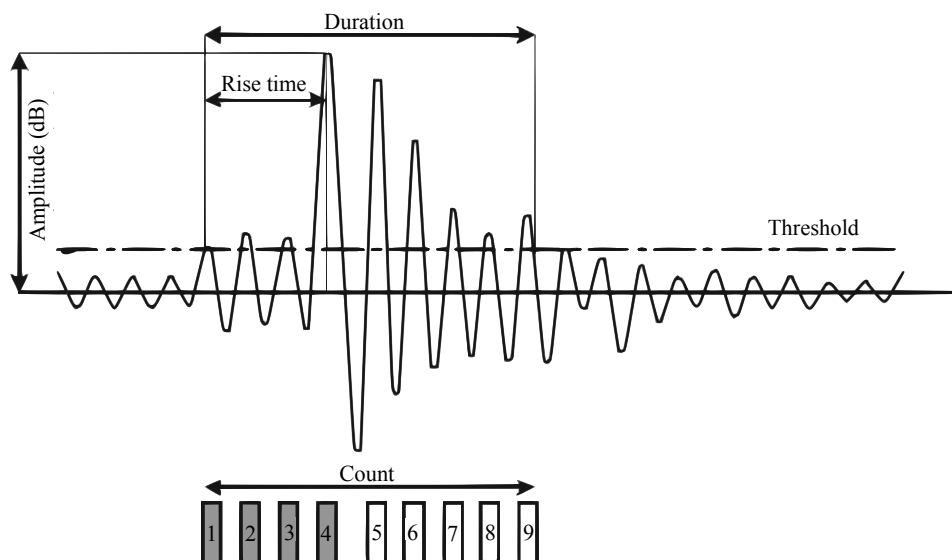


Figure 2.16: Acoustic emission features [62].

The main features are listed:

- **Event (AE event):** a local material change giving rise to acoustic emission.
- **AE signal:** an electrical signal obtained by detection of one or more AE events.

- **Voltage threshold:** a set voltage level such that signals are recognized when they exceed the specified limit.
- **Rise time:** time interval between first threshold crossing and the maximum peak amplitude.
- **Signal amplitude:** absolute value of the peak voltage of the waveform of one or more AE events.
- **Count (AE count):** number or times the AE signal crosses the predetermined threshold.
- **Duration:** time difference between the first and last threshold crossing.
- **Energy:** integral of the squared amplitude over the time of signal duration.

The suitability of AE analysis regarding damage detection and differentiation in composites must be analyzed. It must also be clarified whether different layups have an influence on the AEs features when considering the same damage mechanism.

2.4.2. Damage Differentiation at Laminate Level

Damage detection and differentiation in laminates through acoustic emission analysis has been extensively studied in literature. Different AE features have been analyzed such as amplitude [39, 40, 55, 63–69], frequency [70–73] or a combination of those [74–77]. All the literature examined, makes use of piezoelectric transducers, which are the most used sensors in AEs analysis. They are characterized by low cost, high sensitivity and ease to use [62]. They are made with piezoelectric materials (like ceramics) and are glued on the surface of the part to be tested. When the elastic waves produced by the damage reach the surface, they get in contact with the ceramic of the transducer. This will deform and produce a voltage proportional to the deformation that is amplified and detected by the measurement instrument [78].

Amplitude Analysis

The AE amplitude is one of the most studied features for damage differentiation purposes. To associate an acoustic emission to a failure type, two methods can be used. The first one is inspecting the specimen during testing, which makes possible the damage visualization during the process. The second consists in choosing a specimen that will fail with a certain mechanism due to its characteristics. An example of the first method can be found in the study from Barrè and Benzeggagh [65]. While testing a specimen, they were taking photographs with a SEM (scanning electron microscopy) microscope. They could visualize the different damage mechanisms while they were occurring. The second method was applied by Zhuang and Yan [67]. They tested five layups and each of them was characterized by a failure mechanism. A pure resin specimen was used to study matrix cracking, 90 ° UD for matrix-fiber debonding, 45 ° for fiber pull-out, 0 ° UD for fiber failure and finally ± 45 ° for delaminations.

Multiple researches have been analyzed and the results are summarized in Figure 2.17. All the studies used specimens with different characteristics in terms of dimensions, geometry, loading, fiber type, matrix type, etc. The majority of the researchers did not take into account all the five failure mechanisms, but only few of them. Comparing the different outcomes it can be concluded that damage can be differentiated taking into account the amplitude of the AEs. In the first column of Figure 2.17 the different authors are listed and in the second and third respectively the fibers and resins used during the investigation. Each type of damage is characterized by a specific color. Every author was able to differentiate the damage mechanisms and associate a range of amplitudes to each of them. No agreement is found in terms of amplitude range and damage mechanism between the authors. This is expected due to the differences in the tests performed and materials used. General guidelines cannot be obtained because the results are test dependent but few trends are observed. Matrix cracking is the damage mechanism characterized by the lowest amplitudes and fiber failure by the highest. The energy released when the two damage mechanisms take place is quite different and depends mainly on the ultimate strength and elastic modulus of the forming parts. These values are lower for the matrix, leading to a lower energy and as a consequence a low amplitude. The fibers ultimate strength and elastic modulus are higher. This leads to a higher energy release during failure and higher acoustic amplitudes [64, 66]. The other damage mechanisms have amplitudes that are between those of matrix cracking and fiber failure. It can be concluded that damage can be differentiated using AE analysis up to a certain extent. General trends regarding amplitudes ranges and associated damage mechanisms cannot be identified.

in wavefront area. This is caused by the spherical radiation of energy into the solid volume [30]. Attenuation can also take place in the far field. An example is the dissipation of the wave into adjacent media, which is, for example, the spreading caused by the fiber orientation in composite materials [68]. The free boundary effect creates a difference between the acoustics of matrix cracking taking place in the superficial or inner 90° plies. This is explained by Talreja and Veer Singh [28]. When the 90° layers are superficial, “[...] the tractions on the crack surfaces do more work in closing (or opening) the crack surfaces [...] and therefore, the perturbation complementary energy has a higher value” [28]. In general, it can be concluded that the more superficial the IFF is created, the higher is the amplitude recorded by the sensors.

Sause [30] simulated fiber failure at different depths in the laminate. He concluded that the absolute amplitudes were different. The closer to the surface the damage was taking place, the higher was the AE amplitude.

Layup Consideration

Another aspect that must be analyzed is the effect of more complex layups on the AEs. Liu et al. [69] compared the acoustic emissions generated by 3 different layups: $[0^\circ / 90^\circ]_{4s}$, $[0^\circ / 45^\circ / 90^\circ / -45^\circ]_{2s}$ and $[90^\circ / 45^\circ / 0^\circ / -45^\circ]_{2s}$. They showed that each of them had differences when comparing the number of emissions, energy and amplitudes during the loading. They attributed those to the different damage mechanisms that take place during testing. For example, the specimens with $\pm 45^\circ$ plies had a higher number of detected acoustic signals. This could be associated to delaminations and fiber pull-out effects caused by the weak interlaminar shear that those laminate presented. They were able to differentiate matrix cracking fiber-matrix debonding, delaminations, fiber pull-out and breakage according to their amplitudes.

Oz et al. [55] considered similar layups: $[-45_2^\circ / 90_2^\circ / 45_2^\circ / 0_2^\circ]_s$, $[90_2^\circ / 45_2^\circ / 0_2^\circ / -45_2^\circ]_s$ and $[0_2^\circ / -45_2^\circ / 90_2^\circ / 45_2^\circ]_s$ and used clustering algorithms to classify the different events. These are techniques that can be used to monitor multiple variables simultaneously and divide them into groups [58]. In particular, “K-means algorithm is a clustering method that assigns m input vectors (y_1, y_2, \dots, y_m) to k clusters (B_1, B_2, \dots, B_k), where each vector is allocated to the nearest cluster center.” [79]. Oz et al. analyzed multiple acoustic features and concluded that the layer orientations in the laminate have a significant influence on the cluster groups, which were highly dissimilar. The same failure mode is characterized by different acoustic characteristics according to the layup. The only common trend was the occurrence of matrix cracking in the 90° plies. In each of the three layups was the first damage mechanism taking place.

The same topic has been analyzed by Djabali et al. in two consecutive researches on more complex layups [39, 40]. A plate with UD carbon fibers prepreg with stacking sequence $[45^\circ / -45^\circ / 90^\circ / 0^\circ / 45^\circ / 90^\circ / 90^\circ / -45^\circ / 90^\circ / 90^\circ / -45^\circ / 90^\circ / 90^\circ / 45^\circ / 0^\circ / 90^\circ / -45^\circ / 45^\circ]_s$ was manufactured and specimens were cut longitudinally and transversally. It was highlighted the important influence of the loading type and ply orientation on the damage progression in the laminates. The specimen with more off-axis plies was dominated by matrix and interface failures, while the one with more on-axis plies was governed by fiber behavior. The suitability of AEs analysis on damage identification, localization and evolution has been confirmed, with some limitations.

Failure mechanisms can be differentiated using AEs amplitude, but a specific amplitude range cannot be uniquely associated to a damage mechanism. The type of sensors used, specimen geometry, fiber and matrix type and load conditions have an important influence on the final results, as shown in Figure 2.17. The layup, crack size and depth in the laminate also have an impact on the produced AEs, even for the same damage mechanism. Some trends similar in all the researches can be noticed. Emissions with lower amplitude are usually attributed to IFF, while those with higher ones to fiber failure. In complex layups matrix cracking is the first damage detected while fiber failure usually takes place at later stages. The applicability of these outcomes on more complex structures (such as CPVs) must be studied in detail.

2.4.3. Damage Differentiation using AE Analysis in CPVs

One of the most recent and complete investigations on the topic has been performed by Liao et al. [79]. They performed stepped pressurization on commercial automotive type IV CPVs. The EOL pressure was reached first (105 MPa) and the minimum BP (158 MPa) after. Piezoelectric transducers were used to record the acoustics. Liao et al. [79] considered three AE features: amplitude, energy and frequency and implemented a k-means algorithm. For the described case, the input vectors are AE amplitude, energy and frequency. The

clusters represent the different damage mechanisms, being matrix cracking, fiber-matrix debonding and fiber failure. Matrix cracking was the first damage taking place, at load levels between 30 and 50 MPa. Low amplitudes and energies have been associated to this damage. Signals related to fiber failure had the highest energy and amplitude and appear at pressure stages close to burst (158 MPa). Fiber-matrix debonding was placed between the two other failure mechanisms. This research has confirmed that AE analysis is suitable to detect and differentiate damage in CPVs. The influence of the vessel stacking sequence has not been investigated yet.

Nebe et al. [8] also performed pressurization tests on a type IV CPV. To gather the acoustic data they did not use piezoelectric transducers but sound pressure sensors. A delay-and-sum beamforming algorithm has been implemented to post-process the data. This technique gives the possibility to analyze the acoustic of a scene, giving as result a visual map in which the acoustic sources are identified [80]. This system is completely contactless. The acoustic of the scene is recorded through multiple sensors, positioned in a predefined layout. The location of the acoustic source can be defined analyzing the runtime delays of the wave with respect to each sensor [80]. A representation of the working principle of the delay-and-sum beamforming in time domain is shown in Figure 2.19. It can be explained as follows:

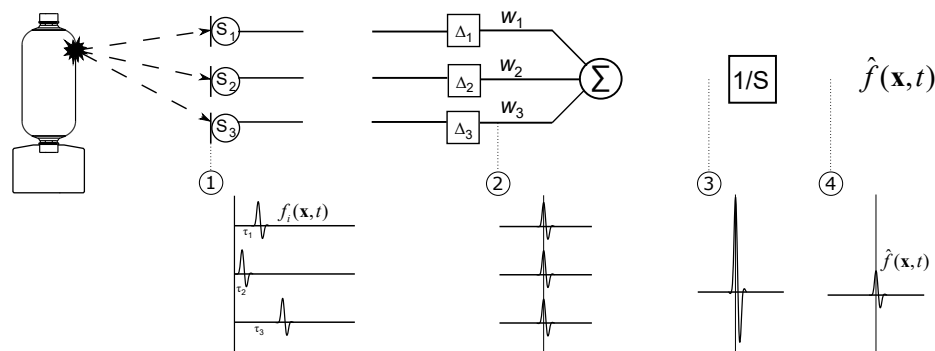


Figure 2.19: Delay-and-sum beamforming principle in time domain[42].

1. When the acoustic source is produced it reaches the sensors with different paths. The sensors detect the signals at different times, with a delay that depends on the covered distance. The absolute run time can be calculated taking into account the distance of a sensor (r_i) and the speed of sound in air (c) with equation:

$$\tau_i = \frac{|r_i|}{c} \quad (2.7)$$

2. The time delay of each sensor can be calculated from the total run time as follows:

$$\Delta_i = \tau_i - \min(\tau_i) \quad (2.8)$$

3. The signal of each sensor is shifted by the corresponding delay and multiplied by the shading weights w_i , which are microphone specific. The signals are now in phase and can be summed.
4. The signal is then normalized by the amount of sensors and the reconstruction of the time function \hat{f} of a point $\mathbf{x} = (x', y', z')^T$ is calculated with Equation 2.9.

$$\hat{f}(\mathbf{x}, t) = \frac{1}{M} \sum_{i=1}^M w_i f_i(\mathbf{x}, (t - \Delta_i)) \quad (2.9)$$

where t is time, M is the number of sensors, w_i are the shading weights, f_i are the time functions recorded by each microphone and Δ_i the relative time delays [80, 81].

Nebe et al. [8] performed a pressurization test of one type IV pressure vessel. They stopped the pressurization at a load corresponding to 90% the burst pressure. The focus was on two major acoustic event that took place

at the end of the test. They were reaching sound pressure amplitudes above 100 dB. They were localized by the beamforming algorithm at the top and bottom of the cylinder, close to the transition zones. They observed the tested vessel and found that the events corresponded to fiber bundle breakage of the outermost helical layer. They also showed that the accuracy of the localization was high, as it can be observed in Figure 2.20.

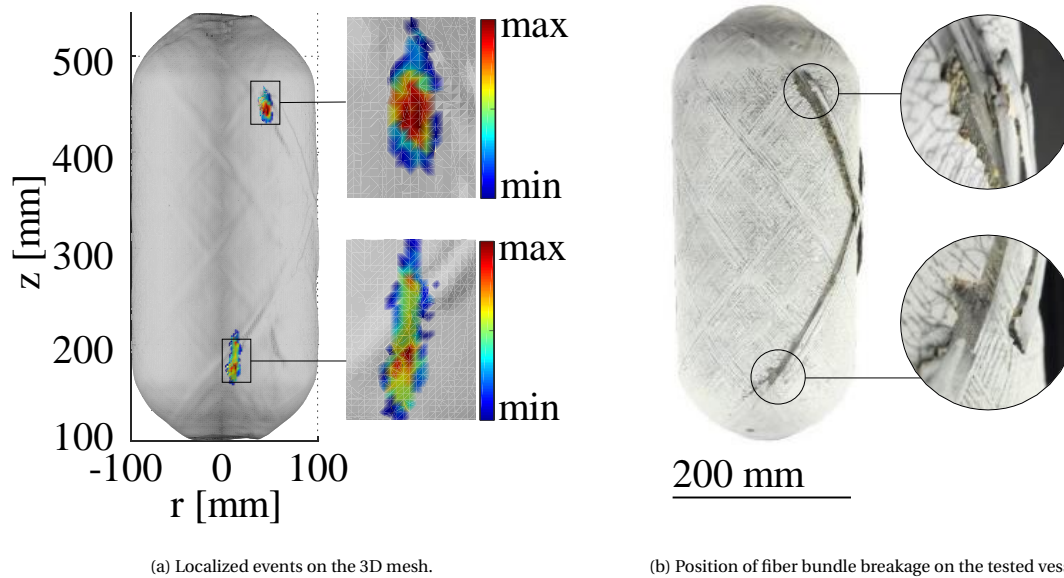


Figure 2.20: Localized and actual position of the fiber bundle breakage [8].

Torres Guijarro [42] performed pressurization and burst tests on CPVs in the same facility used by Nebe et al. [8]. She focused her research on the emissions taking place at earlier pressure stages, in the range 15-75 MPa. She concluded that they can be associated with IFF, which is in agreement with Liao et al. [79] findings. She showed that the number of emissions, their amplitude and the internal pressure at which they occur are layup-specific. Within a layup, these characteristics and patterns are followed by all the specimens. She also concluded that the number of circumferential layers has an influence on the sound pressure amplitude that is linked with the crack fracture surface. Comparing layups A and B which have the same stacking sequence except for the amount of hoop layers (30 for A and 23 for B), she showed that there is a substantial difference in the maximum sound pressure amplitude, as shown in Table 2.1. This is in agreement with what discovered at laminate level by Prosser [68] and Sause [30].

Table 2.1: Difference in maximum sound pressure amplitude with respect to the number of hoop layers [42].

Layup	Number of hoop layers	A_{max} [Pa]	Number of samples
A	30	20.6 ± 3.2	6
B	23	11.5 ± 1.3	7

It can be concluded that AE analysis is suitable to gather information regarding damage creation and differentiation in CPVs, when using piezoelectric transducers [79]. The current investigation will take place in a testing facility in which it is implemented a system used to perform delay-and-sum beamforming analysis. This facility will be explained in Paragraph 3.2. The suitability of this system to differentiate damage mechanisms must be investigated. It has been proven that delay-and-sum beamforming is appropriate to localize superficial damage and to detect IFF in composite tanks. With this method it is also possible to identify differences in the acoustic behavior of vessels when analyzing multiple layups [42] taking into account the sound pressure amplitude. The research in the latter field is just at the beginning. A limited amount of layups have been analyzed and clear and precise conclusions cannot be drawn yet. Further research on the damage dif-

ferentiation using delay-and-sum beamforming on CPVs is needed.

2.5. Research Questions and Objective

From the literature reviewed it can be concluded that the application of damage differentiation to CPVs is not mature yet. DIC has been proven to be a reliable method for strain measurements and damage detection in laminates when the layup is known. Literature on the effects of the layup on DIC measurements could not be found. The topic should be further investigated.

Acoustic emission analysis using piezoelectric sensors has been proven to be suitable for damage detection and differentiation. Delay-and-sum beamforming also seems a promising method when applied to complex structures. Research on the topic is just at the start. The damage differentiation using AE analysis can be challenging when multiple damage mechanisms have overlapping acoustic features. A combination of multiple characterization systems can be a solution.

The aim of the current project is to determine whether it is possible to detect, localize and differentiate damages in type IV CPVs during an EOL test. Knowledge about damage formation and progression can be used to differentiate those detrimental from the less severe ones. The influence of the vessel stacking sequence is also studied. A combination of 3D DIC and delay-and-sum beamforming will be used for the purpose. The tests will be performed in a specially designed testing facility which will be explained in paragraph 3.2. Multiple sub-scale vessels with different stacking sequences will be manufactured and tested. The layups will have different grouping and positioning of the helical and hoop layers, which will be described in detail in Paragraph 3.1.3.

The research questions formulated for the current project are the following:

- How can acoustic features (e.g. maximum sound pressure amplitude) be associated to certain layup characteristics during an EOL pressurization of a CPV?
 1. Which relation exists between the depth of interfiber-fracture and the maximum sound pressure amplitude?
 2. What is the effect of the size of the interfiber-fracture that has formed on the maximum sound pressure amplitude?
- With what accuracy can a combination of DIC and AE using delay-and-sum beamforming characterize and differentiate damage mechanics during pressurization of a CPV?

3

Methodology

In this chapter, information regarding the methods used during the project will be provided. The layups investigated will be explained, as well as their manufacturing. The testing facility will be described and it will be clarified how each system (hydraulic, optic and acoustic) is prepared for testing. The data acquisition and post-processing are also described in detail. At the end, the damage inspection method used (CT) is shown.

3.1. Manufacturing

Sub-scale type IV CPVs are used for the current project. They are manufactured by the student using the prepreg winding technique in a winding facility present in the Daimler AG plant, Untertürkheim, Germany.

3.1.1. CPV

The CPVs used for the current investigation are formed by composite materials wrapped around a polymeric liner, made of polyamide 6. The liner is manufactured by an external company using injection molding. It has a cylindrical section and two half-ellipsoidal domes at the sides to which aluminum bosses are attached. The storage volume in the unpressurized state is 8.6 L and its dimensions can be seen in Figure 3.1. The over-

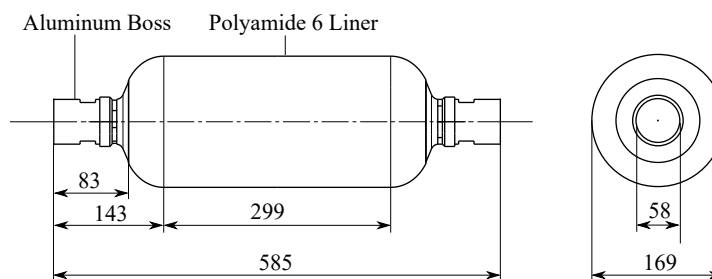


Figure 3.1: Liner dimensions.

wrapping material of the CPV is made of CFRP. In particular carbon fibers of the type T700S (Toray, Tokio, Japan) act as reinforcement of the epoxy resin. The fibers are already preimpregnated with the matrix. They are provided by the manufacturer in form of tows wrapped in bobbins.

The material parameters have been obtained with tests on UD coupons, manufactured with the same technique of the CPVs. Tensile tests have been made parallel and perpendicular to the fiber directions to obtain the tensile strength and elastic modulus in both directions. Shear tests have not been performed, thus values from literature are taken and indicated with *. The tests have been performed externally using the norm DIN EN ISO 527-5. The material characteristics can be seen in Table 3.1.

Table 3.1: Material properties

	Fiber Volume Fraction [%]	X_t [MPa]	Y_t [MPa]	S^* [MPa]	E_x [GPa]	E_y [GPa]	ν_{yx} [-]	G^*_{xy} [GPa]
Hoop	56.7	2350.23	29.26	70	126.26	7.47	0.32	4.00
Helical	54.4	2254.90	28.10	70	121.13	7.17	0.30	4.00

3.1.2. Manufacturing Process

The manufacturing technique used to produce the CPVs is filament winding and in particular prepreg winding. The manufacturing is performed using a six-axis robot (KUKA Roboter GmbH, Augsburg, Germany). The liner is clamped in the robot and acts as mandrel for the winding process. It rotates and displaces in the three directions. A pressure of 1.5 bar is applied during the winding to avoid liner deformation and buckling. The wrapping material is positioned in a cabinet. Four bobbins are used simultaneously for each CPV. They are clamped on rotating cylinders which are linked to a tensioning system that works creating a torque on the bobbin itself. A tension level can be set to each tow. The four tows pass through a predefined layout of rollers which allows the proper placing of the tows with respect to each other. They are then linked on the eyelet, where the final band that will be applied on the mandrel is formed. The manufacturing setup used can be seen in Figure 3.2.



Figure 3.2: Manufacturing setup.

The two kinds of layers used during the manufacturing process are helicals and circumferentials, which are defined through the orientation of the fibers, as described in Paragraph 2.1.2. The circumferential layers are wrapped only in the cylindrical section, while the helicals along the entire geometry of the vessel. In the transition zone, the hoops layers are tapered to avoid the formation of a gap between the top and bottom blocks of helicals. The circumferential layers are wrapped with a tension of 20 N, while the helicals with 50 N. Depending on the layout, the winding time varies from 2.5 to 3 hours. When the process is finished, the vessel is placed in an oven for curing, horizontally oriented. During the curing process, an internal pressure of 2 bar is applied to avoid the shrinking of the liner. The vessel is clamped at the bosses to a mechanism that allows the rotation of the vessel along its longitudinal axis for the entire process. This is made to have constant heating in all the sides and to avoid resin rich areas at the bottom due to gravity. The rotation is at an angular speed of 10 rpm. The curing cycle of the vessel is decided taking into account the manufacturer's specification curing cycle and the thickness profile of the CPV and it is set at 110 ° C for 8 hours. The heating phase from room temperature to the curing temperature happens in 60 minutes, while the cooling needs other 8 hours. The

curing cycle of the vessel can be seen in Figure 3.3.

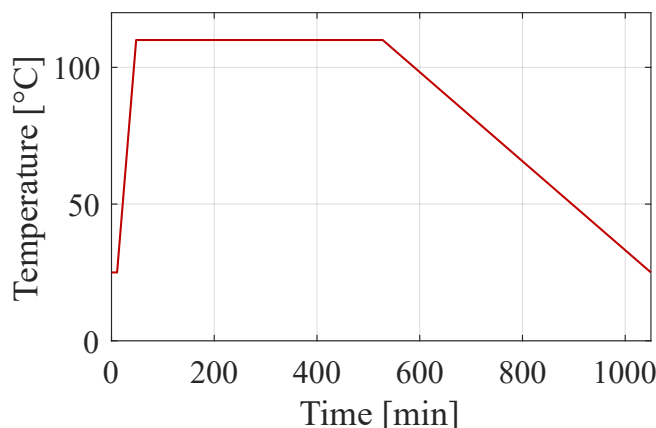


Figure 3.3: Curing cycle.

3.1.3. Layups

The winding pattern needs to be defined before starting the winding process. A winding simulation software (ComposicaD) is responsible for its creation. In the software it is possible to define the type of layer, the winding angle, the coverage and the pole opening (up to a certain extent). The fixed width of the bands makes not possible to obtain a coverage of 100% in all the cases. Sometimes, more circuits are wound giving a coverage varying between 100% and 103%. Since the circumferential layers are wound only in the cylindrical section, whenever passing from a helical to a circumferential and vice versa, it is necessary to connect the end of the previous ply with the starting of the new one. A layer called connector is wound and it is automatically included by the ComposicaD software. This layer is also needed to avoid sharp changes of direction when passing from a layer type to the other due to the important difference of winding angle between the two.

Five layups have been investigated for the current research and the results of other two (B* and E) were available, so have been used for drawing conclusions and observing trends. All the stacking sequences are described in Table 3.2. The angles are calculated with respect to the longitudinal axis of the vessel, thus being

Table 3.2: Layups under investigation.

Layup	# Layers	Stacking Sequence
A	52	$[(\pm 19.9^\circ)(+88.5^\circ, -88.5^\circ)_{15}/(\pm 19.9^\circ)_{10}]$
B	52	$[(\pm 19.9^\circ)_9/(+88.5^\circ, -88.5^\circ)_{15}/(\pm 19.9^\circ)_2]$
C	52	$[(\pm 19.9^\circ)_{10}/(+88.5^\circ, -88.5^\circ)_{15}/(\pm 19.9^\circ)]$
D	52	$[(\pm 19.9^\circ)_{11}/(+88.5^\circ, -88.5^\circ)_{15}]$
E	52	$[(\pm 19.9^\circ)_5/(+88.5^\circ, -88.5^\circ)_7/(+88.5^\circ)/(\pm 19.9^\circ)_5/(+88.5^\circ, -88.5^\circ)_7/(+88.5^\circ)/(\pm 19.9^\circ)]$
F	52	$[(\pm 19.9^\circ)_2/(+88.5^\circ, -88.5^\circ)_3/(\pm 19.9^\circ)_2/(+88.5^\circ, -88.5^\circ)_3/(\pm 19.9^\circ)_2/(+88.5^\circ, -88.5^\circ)_3/(\pm 19.9^\circ)_2/(+88.5^\circ, -88.5^\circ)_3/(\pm 19.9^\circ)_2]$
B*	45	$[(\pm 19.9^\circ)_9/(+88.5^\circ, -88.5^\circ)_{11}/(+88.5^\circ)/(\pm 19.9^\circ)_2]$

0° a layer theoretically wound parallel to it and 90° a circumferential ply. The given layups describe the fibers orientation only in the cylindrical section of the CPV because no circumferentials are wound in the domes. The ellipsoidal shape of the domes does not allow to have a constant winding angle for the helicals, thus it changes continuously along the fiber path. As a result, each axial coordinate in the domes will present a different winding angle. This also changes at the same axial position when considering two subsequent plies. The thickness buildup, radial coordinate and the different pole openings cause these differences. The fibers orientation for each layer and at each position is provided by ComposicaD.

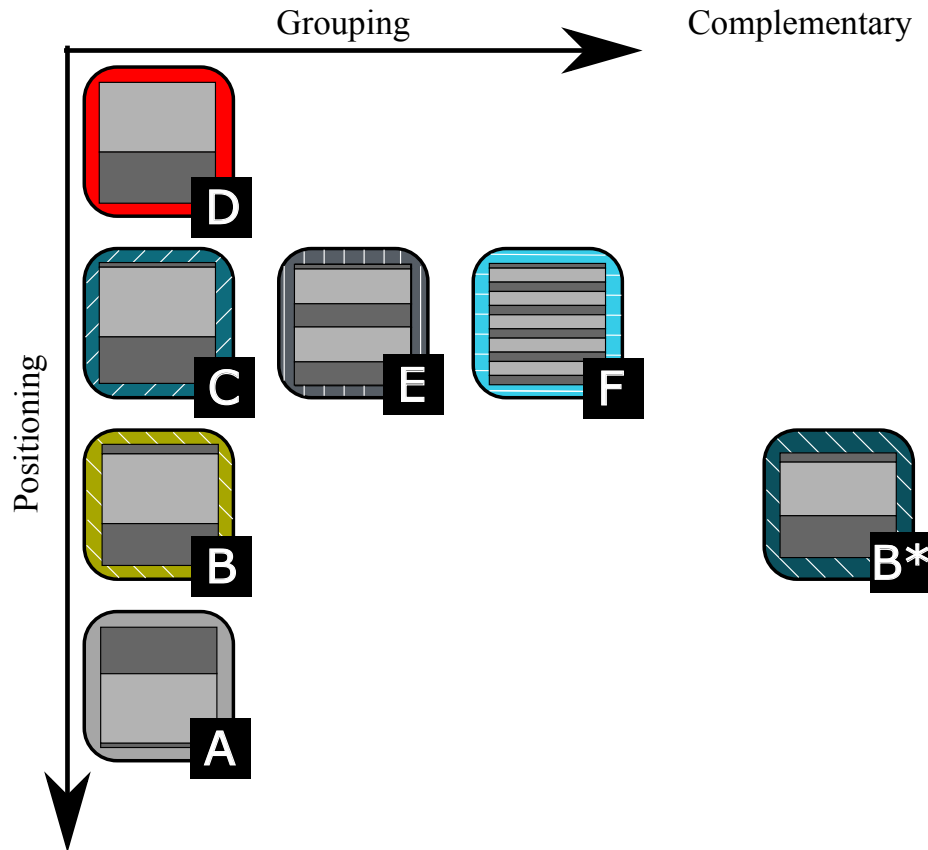


Figure 3.4: Nomenclature of the layups of the investigation.

Figure 3.4 shows a pictorial representation of the stacking sequences of the vessels analyzed in the current project. The nomenclature is provided in the black box below each layup. The dark gray corresponds to the helical layers, while the light gray to the circumferentials. The background color and pattern will be used in some future figures and/or graphs to identify the stacking sequences. All the layups (except B*) are characterized by the same number of hoops and helicals positioned and grouped differently. Layups A to D are characterized by a single block of hoops in which only its position through the laminate thickness is changed. Layups C, E and F differ on the amount of groups their hoops are divided in, being respectively one, two and five. Layup B* is a particular case of layup B, characterized by seven less hoops.

Each layup has a different thickness profile. Since all the layups (except B*) have the same number of plies, the difference can be observed mainly in the domes and transition zone. The thickness profile at each position is provided as an output of the software CompositicaD. It is calculated from the input given in the software, thus it represents the theoretical thickness profile. This can differ from the real one, because it does not take into account fiber slippage, compaction due to applied tension and possible deformation of the mandrel during the winding.

3.2. Testing Facility

The testing facility used for the investigations is situated in Untertürkheim, in the Daimler AG plant in Germany. This testing chamber, visible in Figure 3.5 has been designed to perform burst tests on pressure vessels. It has a hexagonal shape made of 70 mm thick steel walls. For pressurizing the vessel, a hydraulic pump is used and it can provide variable pressure rates. The pressure data is acquired with a sampling frequency of 1 kHz. In order to perform a test, the vessel is clamped at the upper and lower boss through a floating locating bearing arrangement. The bottom locating bearing is fixed and allows the attachment of the vessel to the hydraulic joint. The top boss is clamped in a floating bearing that allows the vessel to axially displace when pressurized. In addition, on three of the sides of the chamber, arranged every 120° along the circumference,

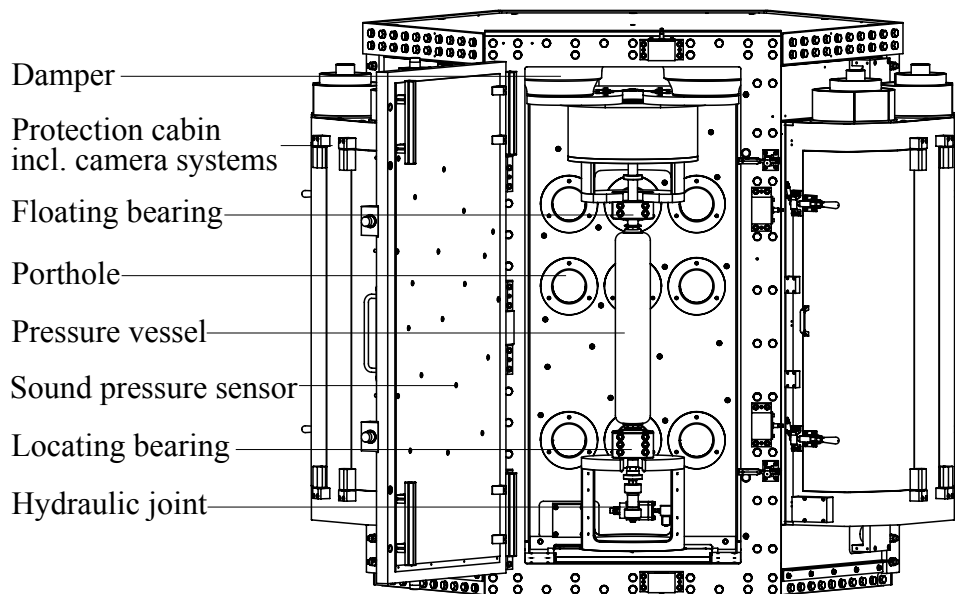


Figure 3.5: Testing facility in the Daimler plant, Untertürkheim, Germany [8].

cameras are placed inside protection cabins. The cameras can take pictures through round portholes and are protected with 82.5 mm thick acrylic glasses. Three stereo cameras are positioned in each cabin, at three height levels: bottom, middle and top. In total nine stereo systems with 18 cameras can be used. Each camera has a resolution of 1624 x 1234 pixels and the maximum frame rate is 10 frames per second (fps). The cameras can be used to perform a 3D digital image correlation analysis of the vessel during the pressurization, as well as to obtain a 3D model of the vessel through stripe light projection. This is possible due to the presence of a projector in the porthole in between two cameras. In addition, 120 sound pressure sensors for recording acoustic events are positioned inside the chamber on the six lateral walls. The sound pressure sensors are arranged in such a way that minimizes aliasing effects. In total 20 sensors are installed in each wall and they all have a unique identification number. The sensors can record acoustic signals with a sampling frequency of 48, 96 or 192 kHz. This must be chosen accordingly to the length of the file to record, due to limited amount of memory. The sensors are used to record acoustic events and through the usage of a time domain delay-and-sum beamforming algorithm, it is possible to localize acoustic events. For the localization, the software NoiseImage (gfai tech GmbH, Berlin, Germany) is used.

3.3. Test Preparation

Before performing a pressurization or a burst, some steps must be taken to prepare the vessel and the systems for the tests. They will be explained in Paragraphs 3.3.1, 3.3.2, 3.3.3 and 3.3.4.

3.3.1. Vessel Preparation

Before being tested a vessel is subjected to five main operations. Three of them are needed for the optical data acquisition, the fourth one is the filling of the vessel (to avoid the presence of air during the testing) and the last one is the clamping in the locating bearing in the burst chamber. The steps for the vessel preparation can be visualized in Figure 3.6.

The first step consists in the creation of a speckled pattern on the CPV. The CPV is first sprayed with a water-based white paint and let dry for approximately one hour. Then, the speckled pattern is applied with a brush. The brush is first dipped into black paint and then the excess color is removed. Afterwards, the brush is tapped on the vessel surface, paying attention not to slide it. The black paint must be randomly applied and the pattern unique. The pattern should not be neither too sparse or too dense and the size of the speckles depends on the cameras resolution, the measuring volume and the distance of the vessel [51]. After the paint is applied on the entire surface, it must dry for at least 2 hours. An example of a CPV with the speckle pattern

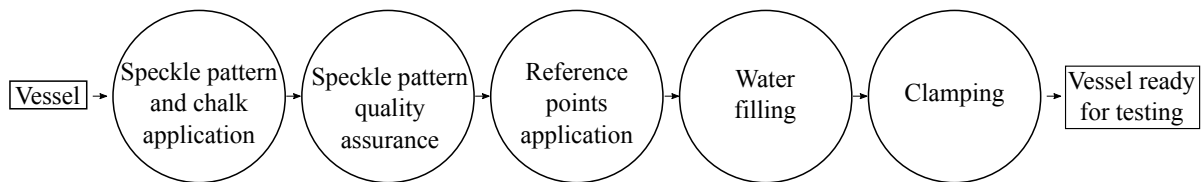


Figure 3.6: Steps for the preparation of the vessel.

applied can be seen in Figure 3.7a. The brush and the paints are provided by GOM (GOM GmbH, Braunschweig, Germany).

The next step consists in the quality assurance of the applied speckle pattern. The vessel must be clamped in the same position it will be placed during the testing. Pictures from each stereo system must be taken and imported in the post-processing software GOM Correlate Professional. The built in function “Pattern Quality” must be activated and it will automatically show the quality of the speckle pattern, being green a good pattern, yellow an acceptable one and red corresponding to low quality. If the quality is not high enough, the software will not be able to perform DIC in the area. An example of an excellent pattern quality can be seen in Figure 3.7b.

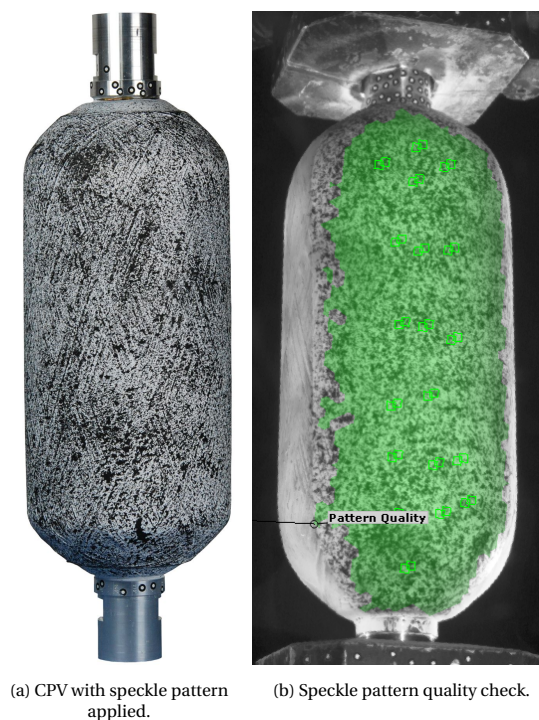


Figure 3.7: Example of speckle pattern on a CPV and quality check.

After the speckle pattern application and check, another step must be done to gather more information during the testing. In order to track the axial deformation of the entire vessel, it is necessary to apply some reference points that the software for the post-processing is able to recognize. These points are also provided by GOM and are attached at the top and bottom bosses, as it can be seen in Figure 3.7.

The last step needed before testing is the filling of the vessel, to avoid the presence of air inside. This is done plugging at the bottom and top of the vessel two tubes. The top one allows the exit of air while the bottom one is connected with the pump. The filling is slow to avoid the creation of a pressure state in the vessel.

While the created speckle pattern allows for full-field strain measurements, the applied paint makes the identification of microdamage on the outer layers impossible. Therefore, the outer surface of an additional set of

vessels has been prepared with chalk powder. The powder is sprayed on the vessel and let dry for 20 minutes. An example of vessel with chalk powder applied can be seen in Figure 3.8. When superficial damage is cre-



Figure 3.8: Example of vessel with chalk powder.

ated, the chalk flies off, making the crack detectable. During the testing it is possible to see from which areas of the vessel the chalk is detaching and whether it can be linked to certain acoustic emissions.

After the previously explained steps are done, the vessel can be clamped inside the chamber, attached to the hydraulic joint and the test can start.

3.3.2. Optical System Preparation

Before the test, the optical system itself must be prepared. The process consists in five operations, shown in Figure 3.9. They are: calibration of the cameras and checking, acquisition of information regarding the positioning of each sensor, preparation of the data acquisition software and setting of the correct lighting.

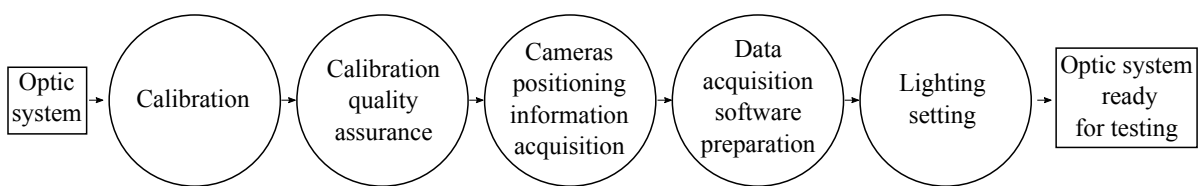


Figure 3.9: Steps for the preparation of the optic system.

The calibration is needed to determine geometrical parameters such as position and orientation of each camera of the stereo system and to define the intrinsic and extrinsic camera parameters [51]. This must be done for each couple of cameras used during the test and it is necessary for the post-processing of the data. For the current case, the calibration is performed using a calibration panel and the software ARAMIS, both provided by GOM. The calibration plate has many white dots on black background and 17 special symbols positioned with a certain layout in the panel. The panel used can be seen in Figure 3.10. To perform the calibration, it must be positioned in front of the cameras and rotated following 13 steps provided by GOM. For each step, a picture must be taken from both cameras. When the acquisition phase is finished, the pictures are loaded in the ARAMIS software, together with the panel code. The software will localize in each picture where the special symbols are positioned and will provide a calibration file. The quality of the calibration file is given checking the parameter “Intersection Deviation”. This parameter expresses the difference between where

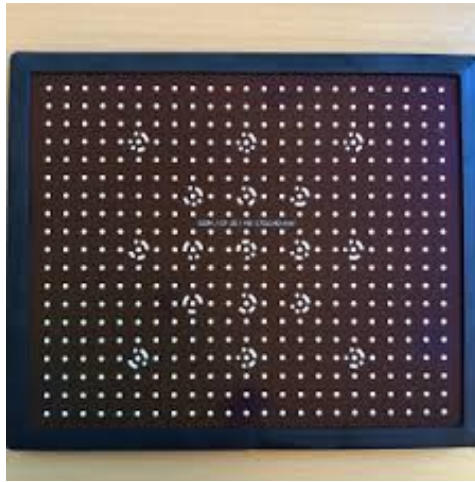


Figure 3.10: Calibration panel.

one camera expects a certain point with respect to where it really is. It is a pure number that multiplied by the pixel size, indicates how much of a pixel size the deviation is. The ARAMIS software considers a system not calibrated when the intersection deviation is higher than 0.3, thus when it is slightly less than a third of a pixel. With the current cameras and settings the pixel size is $4\ \mu\text{m}$. Figure 3.11 shows an example of a calibrated (3.11a) and a not calibrated optical system (3.11b).

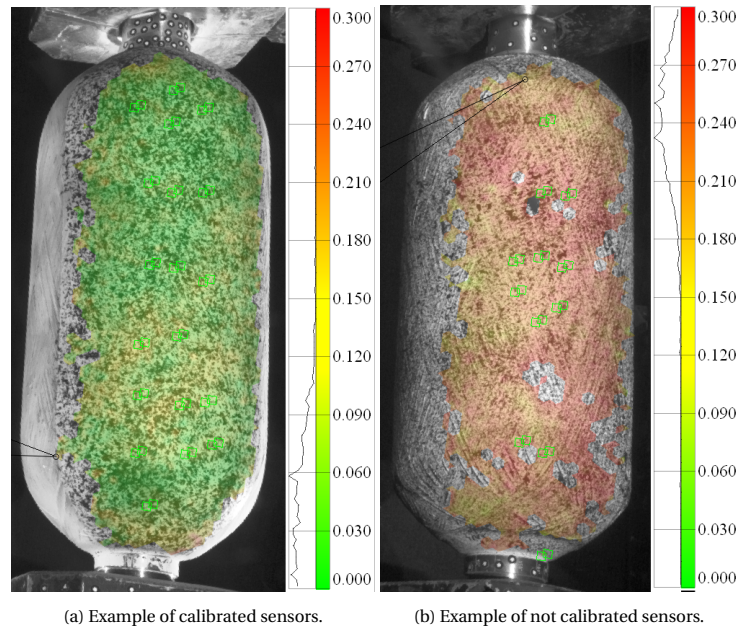


Figure 3.11: Calibrated and not calibrated sensors.

Since multiple stereo-cameras are used simultaneously, to get global knowledge on the pressure vessel it is necessary to merge the information of all the systems. In particular, it is needed to correctly position the deformation data calculated by each stereo system in the 3D space and with respect to each other. This is done using a calibration body provided by the company GOM. The calibration body has a shape of a cuboid, with a known distribution of reference points and identification markers. The calibration body used for the case is shown in Figure 3.12. The position of each of the reference points is recorded in a digital file. To perform the multi-sensor positioning, it is necessary to place the calibration body where the specimen will be tested. Then a picture must be taken from each stereo camera system. The pictures must be loaded in the software ARAMIS, together with the digital file with the reference points position. The software will recognize

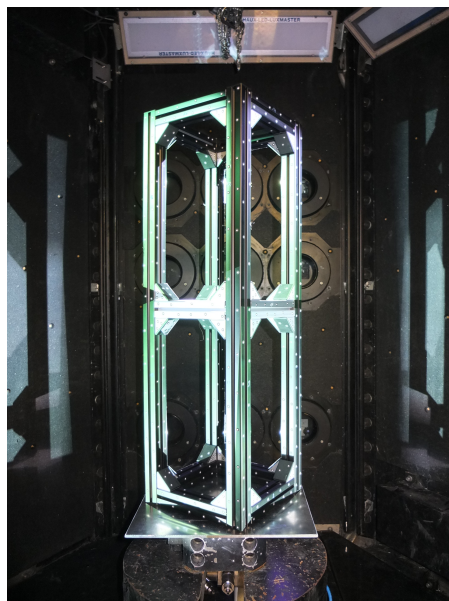


Figure 3.12: Calibration body.

the reference points on the pictures and correlate them with the ones in the digital files. It will then move the pictures in the 3D space to their real position.

It is also necessary to define the settings of the data acquisition software. It is possible to decide which systems to use, the images format, the frame rate and the total amount of pictures. For the current investigation, the frame rate was set to 1 fps and the frames quantity to 300. The images format chosen is .bmp.

Regarding the lighting, it is set up in a way to have a good contrast between the black and white paint in the speckled pattern. The light is produced by the projectors. After experiments it has been found that the best option is the projection of gray light.

3.3.3. Acoustic System Preparation

The acoustic system must also be prepared before starting the acquisition of data. The needed steps can be seen in Figure 3.13.

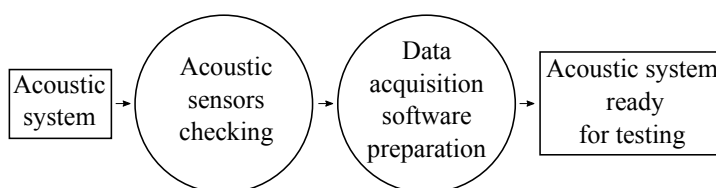


Figure 3.13: Steps for the preparation of the acoustic system.

The first action needed is the checking of the acoustic sensors. The testing chamber must be closed and kept in silence. In the software NoiseImage (the one used for the recording), all the active microphones are visible in a live view and their sound pressure level is shown. If one or multiple sensors show a substantially higher or lower sound pressure, they must be cleaned and if necessary replaced. The goal is to have all the sensors showing a similar pressure level. When this is reached, the sampling frequency and type of trigger must be set. The first is chosen as a consequence of the length of the recording. The trigger is set deciding if the software must store data acquired before or after pressing the trigger button. For the current investigation, the trigger is set at the end, which means that all the data before the pressing of the trigger must be stored.

3.3.4. Hydraulic System Preparation

When the vessel, the optic and acoustic system have been prepared, it is necessary to set the hydraulic. This consists in the creation of the pressurization cycle. It must be first decided whether a single pressurization or a cyclic one will be performed. Then the ending pressure level and the pressure rate must be set. In case of a burst test, the first is set high enough to a pressure stage that the vessel will not be able to withstand. In case of a cyclic test, also the minimum pressure levels must be selected, as well as the amount of cycles, the pressure rate or the pressurization and depressurization time and the pressure hold time. When everything is inserted, the test can start.

3.4. Data Acquisition and Post-Processing

In this paragraph it will be first described how the data is acquired during testing and which steps are performed in this phase (Paragraph 3.4.1). Afterwards, the post-processing of each system is described in detail. It will be explained which steps are performed to obtain the needed information from the DIC (Paragraph 3.4.2) and from the acoustic system (3.4.3).

3.4.1. Data Acquisition Process

When the vessel and the systems are ready, the test can start and the data acquisition with it. The steps to be done are shown, in order, in Figure 3.14.

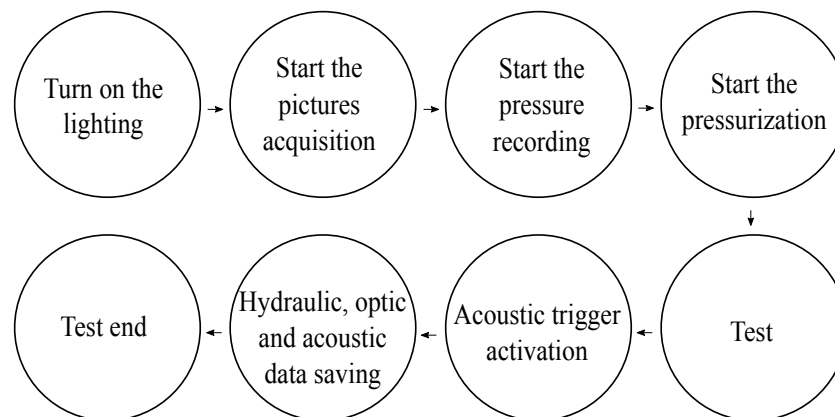


Figure 3.14: Data acquisition process.

First, the projectors must be turned on and few minutes are needed in order to project the predefined light. Then the GoPro recording can be activated, as well as the pictures and the pressure recording. Afterwards, the pressurization can begin, thus the test is performed. Finally, the acoustic trigger is activated. Before the ending of the test, the data coming from all the systems (hydraulic, optic and acoustic) must be saved.

Once the test is terminated, the post-processing of the data can be performed. The videos obtained with the GoPro and the data of the internal pressure of the vessel do not need any specific action. However, to obtain information from the optic and the acoustic systems it is necessary to perform some steps, which will be explained in detail in Paragraphs 3.4.2 and 3.4.3.

3.4.2. Optical Data Post-Processing

For the post-processing of the optical data the software GOM Correlate Professional is used. The main steps needed to carry on the analysis are shown in Figure 3.15. Each of them is described in detail.

Single Project Creation

This step consists in the creation of a project for each stereo system used during the testing. A single project is the set of all the pictures taken from the two cameras of a stereo system, chronologically ordered, which will be used to obtain strain and deformation data. To be able to post-process them, the pictures are loaded

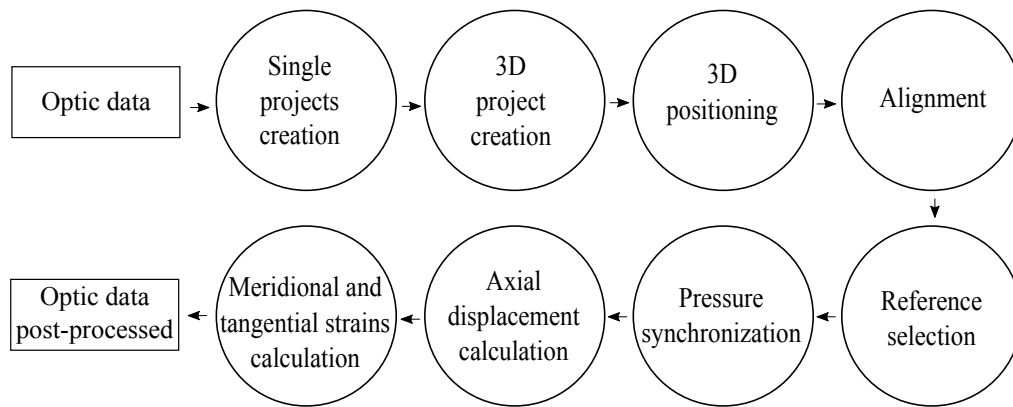


Figure 3.15: Steps for the processing of the optic data.

together with their calibration file. For the current case, a total of six single projects for each test have been created. A picture of the calibration body for each stereo system must also be imported in order to correctly position the pictures in space.

3D Project Creation

This consists in the merging of the single projects in a unique file. This allows to have the data of all the stereo cameras together and be able to study all the sides of the vessel.

3D Positioning

When creating the 3D project, the pictures of the different stereo systems are randomly positioned in the 3D space. To move them to the exact location, the imported pictures of the calibration body are used. The file containing the position of each of the reference points is also needed for the process. The software will recognize the reference points on the pictures and correlate them with the ones in the file. Then, it will move the pictures in the 3D space in their correct position, as it can be seen in Figure 3.16.



Figure 3.16: Pictures of six stereo-systems positioned.

Alignment

The next step corresponds to the alignment. It consists in the positioning and rotation of the global coordinate system in order to place it in the correct location. For this case, the chosen coordinate system is shown in Figure 3.17: the origin is located at the end of the bottom boss, in its center. The z coordinate corresponds with the vessel longitudinal axis of symmetry. The x and y axes are both in the radial direction with respect to the vessel.

Reference Selection

This step consists in the selection of the pictures which are set as reference. In the current case, the first picture of each system is chosen, because it corresponds to the unpressurized vessel. All the pictures taken dur-

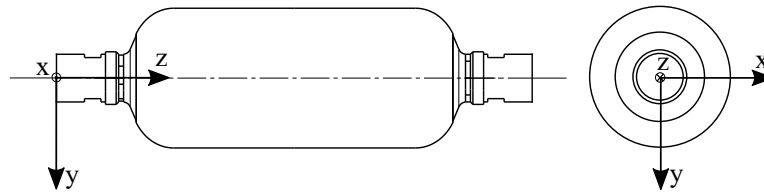


Figure 3.17: Global coordinate system.

ing the pressurization will be compared to the reference stage in order to calculate strains and displacements.

Tracking of Reference Points

The reference points attached at the top boss are needed to track the axial displacement of the vessel. Point components must be created in the software selecting the stickers attached on the surface. Afterwards, the position of the point components at each recorded stage is calculated and the displacement from the reference stage is obtained. The displacements are calculated in the 3 directions decided with the alignment, thus in the global coordinate system. An example of a point component can be seen in Figure 3.18.

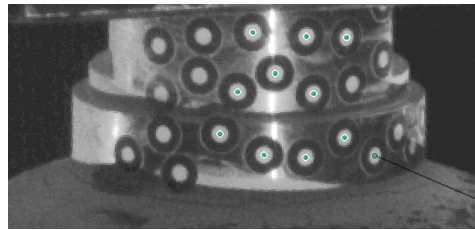


Figure 3.18: Example of a point component taken from the boss of a CPV.

Surface Components and Strains Measurement

Surface components are the tools responsible of evaluating the strains. The components are created on a speckled surface. Each of them is formed by facets, which are groups of pixels. For this case, a facet is a square with 19 pixels in each side. Depending on how these facets displace and rotate, strains can be calculated with respect to the unpressurized state, taken as reference. Contrarily to the displacements obtained from the point components, the strains are calculated in local coordinate systems. Each point of the surface component is the origin of its own local reference system. The three directions are tangential, meridional and through the thickness and can be seen in Figure 3.19. The 'z' local axis is oriented in the meridional direction of the vessel, tangent to its surface; ' θ ' is perpendicular to 'z' and it is also tangential to the vessel surface; the through the thickness axis 'r' is perpendicular to the other two axis, thus perpendicular to the vessel surface, pointing outwards.

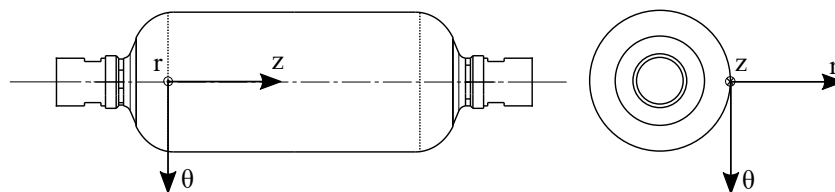


Figure 3.19: Local coordinate system.

The surface strains can be easily visualized in the software using a color map, as shown in Figure 3.20.

Pressure Synchronization

In order to link the displacement and strain data with the corresponding internal pressure stage, it is necessary to import the hydraulic data and synchronize it with the project. The synchronization is performed differently according to which kind of test is carried out: burst or pressurization. In case of burst test, the

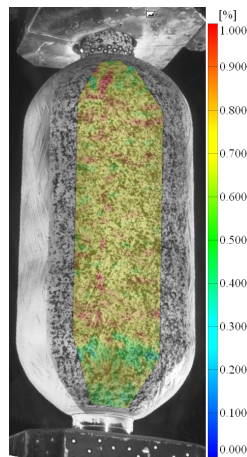


Figure 3.20: Full-field strain measurement of outer meridional strain.

maximum recorded hydraulic pressure is associated with the last picture in the project before the burst event. In case of pressurization test, the last picture before the depressurization is associated with the last sample of the hydraulic file which is recording the highest pressure before depressurization. It is then necessary to provide the pictures frame rate, indicating the time step between the photos. The software will then automatically take the corresponding pressure value, disregarding those in between. In the end, each photo is synchronized with its corresponding pressure stage.

Glasses Distortion Evaluation

As already explained, protection glasses are installed in the portholes between the cameras and the vessel during the testing. Due to their thickness (82.5 mm) it is necessary to evaluate the distortion and the error that it is introduced during the measurement. Measurements of the metal boss obtained with the software GOM Correlate Professional are compared to the nominal ones, taken from the CAD file. In particular it has been chosen to measure the lower diameter of the metal boss, as depicted in blue in Figure 3.21. The nominal

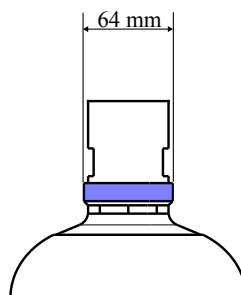


Figure 3.21: Part of the boss used for the comparison.

measurement is 64 mm. To obtain the diameter with the software, it was necessary to apply reference points on the part to measure and take pictures with the cameras from the three sides. Then point components are created and merged with the “fitting cylinder” function. This operation creates a cylinder that fits in the three point components given. The diameter has been measured on multiple vessels and the average calculated diameter is 64.17 mm with a standard deviation of 0.12 mm.

3.4.3. Acoustic Data Post-Processing

For the post-processing of the acoustic data, the software NoiseImage and MATLAB have been used. The main steps needed for the post-processing of the acoustic data are shown in Figure 3.22.

Pressures Synchronization

The synchronization between the sound pressure and the hydraulic pressure is the first action to perform.

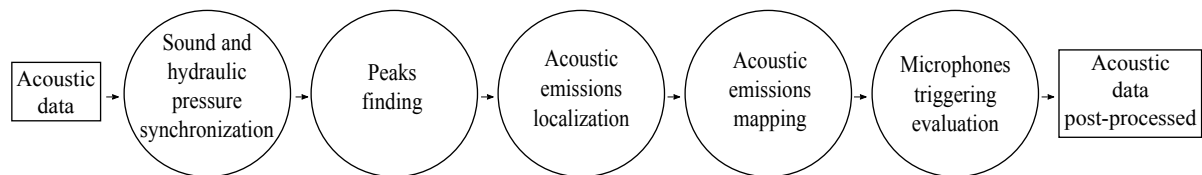


Figure 3.22: Steps for the processing of the acoustic data.

This is done differently according to the type of test. In case of pressurization test, the last sample recorded for both the acoustic file and the hydraulic pressure file is taken as matching point. In case of burst test, the maximum recorded internal pressure is synchronized with the sample corresponding to the maximum sound pressure amplitude. The latter is associated to the burst event. After the matching points are defined, the values of the hydraulic pressure file are interpolated. This is necessary due to the difference in recording sampling frequency (96 kHz for the acoustic data and 1 kHz for the hydraulic pressure). Linear interpolation is used for the purpose.

Finding Peaks

After the synchronization, the acoustic emissions must be detected. The `PeakFinder` algorithm implemented in MATLAB is used for the purpose. The algorithm is able to identify signal peaks which have specific characteristics predefined by the user. This process will give as output the amplitude of the acoustic emission and the time in which the event occurred. Since the acoustic file is synchronized with hydraulic pressure, the latter is also known.

The acoustic signal is first smoothed with the MATLAB filter `medfilt`. Appropriate parameters are then determined and the MATLAB `findpeaks` function is used to correctly identify the peaks. For the current case, three user defined variables are used: minimum amplitude, minimum peak prominence (`MinPeakProminence` in MATLAB) and minimum peak distance (`MinPeakDistance` in MATLAB). Previous studies in the department have identified a set of parameters that has been used for previous investigations. The minimum sound pressure amplitude was set to 2 Pa, the minimum peak prominence to 0.2 Pa and the minimum peak distance to 0.009 s as shown in the first column of Table 3.3. This set of parameters will be denoted as “Threshold I”. After further research it was understood that the previously mentioned parameters were not accurate enough for the goal of the current research. All the emissions with sound pressure amplitude below 2 Pa were in this case disregarded. For continuity reasons it has been decided to still use the parameters of “Threshold I”, but only to compare already defined acoustic variables. For all the other activities, such as emissions localization, it has been decided to define new thresholds which allow the detection of emissions with a sound pressure amplitude below 2 Pa. To gather the largest possible amount of peaks, the minimum amplitude threshold must be set as low as possible, paying attention not to detect the background noise. To define this threshold, it was necessary to investigate the maximum amplitude of the background noise during a pressurization test. From previous studies made in the department, it is known that during pressurizations subsequent to the first one, a vessel does not produce acoustic emissions detectable by the system [42]. Thus, testing an already pressurized vessel it was possible to determine the maximum amplitude of the background noise, which was found to be 0.05 Pa. A safety factor of two has been applied and the minimum amplitude threshold has been set to 0.1 Pa. This was raised to 0.3 Pa later in the research, because with 0.1 Pa an important amount of continuous emissions was detected, while the research is focused on burst type emissions. The thresholds on the minimum peak prominence and distance were decreased iteratively until the `findpeaks` function was detecting multiple peaks from the same emission. This effect is shown in Figure 3.23. Figure 3.23b is a zoom of Figure 3.23a. The blue marks correspond to detected emissions. It can be noticed that in Figure 3.23b two emissions are present, but a total of four peaks are detected by the `PeakFinder` algorithm. When a single emission was detected multiple times, the previously used parameter was set as low limit. The final parameters chosen for the investigation are summarized in Table 3.3 and are defined as parameters with “Threshold II”.

An example of output given from the `PeakFinder` tool is shown in Figure 3.24. Each detected peak is indicated with a blue marker.

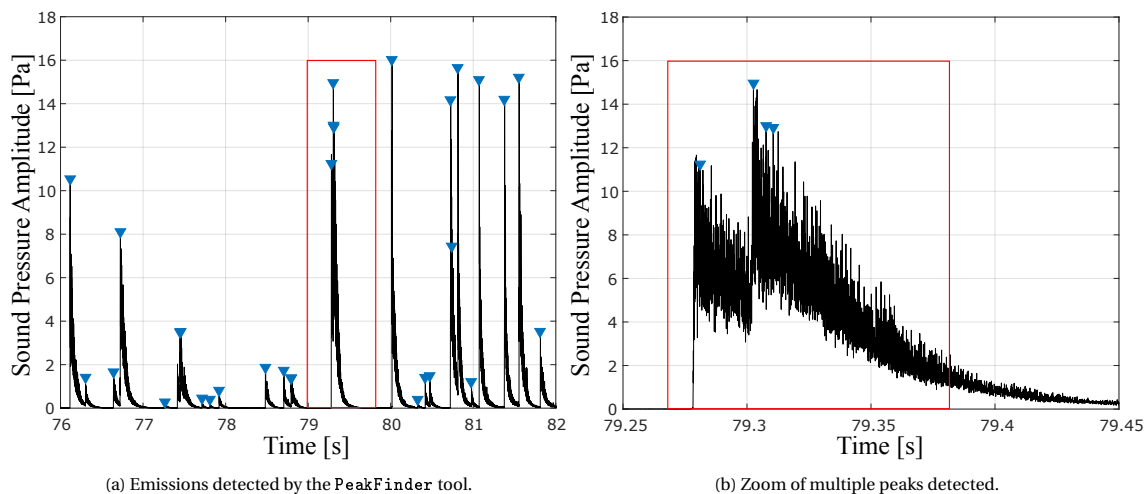


Figure 3.23: Multiple peaks detected on the same emission.

Table 3.3: Acoustic parameters used in the PeakFinder tool.

	Threshold I	Threshold II
Amplitude Threshold [Pa]	2	0.3
MinPeakProminence [Pa]	0.2	0.05
MinPeakDistance [s]	0.009	0.009

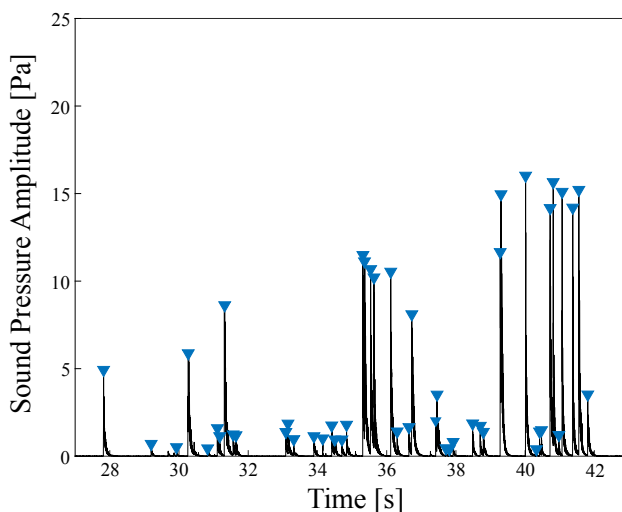


Figure 3.24: Example of peaks detected by the PeakFinder tool.

Emissions Localization in NoiseImage

After the emissions have been identified, it is necessary to localize them. This is performed using the software NoiseImage, which contains a delay-and-sum beamforming algorithm for the localization of acoustic emissions. In order to localize an emission, it is first necessary to import in the software the 3D-mesh of the vessel. This is produced scanning the vessel from all the stereo-cameras using the stripe light projection method. The scans are then merged to form the full 3D-mesh, as it can be seen in Figure 3.25a. Once the 3D-mesh is loaded in the software, the localization can start. Each acoustic emission detected with the PeakFinder tool is manually beamformed. Each peak is selected and the algorithm automatically provides the location of the acoustic source on the 3D-mesh, as it can be seen in Figure 3.25b.

After the emission is localized, a .wrl file of it is exported. It contains three types of data. A RGB color code

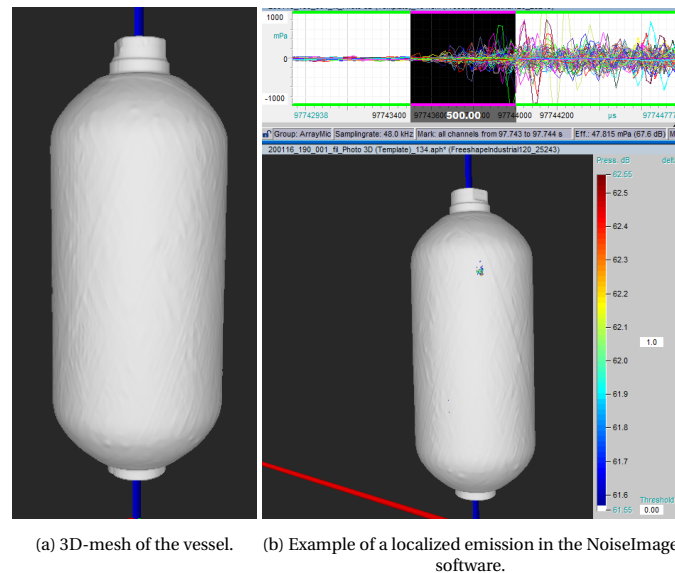


Figure 3.25: Vessel mesh and emission localization example.

contains the information regarding the minimum and maximum sound pressure amplitude of the emission. The number of the faces of the mesh associated with each color and the coordinates of the three vertices of each face are also exported.

The precision of the localization algorithm has been verified by Nebe et al. [8] positioning five acoustic signals generators on the surface of a vessel and recording the emissions. They concluded that the average localization error was 2.38 mm, with a maximum error of 5.83 mm.

Acoustic Emissions Mapping

The most damaged areas can be identified mapping all the localized emissions. This process cannot be done with the software NoiseImage, thus a MATLAB code has been written for the purpose. In order to easily visualize the entire vessel, a 2D map is created. The first step corresponds to the transformation of the cartesian coordinates (x , y and z) of each emission in polar coordinates (r , z and θ). Secondly, the radial coordinate is neglected and the 3D map is transformed in 2D, as shown in Figure 3.26. Due to this process the domes areas get distorted. To further simplify the visualization, bosses, domes and cylindrical sections are marked with different lines. The bosses are marked with solid lines and the cylindrical section with dotted lines, as shown in Figure 3.26. The domes are the areas in between a solid and a dotted line.

After the creation of the 2D map, the emissions are plotted. Each emission is represented with a circular marker. The color of the marker is correlated to the maximum sound pressure amplitude of the emission. An example of a 2D map representation with acoustic emissions can be seen in Figure 3.27. This visualization is useful to understand which are the most damaged areas of the vessel. However, it does not provide knowledge regarding the damage progression during the pressurization. Since the acoustic and hydraulic files have already been synchronized, the previous plot can be easily modified. The tangential coordinate (θ) of the acoustic emission is neglected, while its axial coordinate is kept and plot with respect to the internal hydraulic pressure. Also for this case the emissions have been represented with circular markers and their color depends on their maximum sound pressure amplitude. An example of this representation can be seen in Figure 3.28.

Microphones Emission Detection

For the current research it has also been studied how different emissions trigger the sound pressure sensors present in the testing chamber. The location of the first microphones triggered is studied. Also the microphones recording the maximum amplitude of the AE are investigated. The delay of the peak with respect to the first microphone triggered are calculated. This process was automatized within MATLAB. For each localized emission, the four microphones recording the maximum sound pressure are detected. Informa-

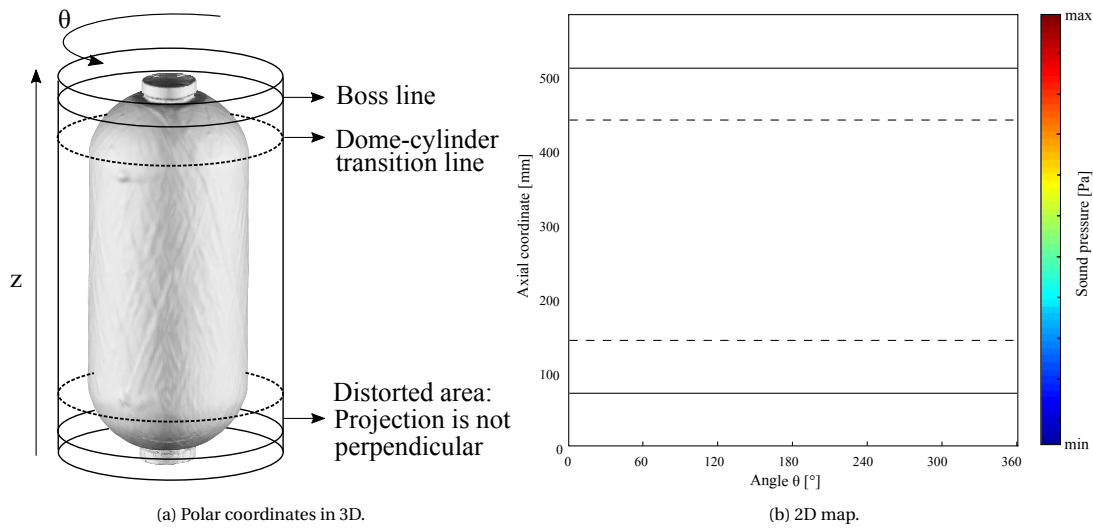


Figure 3.26: Transformation of 3D map into 2D.

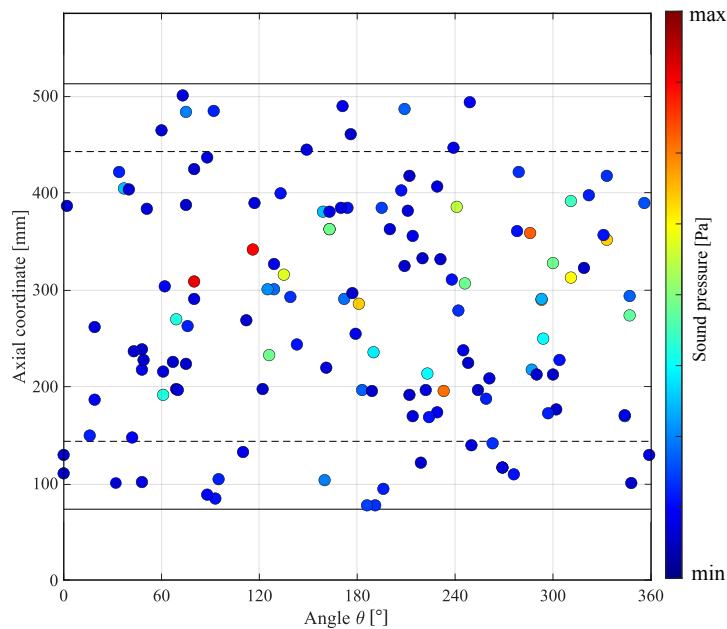


Figure 3.27: Example of representation of the acoustic emissions in a 2D map.

tion regarding the time, the amplitude of each peak and the microphones identification numbers are stored. Then, the first four microphones triggered are detected and their identification number is noted. The first microphones triggered are defined as the first four microphones which record a sound pressure amplitude higher than 0.3 Pa. The time interval between the start of the emission and the four maximum peaks is calculated. The identification number of these sensors is also stored. For a better understanding, an example is provided. Figure 3.29a shows the acoustic file of a certain emission: each line corresponds to one sensor. The microphones which record the maximum sound pressure amplitude are indicated with a red arrow, while the first triggered microphones with a black one. The delay of the maximum peak with respect to the emission start is indicated with a dotted arrow. When all the information is gathered, the results are plotted. An example can be seen in Figure 3.29b. The hexagonal shape is a representation of the testing chamber, being each side one of the lateral walls. The circle at the center represents the CPV. The black cross markers represent the first triggered microphones and the red circles the ones recording the maximum sound pressure amplitude. Each marker is positioned on the wall where the corresponding microphone belongs to and it is labeled with the acoustic sensor identification code and the delay with respect to the first microphone triggered. For the red markers it is also shown the maximum sound pressure amplitude recorded by that sensor.

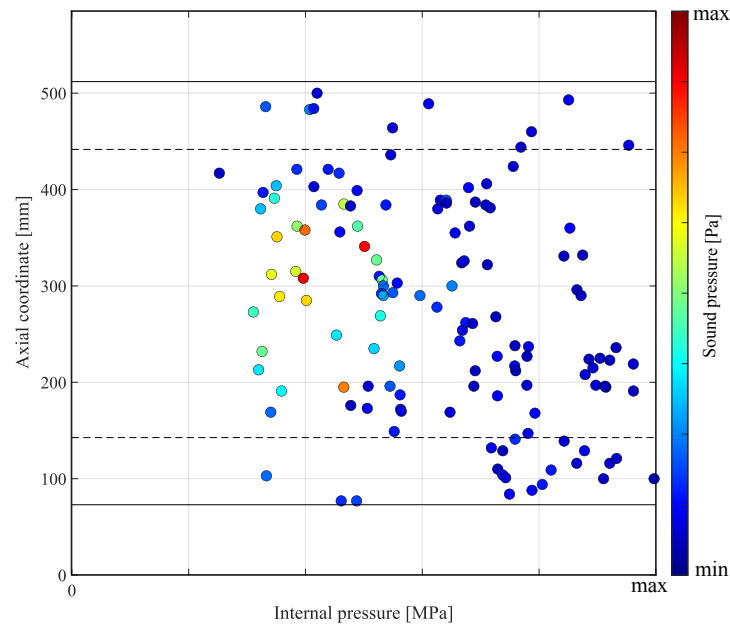
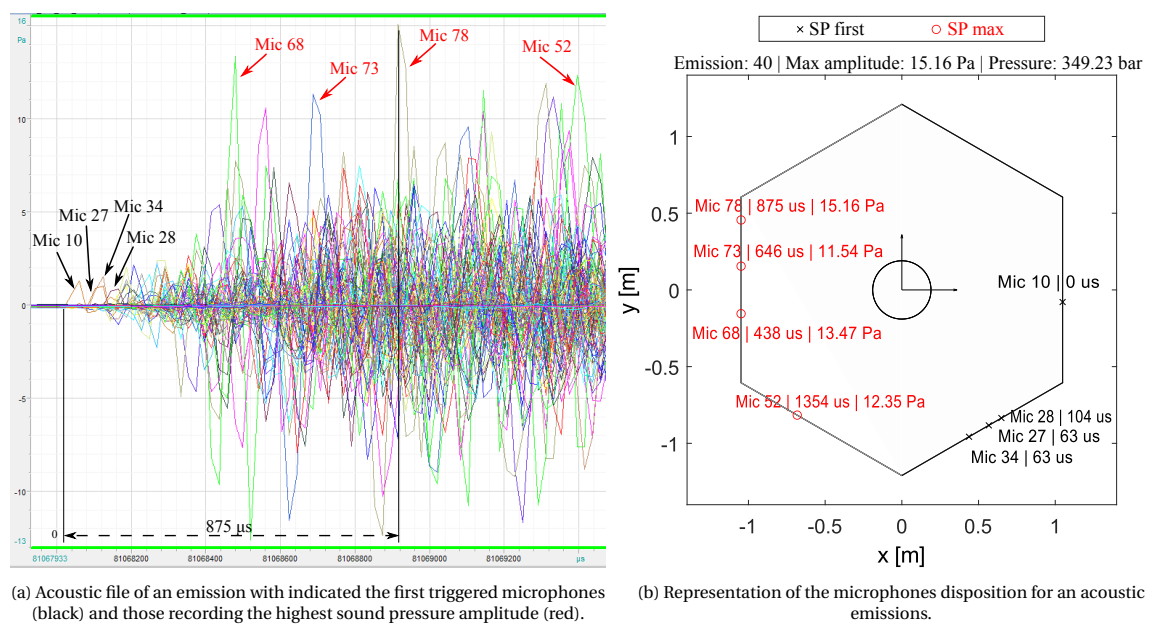


Figure 3.28: Example of representation of the acoustic emissions with respect to its axial position and the internal hydraulic pressure of the CPV.



(a) Acoustic file of an emission with indicated the first triggered microphones (black) and those recording the highest sound pressure amplitude (red).

(b) Representation of the microphones disposition for an acoustic emissions.

Figure 3.29: From the acoustic file to the MATLAB output.

3.5. Damage Inspection

The goal of the observations is to identify the type of damage and the localization through the thickness of the laminate. This has been done using CT scans. This paragraph will explain the specimen preparation and the equipment used.

As already explained in Paragraph 2.2.3, the resolution of the CT results depends on the specimen size. The scan of a full vessel does not provide the needed resolution for the goal. The areas of interest must be se-

lected and cut from the vessel. This is possible only on vessels subjected to a pressurization test and not burst. For cost reasons, three layups have been selected for the purpose: A, B and F. The characteristics of the pressurization test are summarized in Table 3.4. The maximum pressure has been set to 105.0 MPa because it corresponds to the pressure of the EOL test. For layup A, the pressurization was stopped at 75 MPa. This because the average burst pressure of this stacking sequence is 103.8 MPa with a minimum of 91.4 MPa. After the pressurization, the emissions are localized and the 2D-map is created. As already explained in paragraph 3.4.3, this visualization provides the polar coordinates of the emissions (Figure 3.27). For each of the pressurized layup, some of these emissions have been selected for the CT scanning. Table 3.4 shows the data of the specimens that have been scanned for the current project. The pressure rate during the pressurization

Table 3.4: Data of the specimen scanned with the CT method.

	Max pressure [MPa]	Pressure rate [MPa/s]	Specimens scanned	Location of specimen
Layup A	75.0	1.0	2	Cylinder
Layup B	105.0	3.0	4	Cylinder
Layup F	105.0	1.0	2	Cylinder

of the vessel with layup B is different because the specimen has been taken from a vessel used for previous investigations. The influence of the pressure rate on the obtained data will be explained in Paragraph 4.1.5.

Known the coordinates of the emissions, they need to be localized on the vessel. This is possible because in the lower boss of each vessel it is present a scale with angles from 0° to 360°, as shown in Figure 3.30. The angles of the 2D-map are synchronized with those present on the boss. The axial coordinate is measured using a measuring tape. After the chosen emissions are marked on the CPV, specimens must be cut. The vessel is

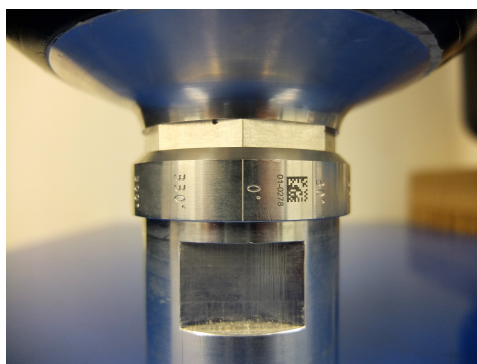


Figure 3.30: Angle scale in the boss of the CPV.

first cut in rings with a Mössner Rekord SSF 520 sax (Mössner GmbH, Pforheim, Germany). This is done by the qualified staff of Daimler AG. To get specimen of the required dimensions, the rings needed to be further cut. This is performed by the student using a Struers Discotom 6 saw with a Struers 56A25 blade (Struers, Ballerup, Copenhagen). The final size of the specimen is 10 mm by 10 mm. The specimen is then glued to a glass rod in order to keep it in place during the scanning process. The CT scans are performed in the Daimler AG laboratories by the qualified staff. The equipment used is a Nanotom M (General Electric, Schenectady, New York) scanner and the results are processed and visualized with the software VG-Studio MAX (Volume Graphics GmbH, Heidelberg, Germany).

4

Results and Discussion

4.1. Acoustic Behavior

In this paragraph, the acoustics behavior of the selected layups is analyzed by means of a single specimen. Due to time constraints, only five of the seven predefined stacking sequences have been analyzed in detail. The results of the other two layups, which are used for other investigations and projects in the department, will be briefly introduced in Paragraph 4.5. For the representation of the stacking sequences, the reader is referred to Figure 3.4, in which the dark gray represents the helical layers, while the light one the hoops. These representations are used in the present chapter as legends for an easier identification of the stacking sequences.

In order to study the different layups, it is necessary to define variables that will be used for the comparison of the data. For continuity reasons, it has been decided to use some that have been already identified during previous investigations in the department [42]. As already explained in paragraph 3.4.3, the parameters chosen to detect the acoustic emissions (defined as threshold I) do not take into account a significant amount of peaks of low amplitude. When localizing the acoustic emissions of a vessel, the parameters in the PeakFinder tool are lowered and threshold II is used. The parameters have already been explained in the previous chapter in Table 3.3.

The first variable chosen for the comparison is the maximum sound pressure amplitude (A_{max}). This is defined as the maximum amplitude of the sound pressure recorded during the EOL test. The second parameter considered is the hydraulic pressure at which the first emission is detected, labeled with the symbol $P_{AE,start}$. N_{hits} denotes the number of detected emissions. All the previously explained variables are evaluated in the hydraulic pressure range 5 - 105 MPa. It has been chosen 105 MPa because it corresponds to the maximum pressure during an EOL test. For layup A, due to the low burst pressure, this value has been reduced to 75 MPa.

4.1.1. Layup C

The stacking sequence of layup C is $[(\pm 19.9^\circ)_{10} / (+88.5^\circ, -88.5^\circ)_{15} / (\pm 19.9^\circ)]$, thus it is formed (from the inner to the outer ply) by 10 helicals, 30 circumferentials and another helical as outermost layer. A total of six vessels of this configuration have been tested, all of them subjected to burst.

Figure 4.1 shows the acoustic channel file of one vessel of this layup. In particular, the sound pressure amplitude is plotted with respect to time in the hydraulic pressure range 5-105 MPa. Figure 4.1b is a zoom of Figure 4.1a and gives more detailed information regarding the acoustic behavior of this layup. In the top part of the graphs it is displayed the internal hydraulic pressure. It is not possible to directly plot the acoustic with respect to the hydraulic pressure due to some small non-linearities in the latter one. As it can be seen from Figure 4.1, at the beginning of the pressurization the vessel does not produce any detectable emission. After about 15 seconds (corresponding to an internal pressure of about 20 MPa), few peaks below 5 Pa are recorded, followed for the next 20 seconds by emissions above 10 Pa, reaching a maximum sound pressure of 19.47 Pa. For the next 10 seconds, until 45 MPa, emissions up to 5 Pa are recorded, followed by an important amount

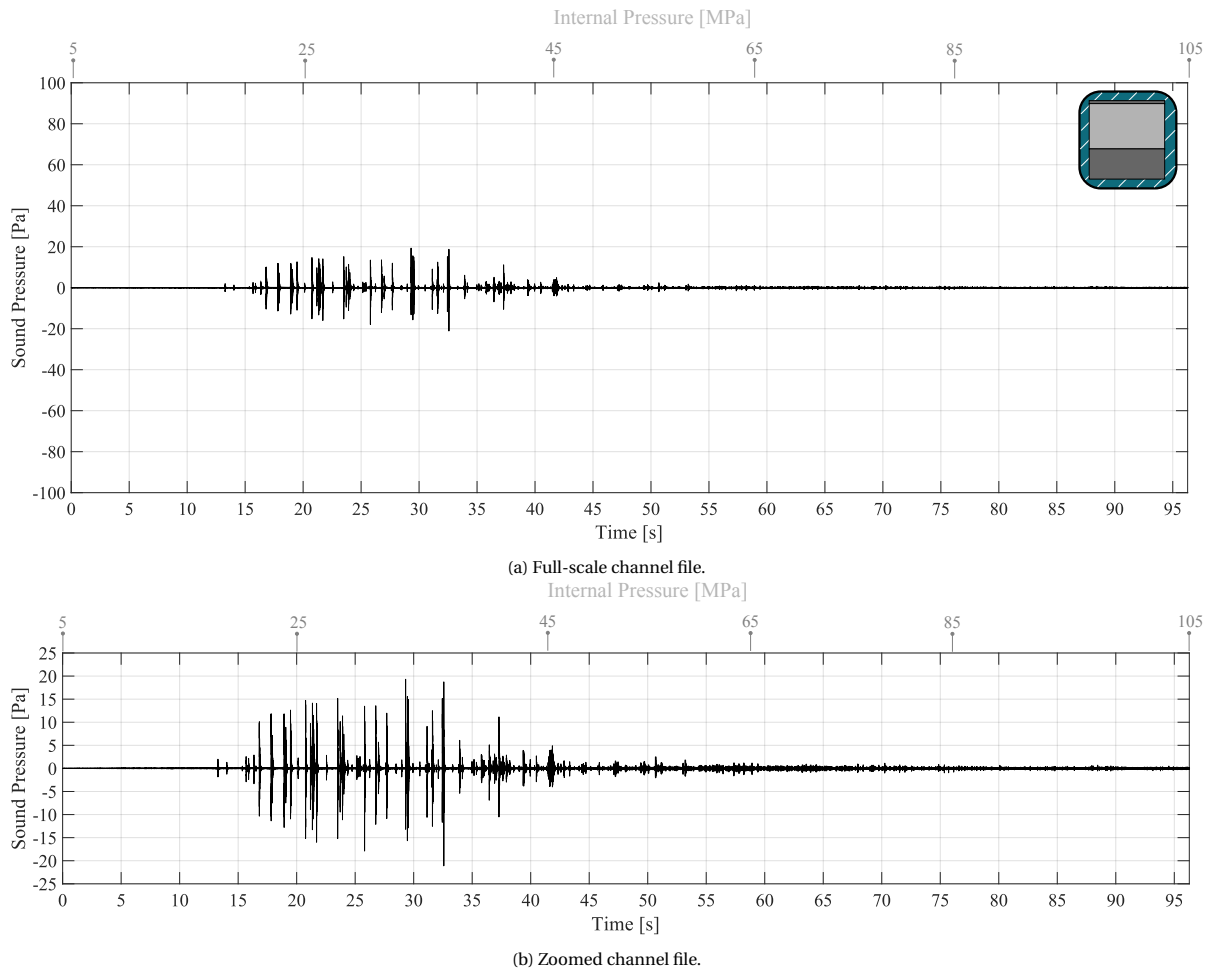


Figure 4.1: Acoustic file of vessel C in the hydraulic pressure range 5-105 MPa.

of small amplitude peaks, usually below 1 Pa, that are present until the end of the pressurization. The maximum sound pressure amplitude (A_{max}) recorded for the vessel is 19.47 Pa and the first emission detected corresponds to the hydraulic pressure of 18.1 MPa. In total, in the predefined pressure range, 51 peaks are detected. They are identified using threshold I. Due to the low pressure stages at which they take place, they could be caused by matrix cracking in the 90° plies [42, 79, 82], thus the hoops. The variables of all the tested vessels of the current layup are shown in Table 4.1, together with their averages and standard deviations. As

Table 4.1: Maximum sound pressure amplitude recorded in the pressure range [5 - 105] MPa, hydraulic pressure corresponding to the first detected emission and detected peaks for layup C.

Vessel	A_{max} [Pa]	$P_{AE,start}$ [MPa]	N_{hits} [-]
C - 01	19.47	18.1	51
C - 02	24.45	21.3	63
C - 03	22.56	19.3	61
C - 04	23.07	22.3	53
C - 05	29.94	17.1	62
C - 06	20.01	20.3	64
$\mu \pm s$	23.25 ± 3.45	19.7 ± 1.8	59 ± 5

concluded by Torres Guijarro [42], it can be noticed that the analyzed parameters are similar for all the vessels with the same layup, thus a clear pattern is present.

As already explained, for the emissions localization it was decided to set other parameters in the PeakFinder

tool, in order to detect also the peaks with amplitudes below 2 Pa. With threshold II, for the current vessel it was possible to detect 278 emissions of which 246 have been correctly localized. The missing 32 detected peaks did not correspond to a burst-type acoustic emission, but to a continuous-type. It is not possible to localize this kind because they are an overlapping of multiple emissions [30, 59, 61], coming from different areas of the vessel.

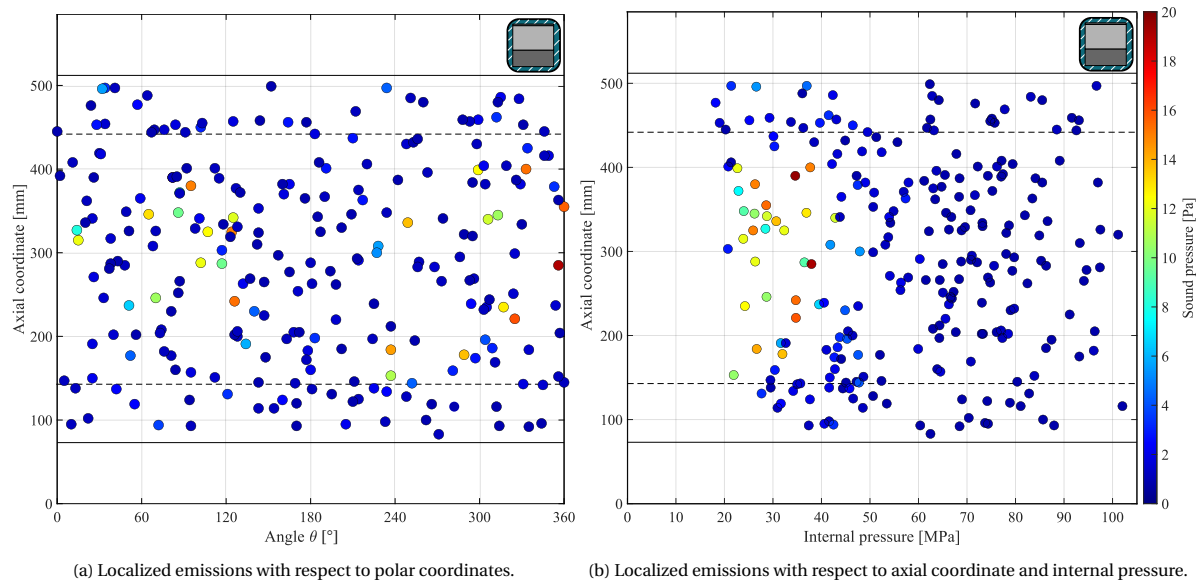


Figure 4.2: Localized emissions plots for layout C.

Figure 4.2 shows the localized emissions for this vessel. In particular Figure 4.2a displays the position of the emissions with respect to the axial and tangential coordinate. It can be noticed that all the peaks with higher amplitudes (above 8 Pa) are localized in the cylindrical section. This fact helps to reinforce the hypothesis that these emissions correspond to IFF in the hoop layers, since they are only wound in the cylindrical section and not in the domes. The fact that they have such a high amplitude could be related to the important size of the fracture surface [68]. In fact, once a crack is created, it progresses until it finds a crack stopper, such as a change in layer orientation [31]. In the current case, the cracks could easily develop through the 30 hoop layers and get stopped by the top and bottom blocks of helicals.

Figure 4.2b shows the axial position of the emissions with respect to the internal hydraulic pressure. It can be noticed that all the emissions with higher amplitude occur at low pressure stages, from 20 to 40 MPa. The rest of the pressurization is characterized by peaks of sound pressure amplitude below 6 Pa. As explained in Paragraph 2.4.2, when the amplitude is low it might be that either the fracture surface created is very small or that the damage takes place in depth in the laminate. With the current information it is not possible to define which case corresponds to the current situation. In the pressure range 20 - 40 MPa, some low amplitude emissions also occur, mainly localized in the transition zone. They could be caused by matrix cracking taking place in that area. In that zone, the hoops are tapered towards the dome. During the curing and the manufacturing process, the tows could laterally slide due to the tension applied. This could lead to the formation of small gaps that get filled with resin. These resin rich gaps could crack and cause AEs. The pressure range 40 to 50 MPa is characterized by low amplitude emissions localized through the entire height of the vessel. In the next 10 MPa only few emissions occur and they are mainly positioned in the cylindrical section. From the internal pressure of 60 MPa to the end of the test a significant amount of acoustic emissions has been localized, all characterized by a sound pressure amplitude below 2 Pa. The majority of the emissions are located in the cylindrical section and few in the domes. In the latter pressure range, nearly no emissions are localized in the transition zone. The presence or absence of these low amplitude emissions in some areas of the vessel cannot be explained with the few information provided. If those peaks are related to damage taking place on the surface, their occurrence might be related and explained with the superficial strain distributions, which are calculated with the DIC. This topic will be evaluated in detail in Paragraph 4.4.

4.1.2. Layup F

Layup F is characterized by five blocks of six circumferential layers each, separated by blocks of two helical plies, except the outermost which is formed by a single helical. The stacking sequence of this layup is: $[(\pm 19.9^\circ)_2 / (+88.5^\circ, -88.5^\circ)_3 / (\pm 19.9^\circ)]$. Eight vessels of this configuration have been manufactured, of which six were subjected to burst and two have been pressurized up to 105 MPa. During one of the pressurization tests, a problem was encountered with the hydraulic system data recorder, thus data of the internal pressure are missing.

Figure 4.3 shows the acoustic file of the other pressurized vessel, in the range 5-105 MPa. Comparing Figure

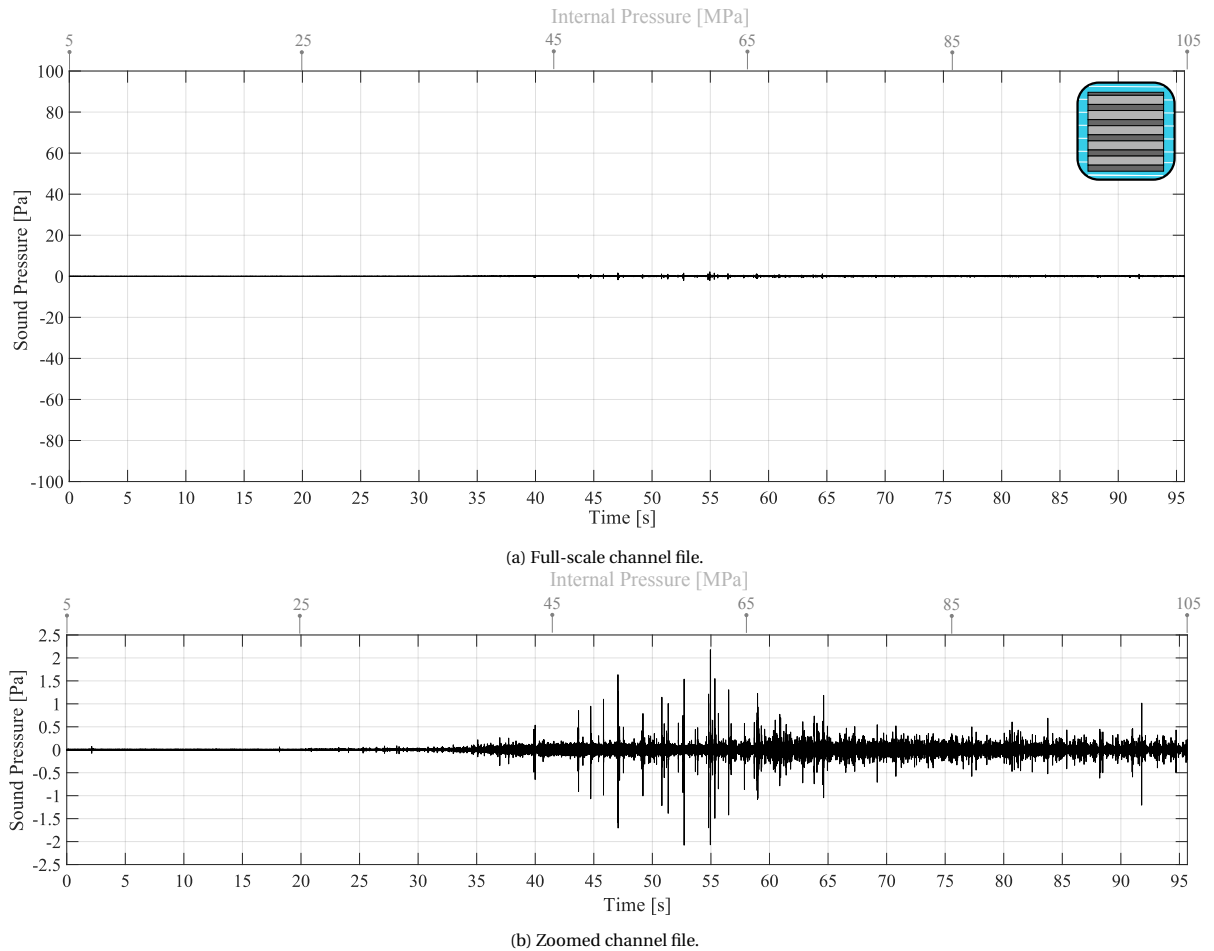


Figure 4.3: Acoustic file of vessel F in the hydraulic pressure range 5-105 MPa.

4.3a with Figure 4.1a it is possible to notice that layup F produces acoustic emissions of lower amplitude. Figure 4.3b is a zoom of Figure 4.3a. The first 20 seconds of the pressurization are characterized by the absence of significant acoustic emissions. They are followed by other 20 seconds (until just before 45 MPa) in which few peaks can be observed but none detectable by the PeakFinder tool because characterized by sound pressure amplitude below 0.3 Pa. From an internal pressure of about 43 MPa, emissions with amplitude above 0.5 Pa can be detected, until reaching a maximum of 2.18 Pa. After this maximum peak, some more peaks above 0.5 Pa can be seen until reaching second 65, at about 72 MPa. Afterwards, up to the end of the pressurization, a significant amount of low amplitude emissions (with sound pressure below 0.5 Pa) can be observed. The maximum sound pressure amplitude (A_{max}) recorded for this vessel is 2.18 Pa. If compared to the maximum of layup C (19.47 Pa), it can be noticed that it is consistently lower. If these peaks are caused by IFF in the hoops, the difference in sound pressure amplitude could be explained by the fracture surface size [42, 68]. In layup F, the crack size is one fifth with respect to C, due to the presence of helical layers every six hoops. The first emission detected corresponds to the hydraulic pressure of 43.0 MPa and it is the only detected peak in

the predefined pressure range, when using threshold I. The maximum sound pressure amplitudes (A_{max}), the hydraulic pressure of the first detected emission recorded in the pressure range 5 - 105 MPa and the peaks detected (N_{hits}) are shown in Table 4.2. The symbol * denotes the vessel that is missing the hydraulic pressure data. In Table 4.2 it can be noticed that for all the tested vessels except three, no emissions were detected in

Table 4.2: Maximum sound pressure amplitude recorded in the pressure range [5 - 105] MPa, hydraulic pressure corresponding to the first detected emission and detected peaks for layup F.

Vessel	A_{max} [Pa]	$P_{AE,start}$ [MPa]	N_{hits} [-]
F - 01	0.90	-	0
F - 02	2.46	21.0	1
F - 03	1.51	-	0
F - 04	1.62	-	0
F - 05	0.86	-	0
F - 06	0.71	-	0
F - 07	2.18	59.3	1
F - 08*	2.45	/	1
$\mu \pm s$	1.59 ± 0.67	40.2 ± 19.2	0.4 ± 0.5

the range 5-105 MPa. When lowering the three parameters of the PeakFinder (using threshold II), as shown in Table 3.3, 70 peaks were detected in this vessel, of which 64 have been localized.

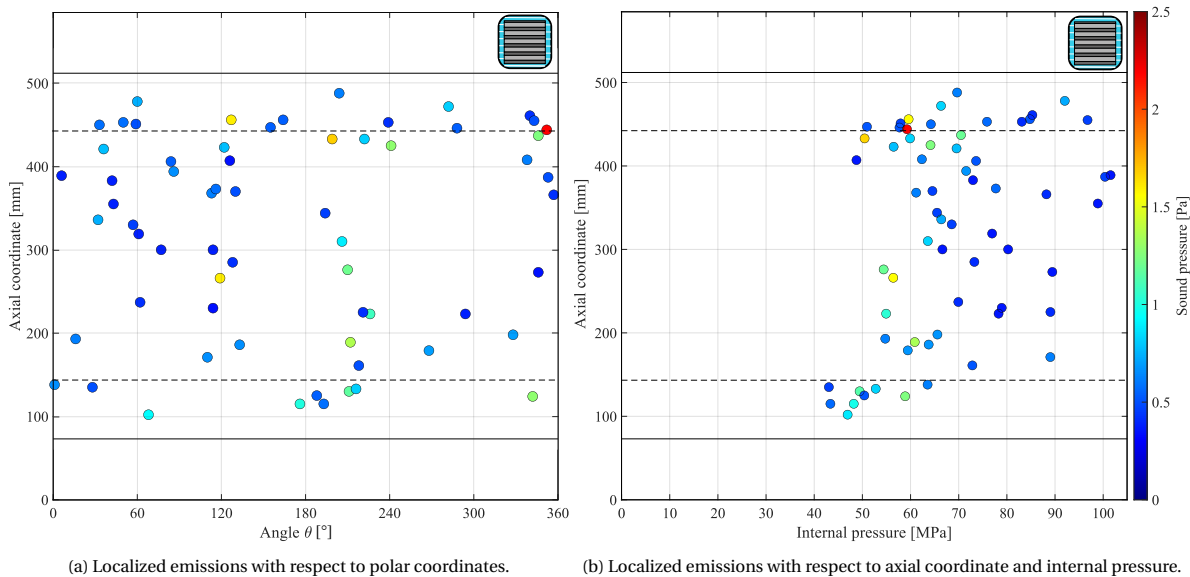


Figure 4.4: Localized emissions plots for layup F.

From Figure 4.4a it can be seen that emissions with sound pressure amplitude above 0.8 Pa are distributed in both the cylindrical section and transition zones. This means that these emissions cannot be uniquely associated with IFF in the hoop layers, since only few of them are wound in the transition zone due to tapering. Emissions with pressure amplitude below 0.8 Pa are mainly located in the cylindrical section. This follows the same trend observed in layup C.

Figure 4.4b shows the emissions with respect to the internal vessel pressure. It can be noticed that at pressure stages below 40 MPa, no emissions are present. The first localized are concentrated in the bottom dome-transition area. It was not clear why they were all concentrated in that area and no emissions could be found in the top transition. Due to vessel symmetry, it is expected that top and bottom transition zones and domes would behave similarly. The vessel has been visually analyzed and a ring with air bubbles (which can be associated to air inclusion) have been detected in the area, as shown in Figure 4.5. This increased superficial porosity could have been the cause of damage formation at low loads and as a consequence of presence of

AEs. This hypothesis has been proven comparing pictures taken at pressure stages 40 and 50 MPa and look-

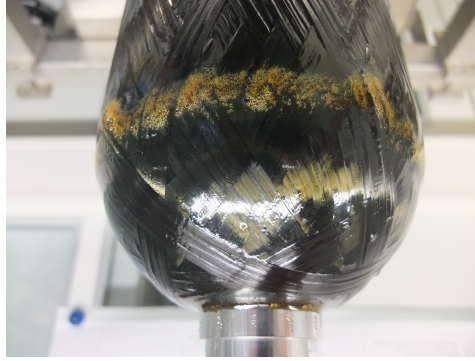
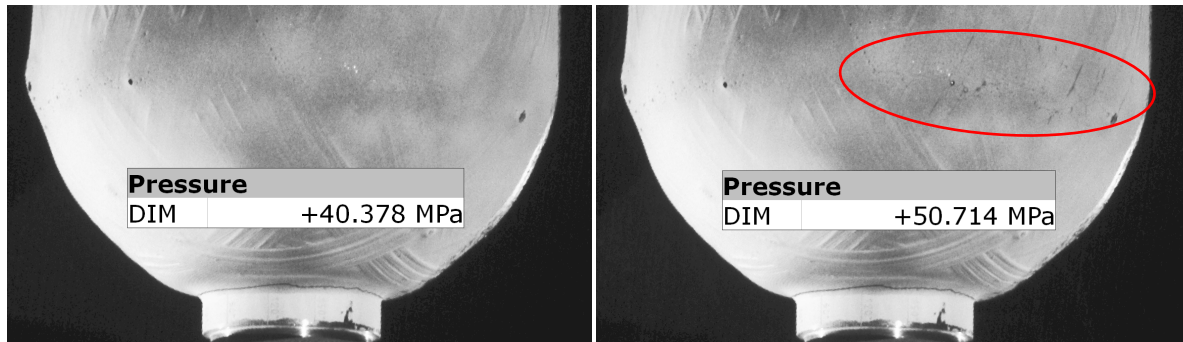


Figure 4.5: Presence of bubbles at the bottom transition zone of layup F

ing at the chalk distribution in the area. In Figure 4.6, the picture on the left shows the transition zone of the vessel before the detection of the emissions at a pressure of about 40 MPa. Figure 4.6b shows the same area at a pressure stage of about 50 MPa, thus after those first peaks have taken place. In the red circle, some dark lines have appeared caused by the falling of the chalk dust. These emissions can be associated to superficial cracking of the matrix in the area. It was not clear what caused this small defect, since no problems during manufacturing and curing have been highlighted. Air inclusion in the transition zone is not a peculiar characteristic of layup F, otherwise it should have been found also in the top part and in other vessels with the same stacking sequence. Since this was not the case, it can be concluded that it was a defect. After these first



(a) Bottom transition zone without superficial damage at pressure stage 40.378 MPa.

(b) Bottom transition zone with visible superficial damage at pressure stage 50.714 MPa.

Figure 4.6: Bottom transition zone of layup F before and after the occurrence of the initial acoustic emissions.

emissions, the next peaks are characterized by higher sound pressure amplitude and are distributed in the pressure range 50 - 70 MPa. They are mainly localized in the cylindrical section and the transition area. From the internal pressure 70 MPa to the end of the test, emissions with amplitude below 0.5 Pa are present and they are mainly localized in the cylinder, as was the case for layup C. The presence and the cause of these last emissions cannot be explained yet with the few data provided.

4.1.3. Layup A

The stacking sequence of layup A is the same of layup C, but reversed. One helical is the innermost layer and it is followed by 30 circumferentials and 10 more helicals on the outside. The stacking sequence is $[(\pm 19.9^\circ) / (+88.5^\circ, -88.5^\circ)_{15} / (\pm 19.9^\circ)_{10}]$. A total of seven vessels of this configuration have been tested of which five were subjected to burst and two to a pressurization test. Due to the low burst pressure of this layup, with an average of 103.8 MPa and a minimum of 91.4 MPa, the pressurization has been stopped at 75 MPa. A problem has been encountered in the acoustic system when testing one of the vessels subjected pressurization. The acoustics of this vessel is missing.

Figure 4.7 shows the acoustic channel file of layup A. The plot represents the sound pressure amplitude with respect to time in the hydraulic pressure interval between 5 to 75 MPa. The hydraulic pressure is present at the top of the graphs. Looking at Figure 4.7a it can be noticed that the acoustic behavior of this layup is in between

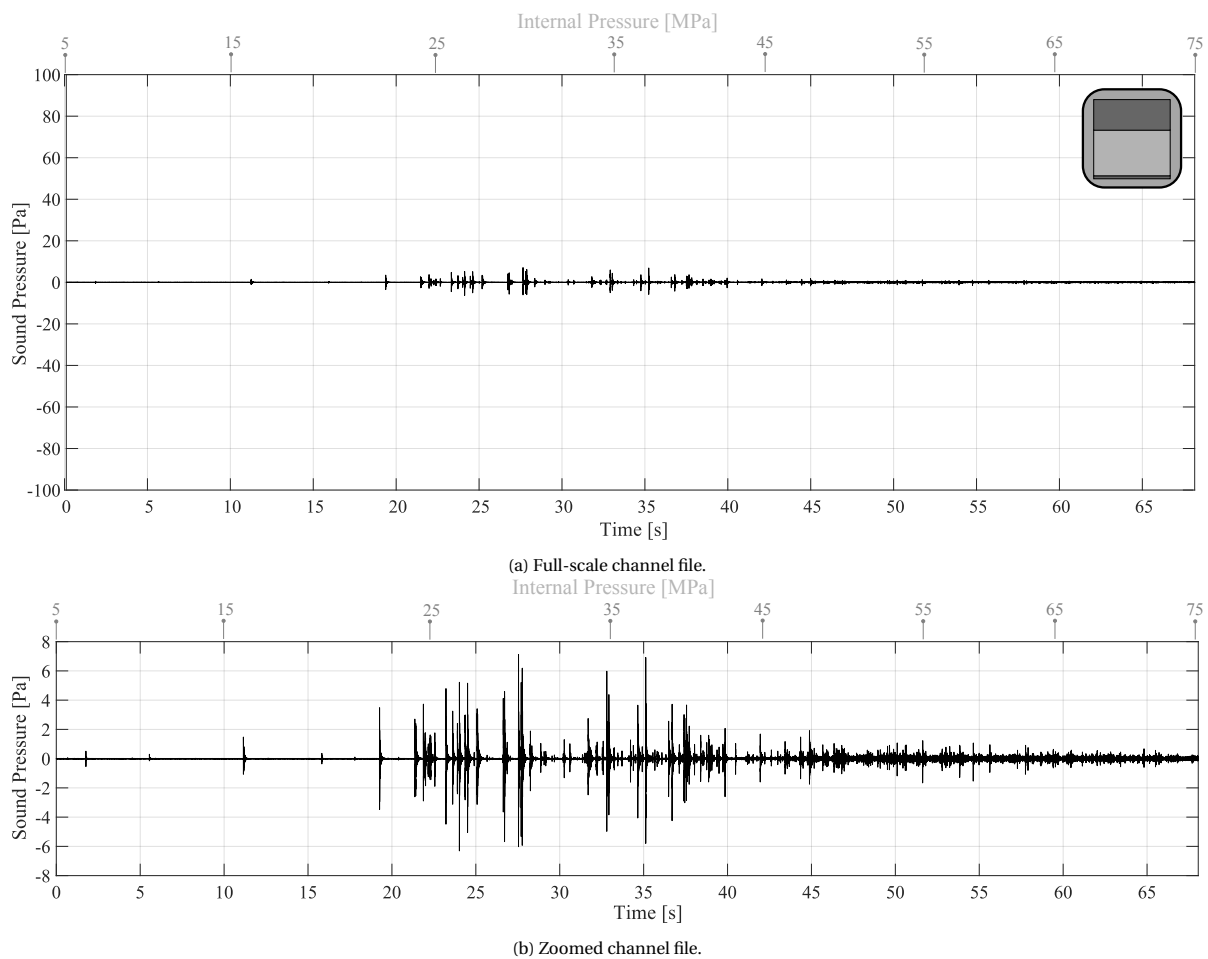


Figure 4.7: Acoustic file of vessel A in the hydraulic pressure range 5-75 MPa.

C and F in terms of sound pressure amplitudes. Figure 4.7b is a zoom of Figure 4.7a. At about second 11 (just above the hydraulic pressure of 15 MPa) a single emission is present. This has not been considered the first peak, because while performing the beamforming, it has been localized in the metal boss, as shown in Figure 4.8. This peak has been associated to an acoustic source caused by the hydraulic pump or any hydraulic valve. The first emission of the vessel is considered the one happening at second 19, which corresponds to the hydraulic pressure of 23.3 MPa. After second 20 it is possible to notice emissions with amplitudes above 3 Pa, with few peaks reaching 5 Pa. 7.05 Pa is the maximum amplitude recorded for the current vessel. In the range between second 35 and 40 (37 - 43 MPa) few more emission are present, but all with amplitudes below 5 Pa. Afterwards, the acoustic file is characterized by low amplitude acoustic emission, the high majority of them with a sound pressure below 1 Pa. The maximum sound pressure amplitude (A_{max}) recorded for this layup is 7.05 Pa. When comparing it to layup C, which has the same stacking sequence but in reverse order, it can be noticed that there is an important difference. For layup A it is 7.05 Pa and for C 19.47 Pa. If these emissions can be associated to IFF in the hoops, the difference can depend on the depth of the fracture in the laminate. Both stacking sequences have a single block with 30 hoops layers which are positioned at different heights in the laminate (deeper for A). The results obtained are in agreement with what found in literature [30, 82]. Drawing conclusions at this point is premature because only few data have been analyzed. The first detected emission for layup A takes place at a hydraulic pressure level of 23.3 MPa and the hits counted for the pressure range 5 - 75 MPa are 27. Table 4.3 shows the results of the other tested vessels of the current layup.

The emissions localization has been performed lowering the three parameters used in the PeakFinder tool



Figure 4.8: Localization of the first detected emission for the examined vessel of layup A.

Table 4.3: Maximum sound pressure amplitude recorded in the pressure range [5 - 75] MPa, hydraulic pressure corresponding to the first detected emission and detected peaks for layup A.

Vessel	A_{max} [Pa]	$P_{AE,start}$ [MPa]	N_{hits} [-]
A - 01	4.45	15.5	15
A - 02	2.77	20.4	9
A - 03	4.07	22.3	16
A - 04	5.71	24.8	27
A - 05	3.59	21.7	17
A - 06	7.05	23.3	27
$\mu \pm s$	4.61 ± 1.41	21.3 ± 2.9	19 ± 7

to threshold II. This allows the detection of emissions below 2 Pa. The results are shown in Figure 4.9. From

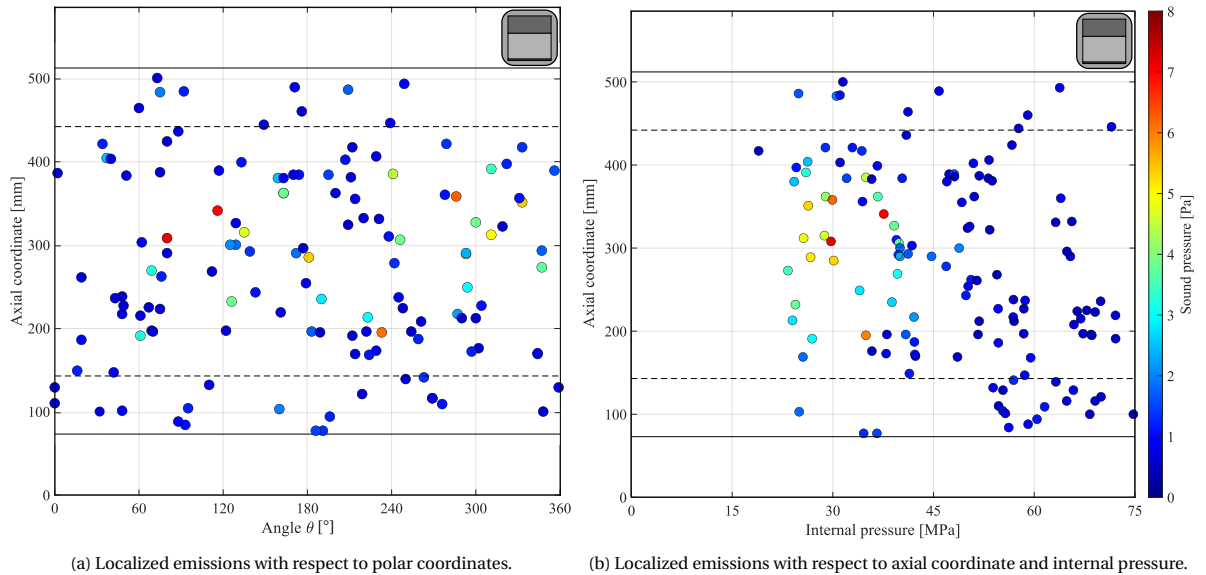


Figure 4.9: Localized emissions plots for layup A.

Figure 4.9a it can be noticed that all the higher amplitude acoustic emissions (above 3 Pa) are localized in the cylindrical section of the vessel. This fact further reinforces the hypothesis that the emissions with higher amplitude can be related to IFF in the hoop layers. The emissions with lower amplitudes are mainly localized in the cylindrical section but some of them can also be found in the domes.

From Figure 4.9b it can be noticed that the first emission occurs at a pressure level just below 20 MPa, and it is

followed by a significant amount of emissions with amplitude above 3 Pa, taking place in the pressure range 20 - 30 MPa. These emissions are all localized in the cylinder except two. The low loading state at which they take place further reinforces the fact that they can be associated to matrix cracking [42, 79, 82]. The pressure range between 30 and 40 MPa is characterized by high and low amplitude emissions, the majority localized in the cylindrical section. Proceeding with the pressurization, some low amplitude emissions are detected in the range 46 - 50 MPa and are localized in the cylindrical section. They are followed by other low amplitude emissions (below 1 Pa) that have been beamformed in both the cylindrical section and the domes. The low amplitude that characterizes these emissions could be associated either to small fracture surfaces or to a damage that takes place deep in the laminate and gets attenuated. This fact will be examined later in the research, when more data will be provided.

4.1.4. Layup D

Layup D is a particular case because it is the only one of the current project without an helical ply as outermost layer. Its stacking sequence is $[(\pm 19.9^\circ)_{11} / (+88.5^\circ, -88.5^\circ)_{15}]$, thus it has 11 helicals on the inside with 30 circumferentials on top. Only one vessel of this layup has been manufactured and it has been subjected to pressurization test up to 105 MPa. Its acoustic file is shown in Figure 4.10.

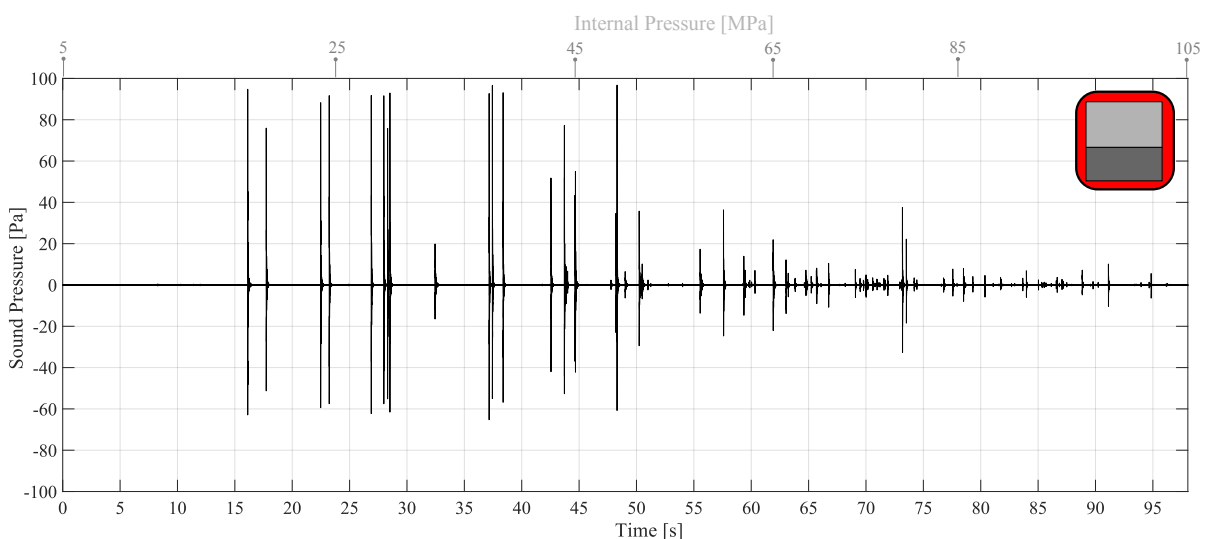


Figure 4.10: Acoustic file of vessel D in the hydraulic pressure range 5-105 MPa.

This layup produces emissions characterized by a significantly high amplitude, some above 80 Pa. The first detected emission can be seen in Figure 4.10 at second 16, which corresponds to an internal pressure of 18.0 MPa. It is then followed by other very high amplitude peaks, until reaching second 47 (which corresponds to about 50 MPa). Emissions of lower amplitude (the majority below 10 Pa) can be detected later and up to the end of the pressurization. The parameters of this layup are summarized in Table 4.4. When lowering the

Table 4.4: Maximum sound pressure amplitude recorded in the pressure range [5 - 105] MPa, hydraulic pressure corresponding to the first detected emission and peaks detected for the only vessel tested with layup D.

Vessel	A_{max} [Pa]	$P_{AE,start}$ [MPa]	N_{hits} [-]
D - 01	96.76	18.0	72

threshold for the localization from I to II, the number of hits increases but not as much as for the previously examined layups. The hits number goes from 72 to 111. The peculiarity of this layup is the absence of a top helical layer. The fact that N_{hits} does not increase as much as the other cases when lowering the detection parameters, could potentially be associated to this feature. It could be speculated that the low amplitude emissions that occur in the other layups can be associated to a damage mechanism taking place in the top helical layer.

The position of the localized emissions can be seen in Figure 4.11. From Figure 4.11a it can be noticed that

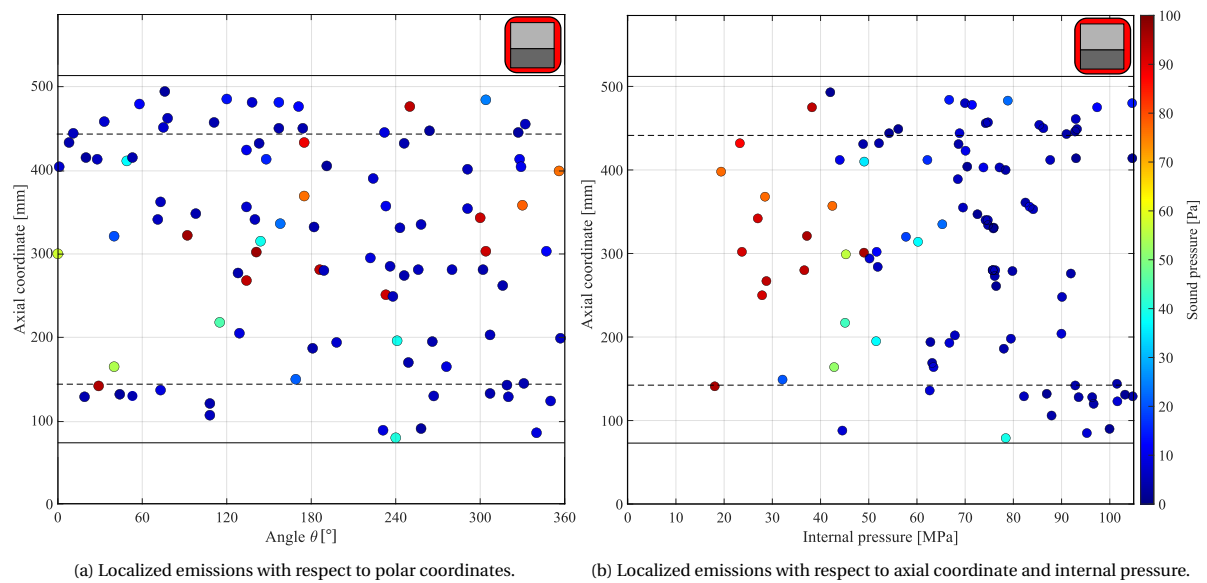


Figure 4.11: Localized emissions plots for layup D.

also layup D follows the trend of the previously examined stacking sequences. All the emissions characterized by higher sound pressure amplitude have been localized in the cylindrical section (except two of them). Due to their significantly high amplitude, it might be hard to associate them to matrix cracking. Matrix cracking usually produces emissions of low amplitude, as shown in Figure 2.17. Fiber failure is associated to events with higher energy release [64, 66]. Looking at Figure 4.11b it can be observed that those emissions take place at early pressure stages (18 to 50 MPa). It is very unlikely that these modest loads could cause fiber failure, thus these significantly high peaks can most likely be associated to IFF in the hoop layers. The important amplitude of the emissions could be caused by the significant size of the fracture surface and to the fact that no helical layers are present on top of the hoops, thus there is no attenuation of the signal. The free boundary effect could also play a role in this configuration, as explained in Paragraph 2.4.2. Talreja and Veer Singh [28] have shown that when the 90° layers are superficial, more work is done during the crack opening by the tractions on the crack surfaces. This can be associated to a higher energy level, thus a higher amplitude of the produced acoustic emission. In the range 50 - 65 MPa some emissions of lower amplitude are present, localized in the cylinder and transition zones. They are followed by emissions (still of low amplitude) that are localized in the cylinder and upper domes, until reaching an internal pressure of 80 MPa. After this stage, the last emissions are mainly localized in the domes. With only the current information it is not clear to which damage mechanism they can be associated. More specific explanations could arise after studying the emissions more in detail as well as the superficial strains with the DIC.

4.1.5. Layup B

Layup B is a particular case of layup C: it is the same but with one of the inner helical layers moved on the outside. Its stacking sequence is $[(\pm 19.9^\circ)_9 / (+88.5^\circ, -88.5^\circ)_{15} / (\pm 19.9^\circ)_2]$. Two vessels of this layup have been manufactured, one subjected to burst and the other to pressurization up to 105 MPa. Layup B has already been extensively used in the department for investigations, thus data of other six vessels are available. However, those have been tested with a different hydraulic pressure rate (3 MPa/s instead of 1 MPa/s). To understand whether and which data could be used for the current research, the three acoustic variables A_{max} , $P_{AE,start}$ and N_{hits} have been compared. Figure 4.12 shows the results of the comparison.

Vessels B-01 and B-02 (depicted in light gray) are the single vessels tested with a pressure rate of 1 MPa/s and the gray bars with black background lines correspond to their average. The single vessels tested with a pressure rate of 3 MPa are denoted with the symbol * and are in green, while their averages are represented in green with white lines in the background. Figure 4.12a shows the comparison of the maximum sound pressure amplitude. The averages of the maximum amplitudes for the two pressure rates are similar and the

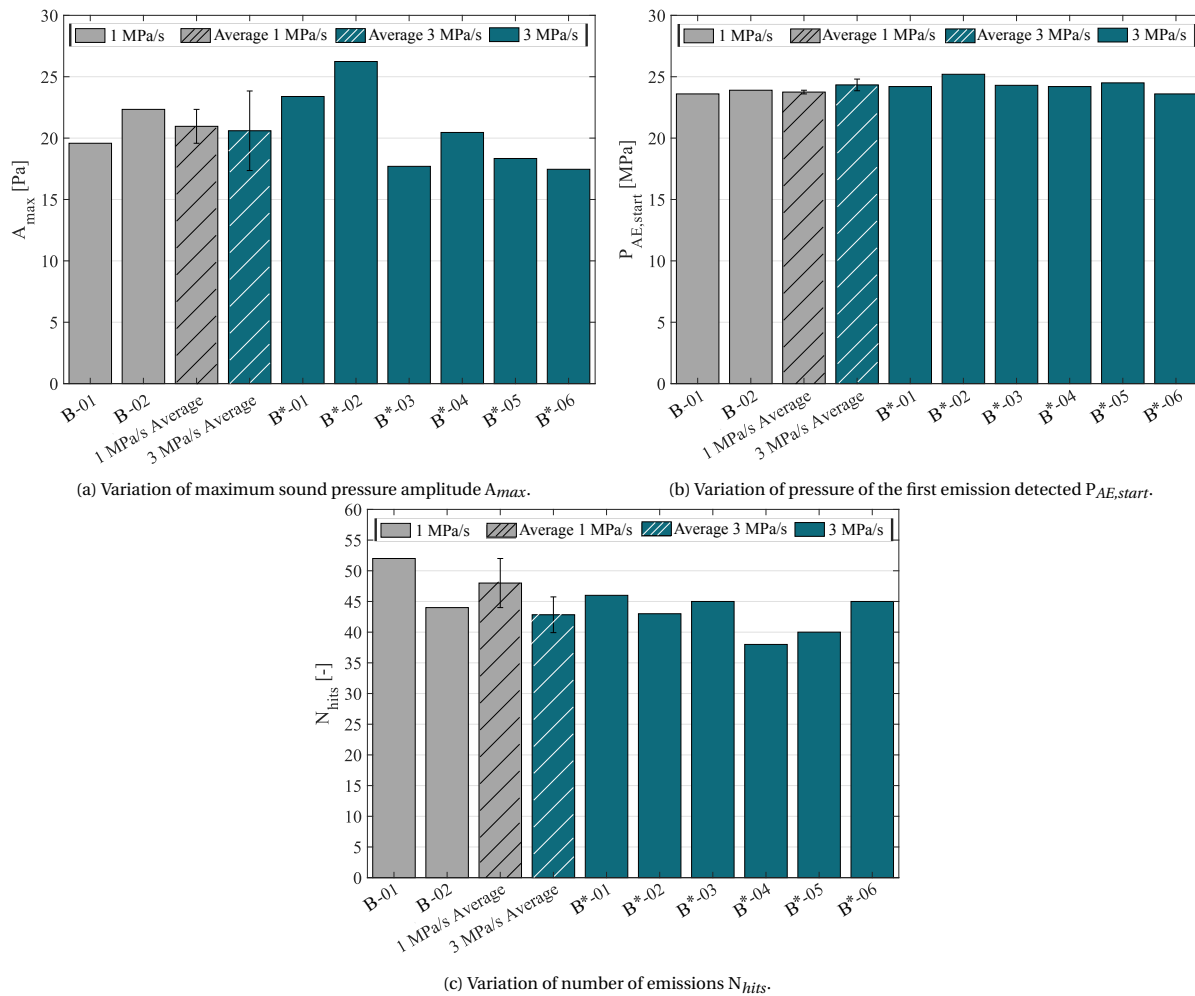


Figure 4.12: Variation of A_{max} , $P_{AE,start}$ and N_{hits} with different hydraulic pressure rates of layout B.

values of B-01 and B-02 are in the scatter region of the B vessels. It has been concluded that the data related to variable A_{max} of the vessels tested with pressure rate 3 MPa/s can be used in the present research. Same outcome was concluded for the hydraulic pressure of the first detected emission as it can be seen in Figure 4.12b. When comparing the amount of emissions (Figure 4.12c) a difference is observable. The average of the emissions of the vessels tested with lower pressure rate is higher than the other and the result of vessel B-01 is not in the scatter of the average of the vessels filled with the higher pressure rate. This outcome could be related to the fact that when testing with higher pressure rates some emissions might overlap, while when lowering it they are more distributed, thus in major number. The data regarding the variable N_{hits} of the vessels tested with pressure rate 3 MPa/s have not been used for the current research. The final results are reported in Table 4.5. The symbol * denotes the vessels tested with a pressure rate of 3 MPa/s. The data in gray in the column N_{hits} are not considered when calculating the average and the standard deviation.

Figure 4.13 shows the acoustic file of the non-burst vessel, pressurized with a rate of 1 MPa/s up to 105 MPa. Looking at Figure 4.13a it can be noticed that the sound pressure amplitudes recorded are similar to those of layout C. This is expected due to the similarity of the two stacking sequences. In Figure 4.13b it is possible to see the acoustic behavior of this layout more in detail. The first 20 seconds of the channel do not present any detectable emission. From second 20, which corresponds to an internal pressure of about 25 MPa, peaks occur, with amplitudes below 10 Pa until second 31. In the next 8 seconds they reach a sound pressure of 15 Pa. The highest amplitude emission occurs at about second 41 and it has a sound pressure amplitude of 22.34 Pa. The range between second 40 and 58 is mainly characterized by peaks of 10 Pa or lower. After second 60 (about 55 MPa), an important amount of small amplitude peaks (below 1 Pa) are present and last until the end of the pressurization.

Table 4.5: Maximum sound pressure amplitude recorded in the pressure range [5 - 105] MPa, hydraulic pressure corresponding to the first detected emission and detected peaks for layup B.

Vessel	A_{max} [Pa]	$P_{AE,start}$ [MPa]	N_{hits} [-]
B-01	19.58	23.2	52
B-02	22.34	23.9	44
B-01*	23.39	24.2	46
B-02*	26.24	25.2	43
B-03*	17.70	24.3	45
B-04*	20.46	24.2	38
B-05*	18.34	24.5	40
B-06*	17.46	23.6	45
$\mu \pm s$	20.69 ± 2.89	24.2 ± 0.5	48 ± 4

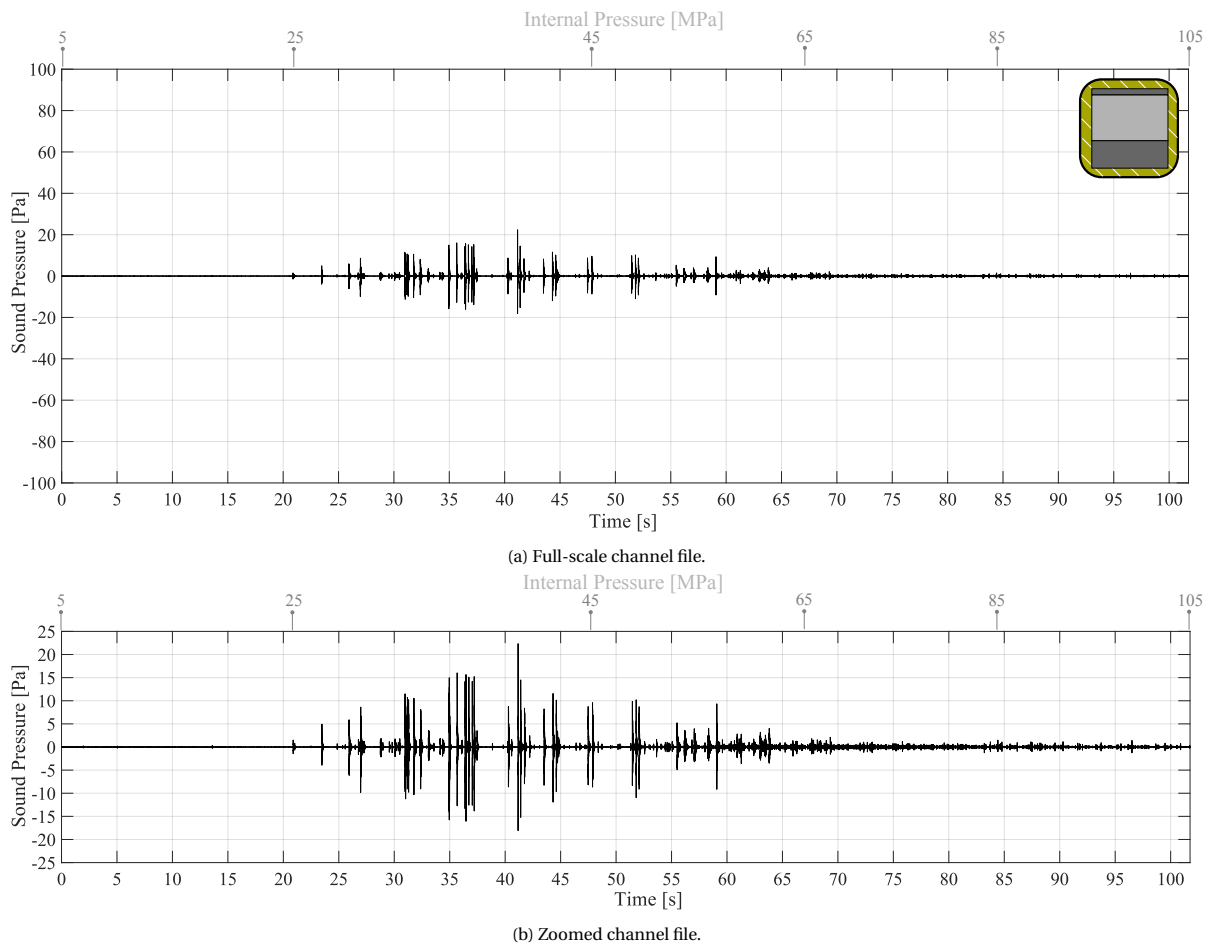


Figure 4.13: Acoustic file of vessel B in the hydraulic pressure range 5-105 MPa.

To get information of the peaks of smaller amplitude, it is necessary to lower the parameters for the `PeakFinder` tool to threshold II. After the post-processing, a total of 186 have been successfully beamformed. The results are shown in Figure 4.14. From Figure 4.14a it can be noticed that all the emissions with higher sound pressure amplitude (above 8 Pa) are localized in the cylindrical section. Due to the similarity in results and stacking sequence with layup C, it can be speculated that these emissions are correlated to IFF in the hoop layers. The high amplitude could be explained by the presence of the single block with 30 circumferential layers, which could create a fracture surface of significant size. Regarding the emissions with lower amplitude, a significant amount have been localized in the cylindrical section and transition zone, less in the domes. Due to their low

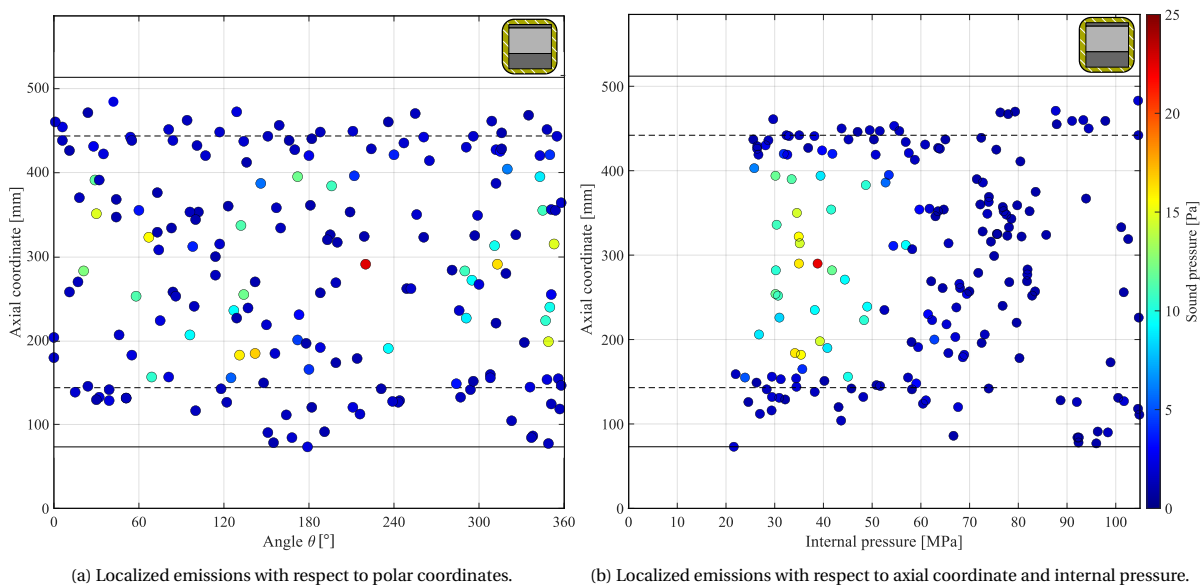


Figure 4.14: Localized emissions plots for layup B.

amplitude they could be related either to damage taking place deep in the laminate that gets attenuated or to more superficial fractures but with a small crack surface.

Figure 4.14b shows the emissions localized with respect to the hydraulic pressure at which they happen. The very first emissions take place in the pressure range between 20 and 25 MPa and are mainly located in the transition zones. This behavior has already been observed when analyzing layup C. It has been attributed to matrix cracking caused by resin rich gaps which are present where the hoops are tapered. The tows sliding during curing and the resin flow could be the cause of this mechanism. The hypothesis is further reinforced by the presence of this effect in layup C and the absence in all the others. The small amplitude of the emissions could be associated to the limited size of the fracture surfaces. These emissions are followed until pressure stage 50 MPa by two sets of peaks: those of higher amplitude (above 8 Pa) all beamformed in the cylinder and those with amplitudes below 5 Pa, localized mainly in the transition zones. The fact that the higher amplitude peaks take place at early pressure stages, reinforces the hypothesis that they could be related to matrix cracking [42, 79, 82]. The pressure range 50 - 60 MPa is characterized by few emissions but it is followed by a significant amount of low amplitude emissions localized in the cylindrical section. From pressure stage 85 MPa on, only few emissions are localized and the majority of them are in the domes. The distribution of the emissions of low amplitude cannot be explained yet. However, if they are related to superficial damage it should be visible when analyzing the superficial strain data, calculated with DIC.

4.1.6. Discussion

From the analysis of the acoustic data it is possible to highlight some trends which are both general and layup-specific. Thanks to those, some hypotheses can be formulated. Considering the totality of the layups, the emissions with higher amplitude take place in the first stages of the pressurization and are mainly located in the cylindrical section (except few outliers). This leads to the hypothesis that they can be related to IFF in the hoop layers [42, 79, 82]. This hypothesis is further reinforced when taking into account the amplitude of these peaks. They follow the trends found in literature, explained in Paragraph 2.4.2. It is shown that these amplitudes vary according to the amount of stacked hoops (thus the created fracture surfaces [30, 68]) and their location through the thickness of the laminate [30, 82]. However, to prove the hypothesis it is necessary to evaluate them with some damage inspection systems, such as CT.

Another aspect that is common to all the layups is the presence of emissions of lower amplitudes. They are detected when lowering the parameters in the PeakFinder tool to threshold II. They are localized through the entire height of the vessel. It seems that their location varies in each vessel depending on the internal

pressure. Due to the low amplitude that characterizes these peaks, it is supposed that they can be associated either to damage taking place deep in the laminate that gets attenuated or by damage more superficial with small fracture surfaces. However, when analyzing layup D (the only one without helicals as outermost plies), it is noticed that the increase in N_{hits} when lowering the parameters in the PeakFinder tool to threshold II is not as high as for all the other stacking sequences. This brings to the hypothesis that those peaks are somehow related to the superficial helical layer. If this is the case, it could be explained analyzing the superficial strains, obtained with the DIC analysis. Layups B and C have a peculiarity that is not present in the other analyzed stacking sequences. Some emissions of smaller amplitude are also detected at the beginning of the pressurization and localized in the transition zone. They are possibly caused by resin rich gaps present due to hoops tapering. From the information gathered only from the acoustics, this hypothesis cannot be proven.

4.2. Damage Differentiation Combining Acoustics and Visual Inspections

After describing the acoustic behavior of each layup, it is necessary to prove the hypotheses formulated. A first step in this direction could be identifying which damage mechanisms are causing the acoustic sources. For the purpose, the pictures of the vessel taken at different stages can be compared. The side covered with chalk powder has been selected for the purpose, because the formation of superficial damage can be identified. The layups considered are D, B, A and E. C is not present because no experiments with chalk applied have been performed. Due to the similarity in stacking sequence and acoustic behavior to layup B, it is supposed that the two layups will follow similar trends.

Before analyzing the damage creation with the chalk powder, it is necessary to provide some considerations regarding the beamforming. These are explained in Paragraph 4.2.1. Afterwards, each layup will be analyzed separately, comparing its acoustic behavior previously described with pictures taken during the pressurization to the side where the chalk powder had been applied.

4.2.1. Considerations about the Time Interval of the Beamforming

It is necessary to explain how the time interval for the beamforming was chosen. In the current paragraph some results that will be explained in detail later are shown in advance. This was fundamental for the understanding of the basic decisions taken when performing the emissions localization.

During the research, it was discovered that the beamforming algorithm implemented in the software was highly dependent on the time interval chosen. This interval had been identified in previous researches, after making a small experiment. Five piezo signal generators had been glued to a vessel and the signal produced had been beamformed. It was concluded that the best time interval was $500 \mu s$. It must be taken into account that the algorithm implemented in the software assumes a point source. This assumption is incorrect when trying to localize certain emissions produced by the vessel. An example is here reported. The emissions of higher amplitude in layup D are associated to the formation of damage in the cylindrical section. A ring that propagates through the entire circumference of the vessel is associated to each AE. This has been observed looking at the videos of the pressurization. This damage can be associated with IFF in the hoops. In Figure 4.15 it is shown one of these emissions (emission 4). The first microphones triggered in the testing chamber are marked with black markers, while those recording the maximum sound pressure amplitude in red. It can be noticed that the four microphones recording the maximums are spread all around in the chamber. This means that it is incorrect to identify the emissions as point sources.

Figure 4.16a shows the location of the IFF that caused emission 4, which corresponds to the center of the vessel. When using the predefined time interval ($500 \mu s$) during the beamforming process, the emissions of higher amplitude were not localized in the correct location, as shown in Figure 4.16b. Also increasing the time interval to, for example, $900 \mu s$ was not providing a correct location (Figure 4.16c). Looking at Figure 4.15 it can be noticed that the first microphones triggered are located close to each other, on two adjacent walls. This means that the fracture started on one point and quickly progressed into a ring. It was speculated that using a small interval during the beamforming, the emission could be considered as point source. In Figure 4.16d it is shown the beamforming of emission 4 with a time interval of $63 \mu s$. It can be noticed that its location is correct. For this reason, for the beamforming of the emissions of higher amplitude it has been

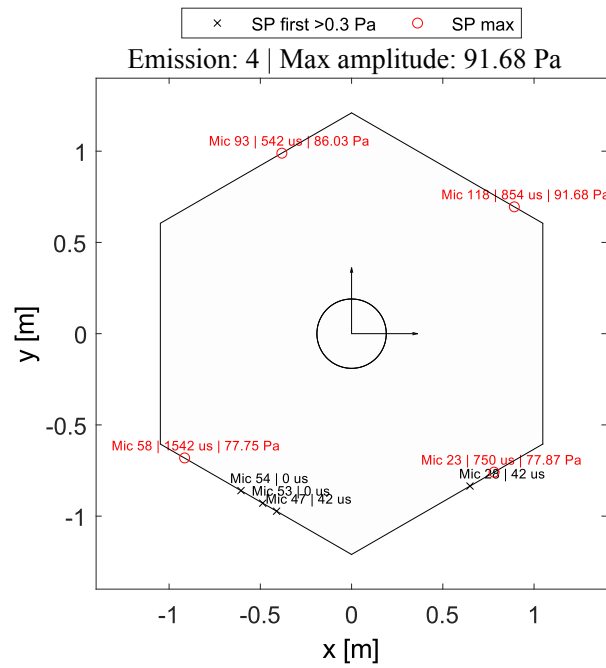
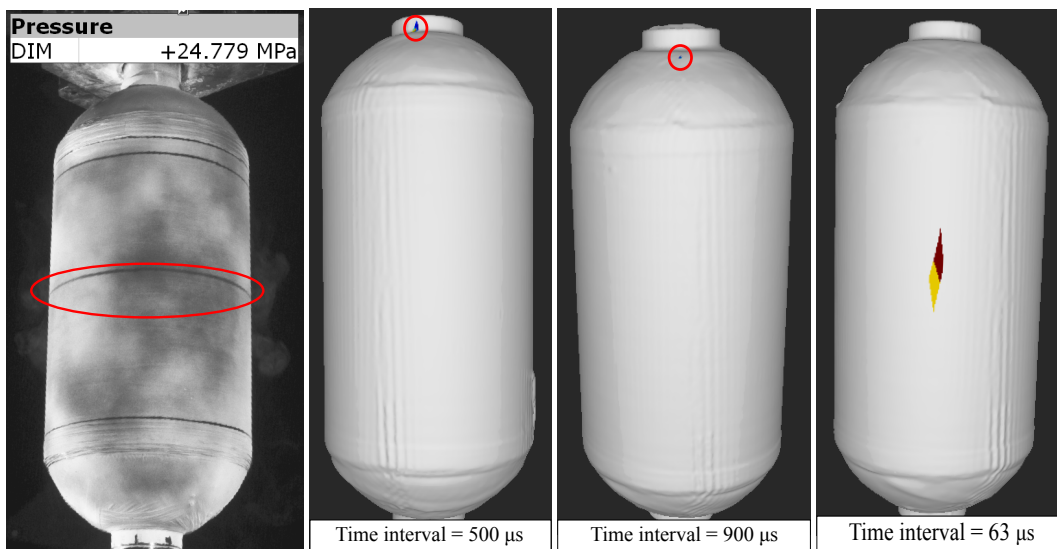


Figure 4.15: Example of microphones triggering for emission 4 of layup D.



(a) IFF causing emission 4. (b) Beamforming of emission 4 with at time interval of 500 μ s. (c) Beamforming of emission 4 with at time interval of 900 μ s. (d) Beamforming of emission 4 with at time interval of 63 μ s.

Figure 4.16: Emission 4 of layout D: IFF location and beamforming with different time intervals.

decided to use small time intervals, varying from 42 to 125 μ s.

Looking at the video of the pressurization of layout A, it was noticed that when the emissions of smaller amplitude were taking place, it was possible to see the chalk detaching from the vessel surface and dark marks were appearing. An example is shown in Figure 4.17a in the red circle. The emission associated to this damage has been beamformed and it was found a correlation in location. Since this kind of damage is located in a specific spot on the surface, the type of acoustic source related to it can be seen as punctual. This has been proven using different time intervals during the beamforming. Figures 4.17b, 4.17c, 4.17d and 4.17e show the emission localization with a time interval of respectively 83 μ s, 250 μ s, 500 μ s and 1500 μ s. It can be observed that the location is correct and it does not change.

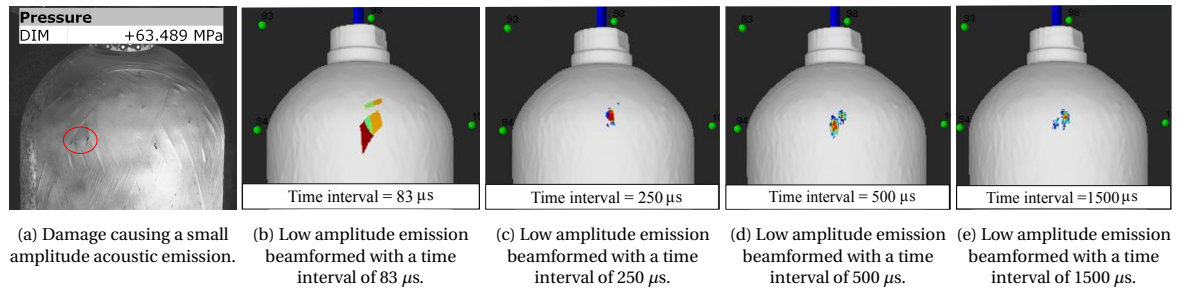


Figure 4.17: Same low amplitude emission beamformed with different time intervals.

As a conclusion, it has been decided to use small time intervals (in the range 42 - 125 μ s) when localizing the emissions with higher amplitude and the usual 500 μ s for the smaller peaks.

4.2.2. Layup D

The first layup considered for damage identification is D, the one without a helical as outermost layer. Figure 4.18 has already been described in Paragraph 4.1.4, but it is reported here to make the understanding easier. It shows the relation between the axial position of the acoustic emissions, their sound pressure amplitude and the internal pressure at which they occur. Layup D is characterized by emissions of high sound pressure

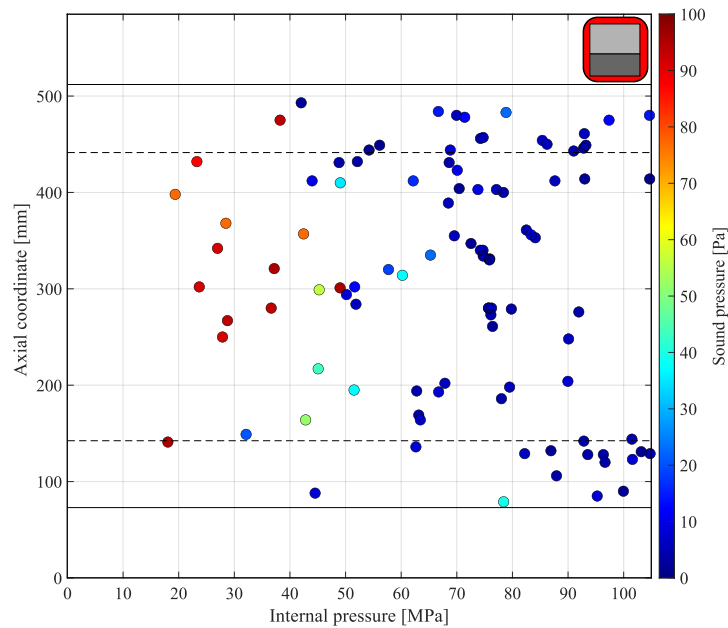


Figure 4.18: Acoustic file of vessel D in the hydraulic pressure range 5-105 MPa.

amplitude until pressure stage 60 MPa, followed by others of lower amplitude. Figure 4.19 shows the vessel at three different pressure stages: before the pressurization, after the occurrence of the emissions of higher amplitude and at the end of the pressurization. Figure 4.19a corresponds to the unpressurized stage and it is taken as reference. Figure 4.19b is captured at a pressure stage of 61 MPa. It is possible to notice that some chalk has fallen, due to the creation of damage. Rings in the cylindrical section are visible, only where the hoop layers are wound. Looking at Figure 4.18 it can be seen that the emissions with higher sound pressure amplitude are almost all localized in the cylindrical section. They can be associated to interfiber-fracture in the circumferential layers, as previously speculated. To further investigate the link, some of these emissions are analyzed more in detail. The hydraulic pressure at which one peak is detected is recorded and the emission peak is localized on the vessel. Then a picture of the vessel at the same pressure stage is taken and compared to the previous one. An example can be seen in Figure 4.20. The picture on the left is taken from the software NoiseImage and it corresponds to the result of the beamforming of emission 4. Figures 4.20b

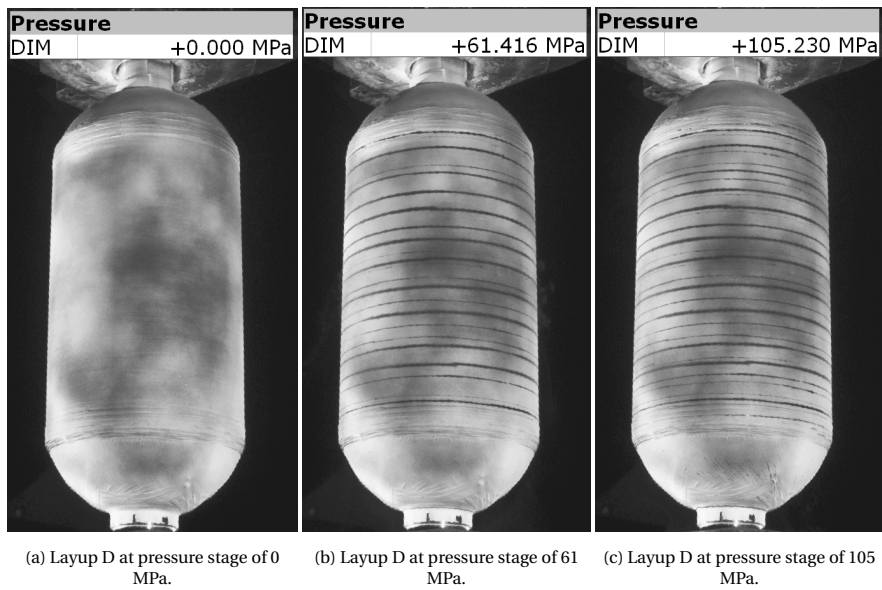


Figure 4.19: Layup D at different stages of the pressurization.

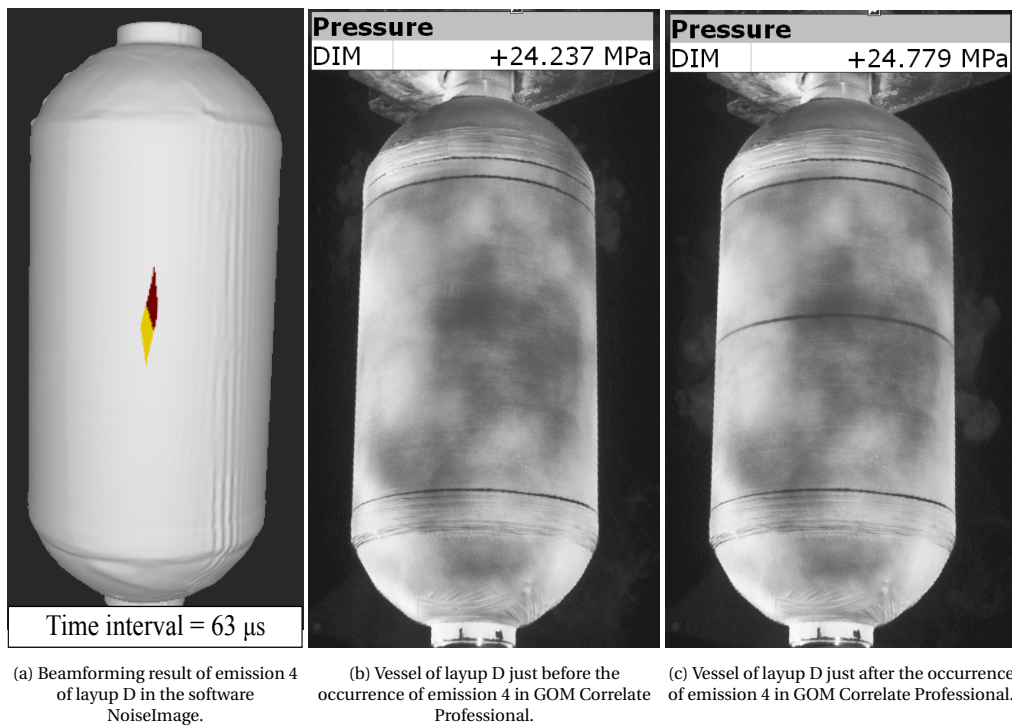


Figure 4.20: Beamformed emission and corresponding damage creation.

and 4.20c are taken respectively just before and after the pressure stage at which emission 4 occurred. It can be noticed that there is a correspondence between the location in which the emission is beamformed and the position in which the damage occurred. The same investigation has been performed for all the emissions that occurred in the pressure range between 18 and 61 MPa. For all the cases (except one) have been found similar results to those just described. The acoustic sources occurring in this pressure range reach a significant amplitude because the sound pressure of each event can be related to the energy released due to the damage formation and to the important fracture surface [30, 68]. Once the crack is started, it is free to develop and it is stopped only where there is a change in orientation [31], thus it runs through the entire block of hoop layers. The free boundary effect also plays a role in this layup, as explained in Paragraph 4.1.4. This is caused

by presence of the 90° layers on the surface which cause a higher work during crack opening [28]. It can be concluded that the high amplitude emissions taking place in the pressure range 18 - 60 MPa are associated with IFF in the circumferential layers.

The second part of the pressurization is characterized by emissions of lower amplitude, localized in the cylinder and dome region. Comparing Figure 4.19c with Figure 4.19b it can be noticed that there is a progression of damage. More chalk has fallen from the cylindrical section and few less marked rings have been created. The fact that the new lines are less visible than the previous ones could be related to the lower amplitude of the emissions and thus a smaller energy release. This could be linked to the superficiality of the damage. The same hypothesis could be developed when looking at the domes in Figure 4.19c. Some marks can be seen in these areas due to the fallen of the chalk powder at the end of the pressurization. The marks follow the direction of the wound layer. Also here the signs are not overly pronounced and can be associated to the emissions taking place at the end of the pressurization. Since in the domes there are no circumferential plies, there is a change in winding direction in each helical ply (one helical layer is wound at both $\pm 19.9^\circ$). The crack is stopped after just one layer, thus its fracture surface is limited. This could explain why the emissions localized in that area are characterized by lower sound pressure amplitude.

4.2.3. Layup B

The acoustic behavior of layup B is reported in Figure 4.21. The first 50 MPa of the pressurization are char-

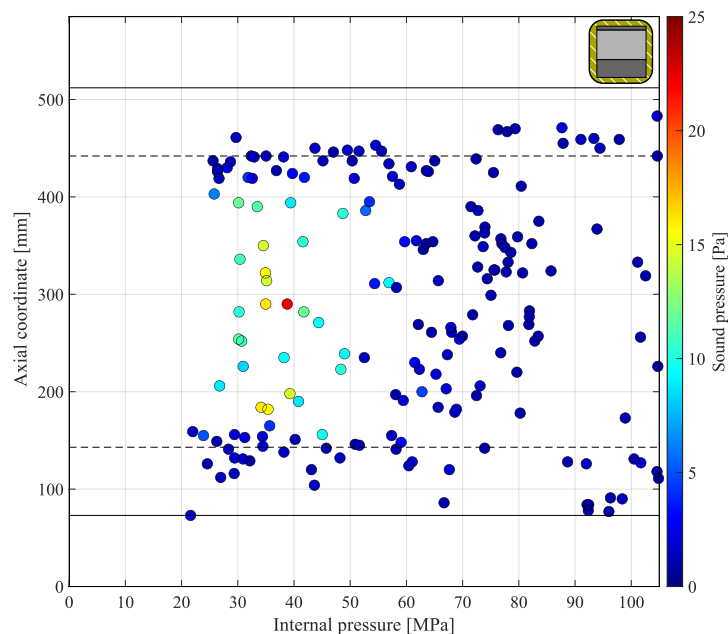


Figure 4.21: Acoustic file of vessel B in the hydraulic pressure range 5-105 MPa.

acterized by emissions mainly occurring in the cylindrical section and transition zone. Figure 4.22b is taken at a pressure stage of 50 MPa. No visible damage can be seen when comparing it to Figure 4.22a, which corresponds to the unpressurized stage. This means that damage is not superficial but it happens inside the laminate. As for layup D, the emissions of higher amplitude are all beamformed in the cylindrical section and take place at the beginning of the pressurization. It is likely the case that these emissions correspond to the same damage mechanism: IFF. This cannot be detected by visual inspection because the hoops are not the superficial plies. Two main differences can be noticed comparing these emissions with those of layup D. The latter reach a sound pressure amplitude which is 4 times higher (even if the amount of circumferential layers is identical) and that they start earlier, around 18 MPa instead of 26 MPa. Both differences could be explained by the presence of helical layers as outermost plies. When the crack is formed, the acoustic source is produced but its sound pressure is attenuated by the top helicals and lowered before reaching the acoustic sensors. The helical plies also restrict the separation of the two surfaces of the crack, reducing the work done in comparison with layup D in which the free boundary effect was taking place. This causes a lower energy

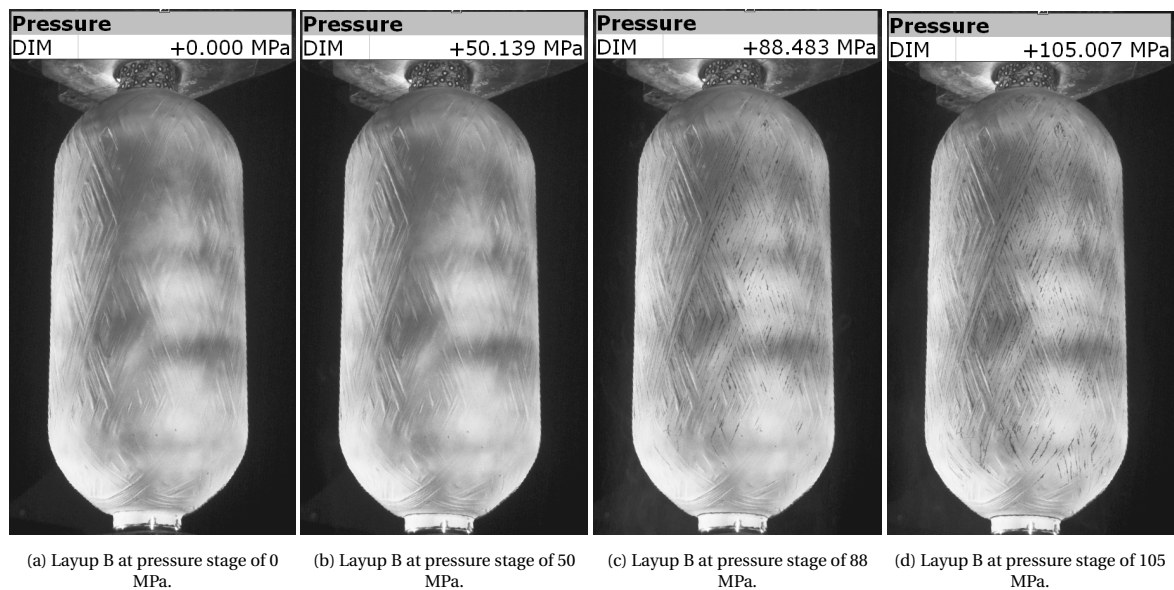


Figure 4.22: Layup B at different stages of the pressurization.

release and a lower amplitude of the acoustic source. The constraining effect performed by the helicals on the hoop layers could also be the reason of the delay in the occurrence of the first emission.

In the same pressure range, some emissions of lower amplitude also occur, which have mainly been beamformed in the transition zones. As for the others, no superficial damage can be seen in Figure 4.22b, which is why it is concluded that the damage takes place on the inside of the laminate. Due to the low pressure stages at which it is happening, it might be related to matrix cracking [42, 79, 82] and since it is not visible, it must be in the internal layers. Few hoop layers are present in the transition zone, tapered towards the domes. Due to friction, fiber tension and to resin flow during curing, they might slightly slide. This could create small gaps between the bottom block of helicals and the outermost ones. Due to the compaction effect of the domes during the curing, this gap could be filled with resin and cause premature matrix cracking, which could be associated to these emissions. A similar trend can be observed in C (Figure 4.2b). Due to the similarity of the two layups, similar behaviors are expected.

The pressure range between 50 and 88 MPa is characterized by acoustic emissions of amplitude below 5 Pa mainly localized in the cylindrical section. Figure 4.22c shows the vessel at pressure stage 88 MPa. It can be noticed that some chalk powder has fallen, in particular in the cylindrical section of the vessel. The emissions could be linked with matrix cracking in the top helical. To further prove this, as already done for layup D, some emissions have been beamformed and their pressure recorded. Pictures just before and after that pressure stage are compared in order to verify whether there is a link between the damage formed and the acoustic. An example is shown in Figure 4.23. In the red circle of Figure 4.23c it can be noticed that some chalk powder is missing if compared to the previous pressure stage, shown in Figure 4.23b. The position matches with the location in which the emission has been beamformed and this has been confirmed for multiple emissions. It can be concluded that the low amplitude emissions happening later in the pressurization can be associated with superficial damage, identified as matrix cracking. This damage is caused by the presence of external helical layers. This can be concluded by comparing the amount of detected emissions when changing the thresholds of the PeakFinder tool. Since the emissions taking place at higher pressure stages are all characterized by a low amplitude, they are not detected when the amplitude threshold is set to 2 Pa. They are identified when lowering the same parameter to 0.3 Pa. Table 4.6 shows the increase of detected emissions when lowering the parameters of the PeakFinder tool from threshold I to II. Layup A is in gray because its values are calculated in the pressure range 5 - 75 MPa, while the rest of the vessels in 5 - 105 MPa.

For layup D the increase is significantly lower with respect to the others and this vessel is characterized by the absence of helical layers as outermost plies. It can be concluded that the emissions of lower amplitude hap-

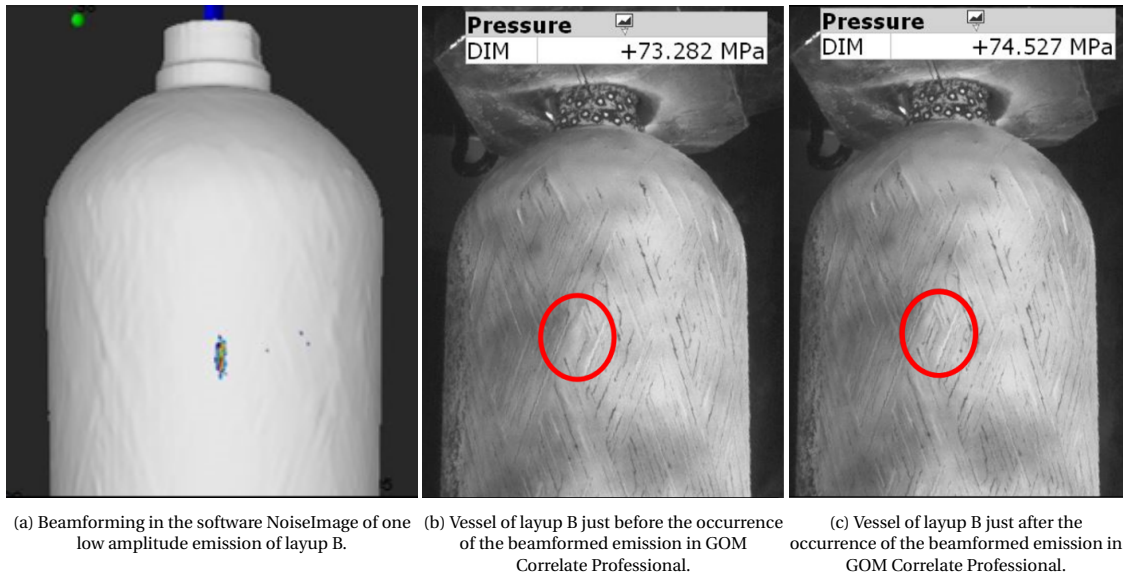


Figure 4.23: Beamformed emission and corresponding damage of an acoustic source of low pressure amplitude of layup B.

Table 4.6: Hits detected by the PeakFinder tool when using thresholds I and II and percentage increase.

Layup	N_{hits} Threshold I [-]	N_{hits} Threshold II [-]	N_{hits} increase [%]
A	27	134	396
B	48	248	463
C	51	246	382
D	72	111	54
F	1	64	6300

pening at late pressure levels are relatable to the presence of the superficial helical layers. The marks caused by the falling of the chalk are shaped as straight lines. These lines are oriented in the same direction of the helical tows and they are formed at the sides of each band. They also stop when there is an intersection of the bands. This damage could be caused by two effects. The first and most probable one is related to the tangential stresses that act towards the matrix and transversally to the tows which can cause a crack. The second could be linked to the Poisson effect. During the pressurization, the vessel axially deforms. This makes the fiber bands strain in the axial direction and contract transversally, causing some cracks in the matrix at the sides of the bands. Both the effects could explain why the marks are appearing at higher pressure stages and why they are located at the sides of the tows and shaped like straight lines, at least in the cylindrical section. It can be concluded that the emissions taking place in the pressure range 50 - 88 MPa can be associated to matrix cracking of the superficial helical. The same outcome has been concluded for the emissions taking place from 88 MPa until the end of the pressurization: they have mainly been beamformed in the domes. In Figure 4.22d it can be noticed that some chalk is missing in those areas.

4.2.4. Layup A

The next vessel analyzed is layup A and its emissions are shown in Figure 4.24. The peaks start just below 20 MPa and up to 40 MPa can be divided into two categories: those of higher amplitude, all localized in the cylindrical section and some of lower amplitude, located both in the dome and in the cylinder. When comparing Figure 4.25a and 4.25b, which correspond to the internal pressures of 0 and 40 MPa respectively, no differences can be noticed. This means that the damage is not superficial but it takes place internally in the layup. The same assumptions made in Paragraph 4.2.3 for layup B are valid and for the same reasoning they could be related to IFF in the hoop layers of the cylindrical section. There is an important difference between the two cases which is the sound pressure amplitude of the emissions. For layup B the maximum recorded pressure corresponds to 23.6 Pa while for layup A it is 7.05 Pa. As already speculated, this difference could

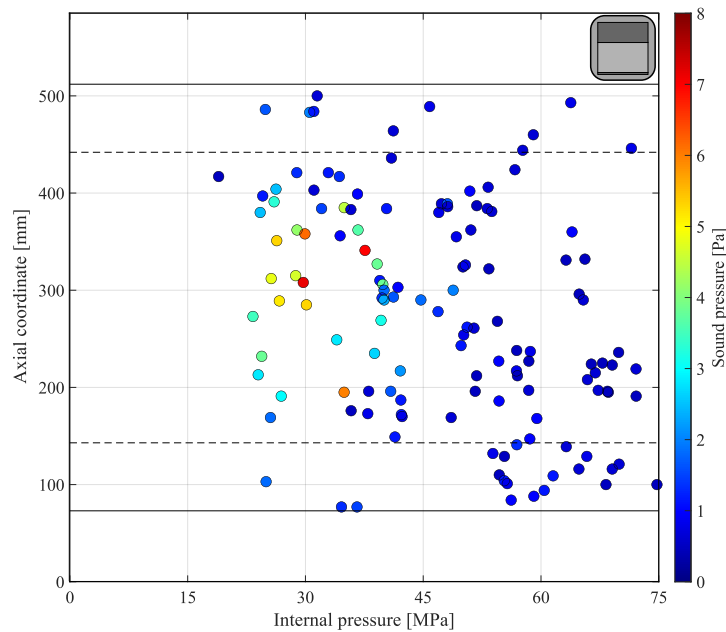


Figure 4.24: Acoustic file of vessel A in the hydraulic pressure range 5-75 MPa.

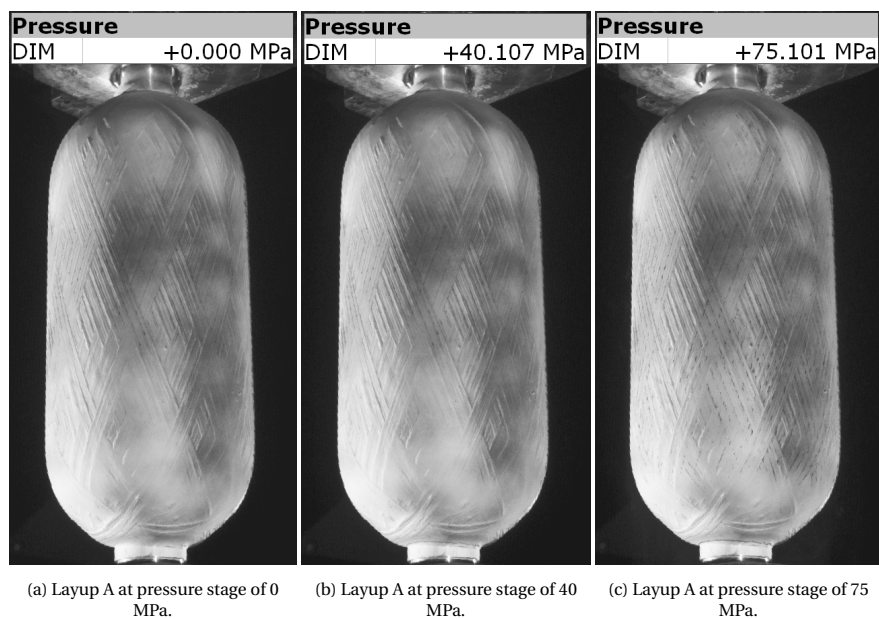


Figure 4.25: Layup A at different stages of the pressurization.

be explained by comparing the stacking sequence of the two vessels. The amount of circumferential layers stacked together is the same, but the positioning in the layup is different. In fact, while layup B only has two helical layers on top of the hoops, layup A has 10. This block of helicals could attenuate the sound pressure of the acoustic emissions, causing a lowering of their amplitude [30, 82]. It can be concluded that the acoustic emissions with higher sound pressure amplitude can be associated with IFF in the hoops. In the same pressure range, also some emissions of low amplitude are present, which don't cause any superficial damage. Due to the low pressure stages in which they take place, they might be related to matrix cracking happening in the innermost layers.

After pressure stage 40 MPa, the acoustics of layup A is characterized by peaks of low amplitude (below 2 Pa), mainly localized in the cylindrical section and transition zones. Figure 4.25c shows the vessel at the end of

the pressurization. As for the previous layups, it is possible to see that some chalk has fallen from the vessel, leaving dark marks. The marks are shaped as straight lines and follow the direction of the tows, stopping where there is an intersection between bands, as for the previous layup. It can be concluded that those emissions correspond to matrix cracking in the superficial layer. It can be observed that the marks are not in large numbers when compared to the amount of emissions, particularly in the domes. This means that the emissions are not taking place superficially but most likely from the inner layers. This could be explained by the presence of 10 helical layers on the outer side. It might happen that not only the outermost layer cracks, but also the others. Due to the continuous change in direction, the cracks only go through single plies, thus they produce an acoustic emission but they cannot be seen on the surface of the vessel. This fact could be proven after having the results from the CT scans. Another factor that might play a role is layers compaction. It has been noticed that whenever the hoops are positioned above the helicals, they tend to compact the latter during curing. This causes air release and resin flow towards the surface. This results in a superficial resin layer as shown in Figure 4.26a. In layup A, the circumferentials are below the helicals, thus this effect is not present. This leaves a dry vessel surface, as visible in Figure 4.26b. Few emissions are also localized in the transition

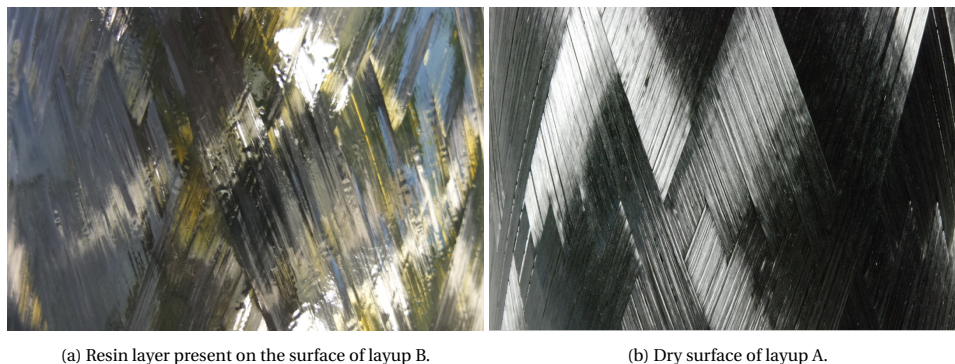


Figure 4.26: Surface comparison of layups B and A.

zones and domes, but nearly no damage is visible in those areas. This could be linked to the stresses being higher on the inside and causing cracks in the innermost layers first. The latter hypothesis needs more research to be verified.

4.2.5. Layup F

The acoustic behavior of layup F is shown in Figure 4.27. The first part of the pressurization, up to 50 MPa is characterized by emissions localized in the bottom transition zone and dome. These are caused by the presence of a ring with air inclusion in forms of bubbles in that area. This fact has already been explained extensively in Paragraph 4.1.2. Figure 4.28b shows the marks in the bottom transition zone related to those emissions in the red circle.

The pressure range 50 - 61 MPa is characterized by the highest amplitude emissions for this layup, even if the maximum sound pressure is just above 2 Pa. They are mainly localized in the transition zones and the cylindrical section. This situation is different from the cases previously examined. In fact, the first emissions localized in the cylindrical section take place much later, at about 48 MPa (for the other vessels it is between 18 and 24 MPa). Furthermore, their sound pressure amplitude is significantly lower than for the other vessels. If these emissions are associated with IFF, their lower amplitude could be explained by the size of the fracture surfaces. All the vessels studied have the same amount of circumferential layers. While the previously investigated ones have all the hoop plies stacked in one group, layup F has the circumferentials divided in five groups, separated by helical layers. Each block of circumferentials is made of six plies. When a crack in the hoops is formed, it is stopped by the change in orientation caused by the presence of the helical layers. This reduces the length of the fracture surface, thus the energy released and as a consequence the sound pressure amplitude [68]. Looking at Figure 4.28c it can be noticed that some chalk has fallen from the top transition zone and few marks are present also in the cylindrical section, which could be related to the few emissions detected in that zone. Due to the few information, the damage taking place in this pressure range cannot be clearly defined.

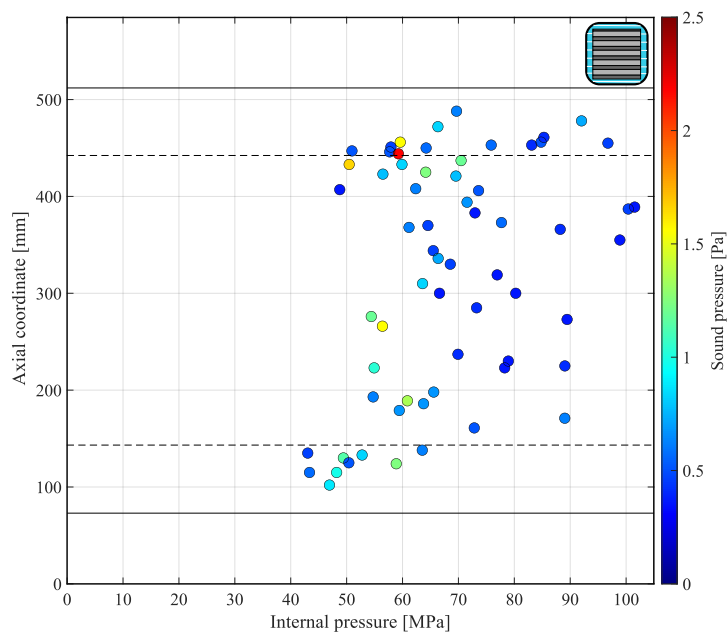


Figure 4.27: Acoustic file of vessel F in the hydraulic pressure range 5-105 MPa.

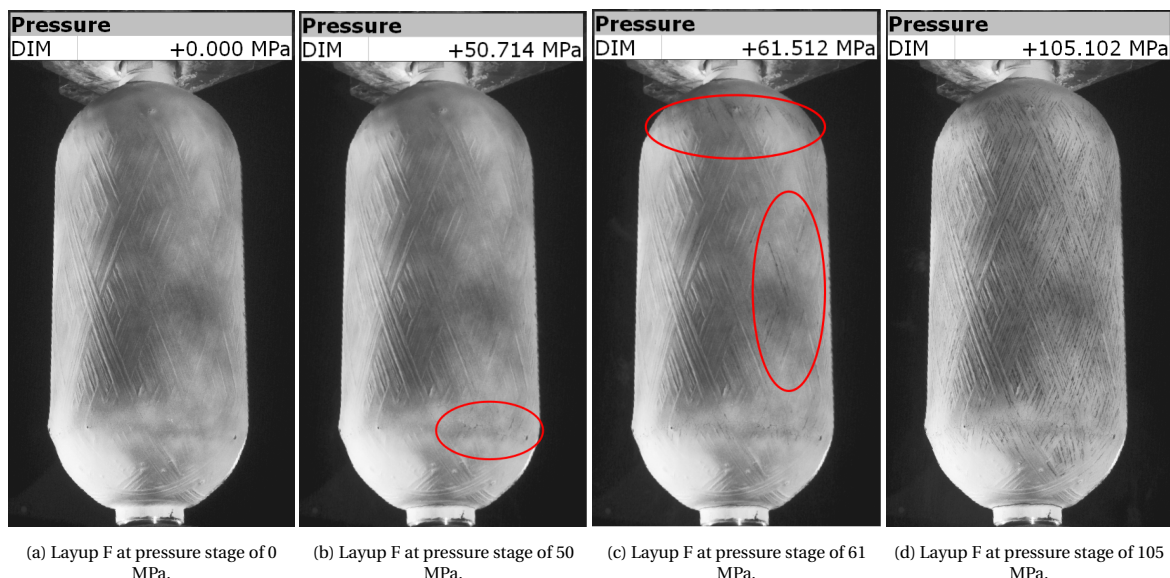


Figure 4.28: Layup F at different stages of the pressurization.

From the pressure stage 61 MPa to the end of the pressurization, some more emissions have been beam-formed. Figure 4.28d shows the vessel at the end of test. It can be seen that an important amount of chalk is fallen, leaving clear marks on the surface. The marks are similar to the ones of the other vessels and can be associated to matrix cracking in the superficial layers. Looking at Figure 4.27, it can be noticed that the emissions localized are fewer than those for the other layups and the visible marks are in greater number. This means that not all the emissions produced by the vessel are detected by the system. The minimum sound pressure amplitude detected by the system is 0.3 Pa and all the emissions below the threshold are not considered. A factor that can also play a role is the distance between the sound pressure sensors and the vessel. The sound pressure amplitude can be highly reduced when passing through the air. It can be concluded that the system used for the analysis is not able to detect all the acoustic emissions produced by the vessels. The reason why this fact is evident only in this layup is not clear. Since the damage considered is matrix cracking in the outermost helical, the superficial strains distribution might be a factor to take into account. This will

be investigated with the DIC strain data in Paragraph 4.4.

The link between acoustics and damage mechanisms, taking into account the amplitude of the emissions, the hydraulic pressure at which they take place and the visibility of the damage has been analyzed. The emissions that take place at the beginning of the pressurization are usually characterized by the highest sound pressure amplitudes and are always beamformed in the cylindrical section. This led to the hypothesis that they correspond to IFF taking place in the hoop layers. This fact is proven for layup D while further inspection is necessary for the other stacking sequences. The inspection has been performed using CT and the results are described in Paragraph 4.3. The sound pressure amplitude and the starting pressure of the emissions have been found to be linked with the grouping and positioning of the hoop layers. This topic will be studied more in detail in Paragraph 4.5. The emissions occurring at higher pressure stages and characterized by low amplitude are relatable with matrix cracking taking place in the outermost helical layer. This has been proven looking at the fallen of the chalk. The acoustic system used in the investigation has been found to be not capable of detecting all the emissions produced by the vessels, as shown in Paragraph 4.2.5.

4.3. Damage Inspection

In the previous paragraph it was concluded that the emissions of higher sound pressure amplitude are relatable to IFF in the hoop layers. Since in all the layups (except D) the circumferential layers are not visible, it is needed to prove that this type of damage is present. It must also be proven that the superficial damage that has been linked to matrix cracking in the outermost helical layer is visible. In this paragraph, the results of the CT scanning of the layups B, A and F will be described. The procedure regarding the specimen preparation has already been explained in detail in Paragraph 3.5. The emissions selected for each layup are those of higher amplitude that have been beamformed in the cylindrical section.

4.3.1. Layup B

Figure 4.29 shows the scan of a specimen cut from a vessel with layup B, subjected to a pressurization up to 105 MPa. The specimen is taken from the cylindrical section, where a high amplitude emission has been beamformed. The three main blocks of layers can be seen in Figure 4.29a: the top one corresponds to two helical plies, followed by 30 circumferentials and ending with other nine helicals. In the middle of the picture in the red box it can be noticed a crack, located in the hoops. Figure 4.29b is a zoom of this crack. It runs through the entire block of circumferential layers and it is stopped where the helicals start, which is in agreement with what found in literature [31]. It can be concluded that the acoustic emissions of higher amplitude can be related to IFF in the hoop layers. It can also be observed that the change in orientation of the layers acts as a crack stopper.

In Figure 4.29a other cracks with a smaller length, located in the top helical layers are also present. They are marked with blue boxes and are shown in detail in Figure 4.29c and 4.29d. This scan proves that the low amplitude emissions visible as black marks on the surface of the vessel correspond to matrix cracking. Even though this damage is superficial, the fracture surface of the cracks is significantly small, from which the low amplitude of the emissions [68].

4.3.2. Layup A

The next layup analyzed is A. After the pressurization test, some of the emissions with higher amplitude have been localized in the cylindrical section. Specimens from those areas have been cut and CT scanned. The results are shown in Figure 4.30. Figure 4.30a shows the full height of the laminate, in which it is possible to distinguish the top 10 helical layers, followed by the block of hoops and the bottom single helical. Figures 4.30b and 4.30c show a zoom on the cracks present in the hoops (red box) and top helical layers (blue box) respectively.

IFF in the hoop layers is present in the location where an emission of higher amplitude is detected, as for the previous case. The crack runs through the entire thickness of the block of hoops and stops only where there is a change in direction of the wound layers. In Figure 4.30b it is possible to observe that an important

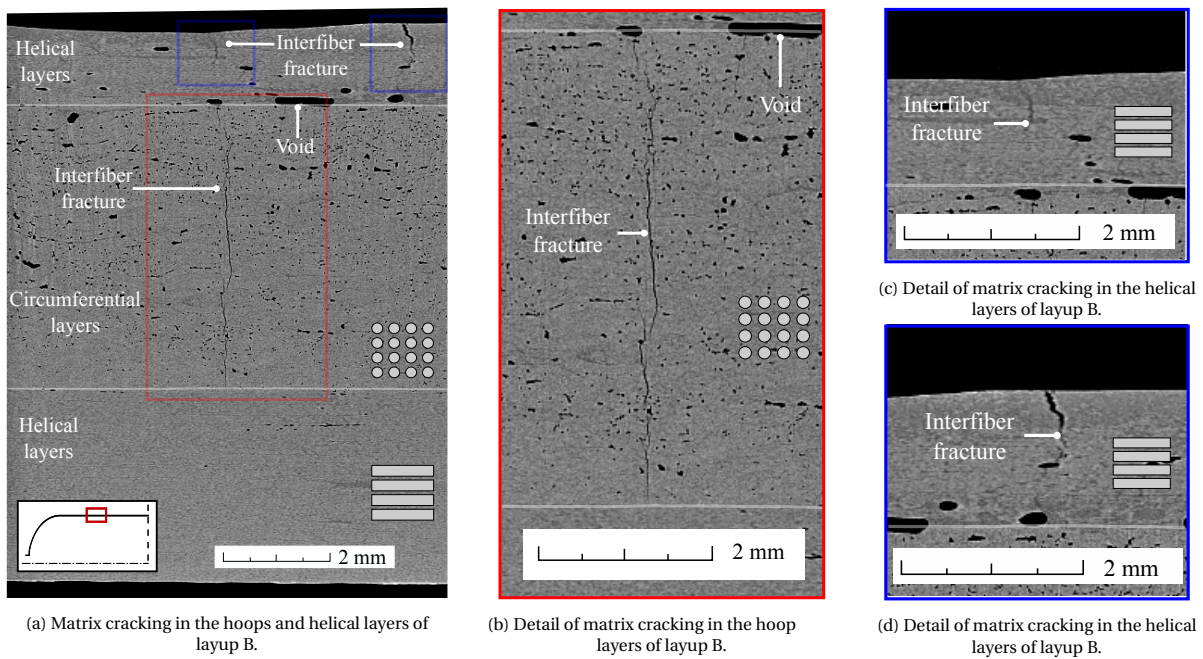


Figure 4.29: CT results of a specimen taken from a vessel with layup B after an EOL pressurization up to 105 MPa.

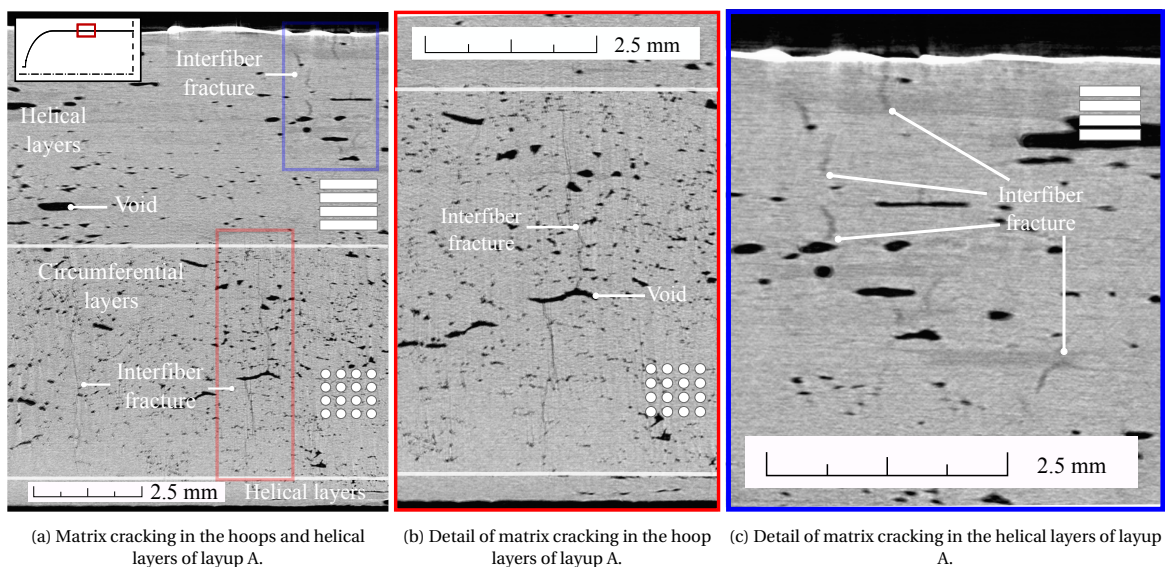


Figure 4.30: CT results of a specimen taken from a vessel with layup A after an EOL pressurization up to 75 MPa.

amount of black spots are present. It is very likely that these black spots are voids and it is evident that the crack passes through them. The voids could be the cause of the crack formation in that area because they act as stress concentrations [29]. It can be concluded that also for layup A, the emissions with higher sound pressure amplitude can be associated with IFF in the hoop layers.

Figure 4.30c shows the outer block of helicals, which, for this layup, it is made by 10 plies. Multiple cracks can be observed, in many of the top helicals, all characterized by small length. The change in orientation of the helical layers acts as crack stopper. The cracks located on the surface of the vessel can be associated to the black marks visible at the end of the pressurization due to the detachment of the chalk. In Paragraph 4.2.4 it was shown that the emissions were in larger number than the visible marks. This could be explained by the fact that some of the detected emissions correspond to the damage taking place in the helicals below the superficial, shown in Figure 4.30c.

4.3.3. Layup F

The last vessel scanned belongs to layup F, which has been pressurized up to 105 MPa. The results are shown in Figure 4.31 and belong to the same specimen (cut in a square of sides 10 mm by 10 mm) but at different widths and lengths.

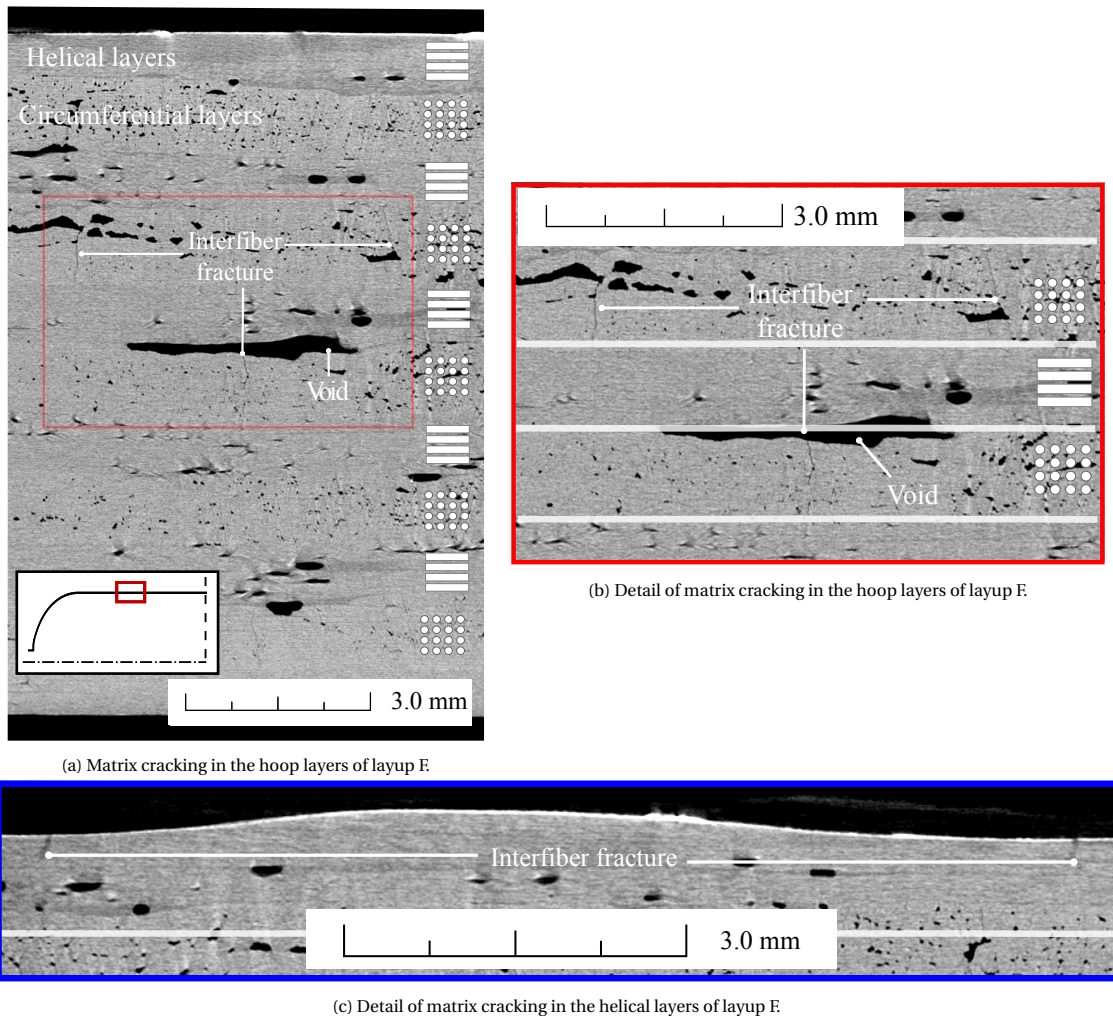


Figure 4.31: CT results of one specimen taken from a vessel of layup F after an EOL pressurization up to 105 MPa.

Figure 4.31a shows the entire thickness of the laminate, where the different blocks of hoops and helicals can be observed. The cracks formed in the hoop layers stop whenever there is a change in orientation, thus the fracture goes only through six circumferential plies. Figure 4.31b is a zoom of the red box of of Figure 4.31a in which it is possible to have a better visualization of IFFs. The cracks are formed where there is at least one void, which could act as stress concentration [29]. Looking at Figure 4.31a and considering only the blocks of hoop layers, it can be noticed that the porosity increases when going from the innermost to the outermost blocks. This is most likely caused by a compaction effect. Since tension is applied on the tows while winding, the deeper the layers are positioned in the laminate, the more they get compressed. This compacts the plies and lets the air trapped during winding out. This effect reduces the amount of voids in the inner layers and as it can be seen in Figure 4.31a also the possibility of creation of IFF. In fact, more cracks can be found in the outer blocks of hoops than the inner ones.

Figure 4.31c is taken from the same cut specimen but at different widths and lengths and shows the outer helical layers. As for the other layups, it is possible to notice the presence of matrix cracking in the superficial

helicals. This can be associated to the falling of the chalk.

With the information obtained analyzing this specimen it is not possible to conclude whether the acoustic emissions with higher amplitude in layup F can be associated to IFF in the hoops or in the outer helicals. This because in the specimen, both damage mechanisms are present. It can be speculated that the visible superficial matrix cracking might have taken place later in the pressurization and that the AE correspond to IFF in the hoops. This hypothesis could be reinforced observing that the emissions considered have a sound pressure amplitude above 1 Pa, while those in the later pressure stages (and usually associated with superficial cracking) have it below 0.5 Pa. On the other hand, it could be speculated that the damage corresponds to matrix cracking in the superficial helicals because in that zones it is possible to detect some fallen chalk. A possible solution to understand which is the correct hypothesis could be to pressurize a vessel until, for example, 40 MPa. Considering the other layups, at this pressure stage IFF in the hoops has already taken place, while in the helicals not yet. At this stage, no emissions should have been detected yet. When cutting a specimen from a random position in the cylindrical section, if IFF in the hoop layers is detected, it might be that the fracture surface is so small that does not produce any detectable emission. For this reason, what is detected by the sensors could be associated to IFF in the superficial helicals. If IFF in the hoops is not found, it would still not be possible to correctly associate the AEs.

In this paragraph it has been inspected the kind of damage present in the cylindrical section of the vessels after a pressurization. Three different layups have been analyzed: B, A and F. In all of them IFF in the hoop layers has been identified. The cracks were damaging the entire block of hoops in which they have been formed and stopped only where a change in winding direction was present. All the cracks were passing through at least one void. It has been concluded that there is a link between porosity and cracks formation in the hoops. This leads to the decrease in amount of cracks in the blocks of hoops located deeper in the laminate. In the three layups analyzed it was also detected matrix cracking in the outermost helical layers. The cracks stopped wherever there was a change in orientation, thus in between a single helical. When analyzing layup A it was noticed that not only the outermost helical presented cracks, but also others belonging to the same block but not superficial. Regarding layup F, both IFF in the hoops and superficial helicals were present in the same specimen, thus it was not possible to associate the AE with one of the two damages.

4.4. Damage Detection using DIC

In the considered pressure ranges the two main damage mechanisms that take place are IFF in the hoop layers (earlier in the pressurization) and in the superficial helical layers (later). It is interesting to understand whether these damages can be identified in the different layups using the DIC analysis. The two information that can be compared are the axial displacement of the top bearing and the full-field strain measurements.

In Figure 4.32 it is possible to observe the axial displacement of the top bearing during the pressurization test. As explained in Paragraph 3.4.2, this is tracked thanks to the reference points that are glued on the top boss of the vessel before the test. This is the side clamped into the floating bearing, which is free to displace. In Figure 4.32a are shown layups D, B and F (which were pressurized up to 105 MPa), while in Figure 4.32b A (pressurized only up to 75 MPa). The first part of the curves is non-linear and has some peaks and plateaus. This can be linked to the non-linearities caused by the pump at the beginning of the pressurization. Afterwards, the pressure rate is reached by the pump and kept constant and the internal pressure increases. This can be seen in the second part of the graphs, where the axial displacement increases. When reaching 105 MPa (or 75 MPa for layup A), the pressure rate drops to 0 and the maximum pressure is kept constant for few seconds. The pump valve is then opened and this causes the rapid depressurization of the vessel, which corresponds to a fast decrease in axial displacement. At the end of the test, the internal pressure of the vessel is 0 MPa, but a residual axial displacement is left. The displacements are summarized in Table 4.7. The row containing the information regarding layup A is gray because this layup is pressurized up to a different pressure stage and the data cannot be directly compared. This residual displacement can be related to the formation of damage in the vessel, in particular to IFF in the hoop layers. It is calculated in the axial direction and could be connected to the cracks formed in the 90° plies. After the depressurization, the cracks might not close perfectly and a small gap between the sides might be left. Summing up the gaps of all the formed IFFs could lead to a measurable displacement. This hypothesis is further reinforced when analyzing N_{hits} , which corresponds to

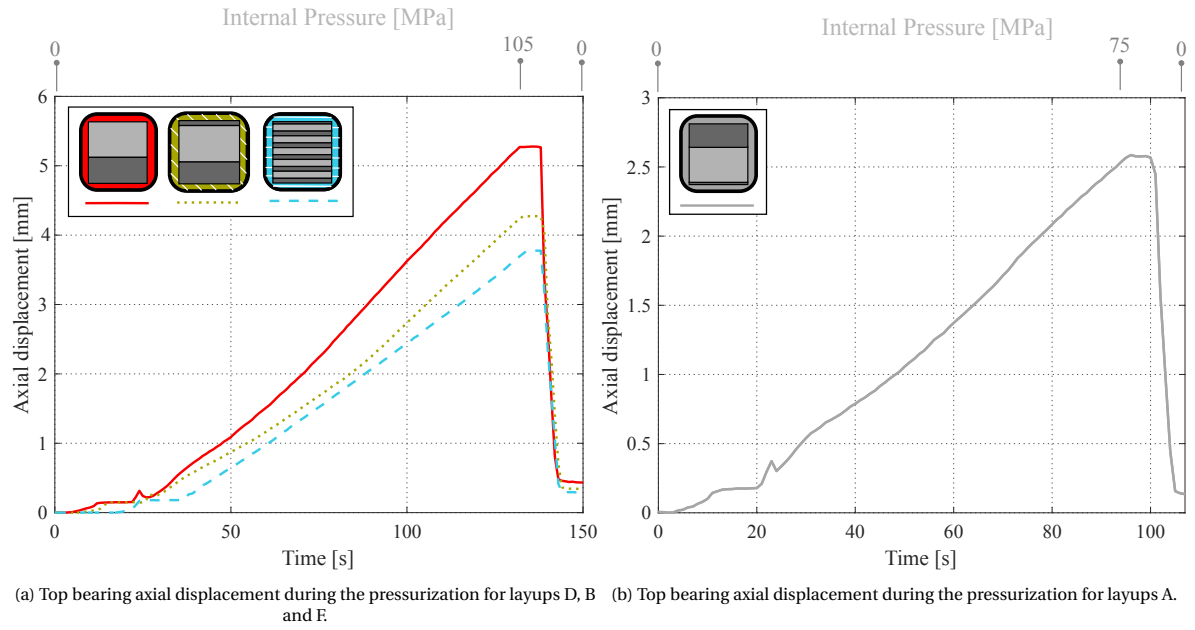


Figure 4.32: Axial displacement of the top bearing during pressurization test.

Table 4.7: Maximum and residual axial displacement of the top bearing during a pressurization test.

Layup	Maximum axial displacement [mm]	Residual axial displacement [mm]	N_{hits} [-]
D	5.28	0.441	72
B	4.28	0.340	48 ± 4
F	3.78	0.301	1 ± 0
A	2.59	0.135	17 ± 7

the peaks detected with a sound pressure amplitude above 2 Pa. These emissions are associated with IFF in the hoops. It can be noticed that (except layup A) the more cracks in the hoops are detected and the higher is the residual axial displacement.

Another aspect that could be interesting to analyze is the full-field strain. This is represented as a pictorial map that shows the strain state of the entire surface. In the next figures, the meridional superficial strains for each layup are shown. They are taken at two pressure stages: the first one corresponds to the vessels right after the higher amplitude AE are recorded (after IFF in the hoops has occurred) and the second one at 75 MPa for layup A and 105 MPa for all the others. In Figure 4.33 is represented the vessel with layup D. For this case, the first Figure (4.33a) shows the vessel before the pressurization. This stage is the reference and the measured strain is 0% everywhere on the surface. This is the same for all the layups, thus the full-field strain of the unpressurized vessel is shown only once. In Figure 4.33b it is represented the vessel after IFF in the hoops has taken place. Lines of different colors are visible where IFF is formed. It can be concluded that it is possible to detect IFF in the hoops layer when they are the outermost plies. This is in agreement with the research of Oz et al. [55], which has the same outcome but at laminate level. It must be taken into account that, when IFF is formed the color depicted on the surface does not represent the real strain. The two sides of the crack get separated and a small discontinuity in the speckle pattern is created. This is not accounted for in the DIC software, as shown in Figure 4.33d. The software will recognize it as strain and will color it consequently. This effect is also seen in Figure 4.33c, which shows the vessel at 105 MPa. Due to the pressure increase, the vessel axially displaces and the sides of each crack get further separated. The software will represent the areas as if they were highly strained, while a further separation between the two sides is taking place.

As explained in Paragraph 4.2.2, matrix cracking in the superficial helical is present in the domes for layup D at the end of the pressurization. Looking at Figure 4.33c it is possible to notice that the interested area is sub-

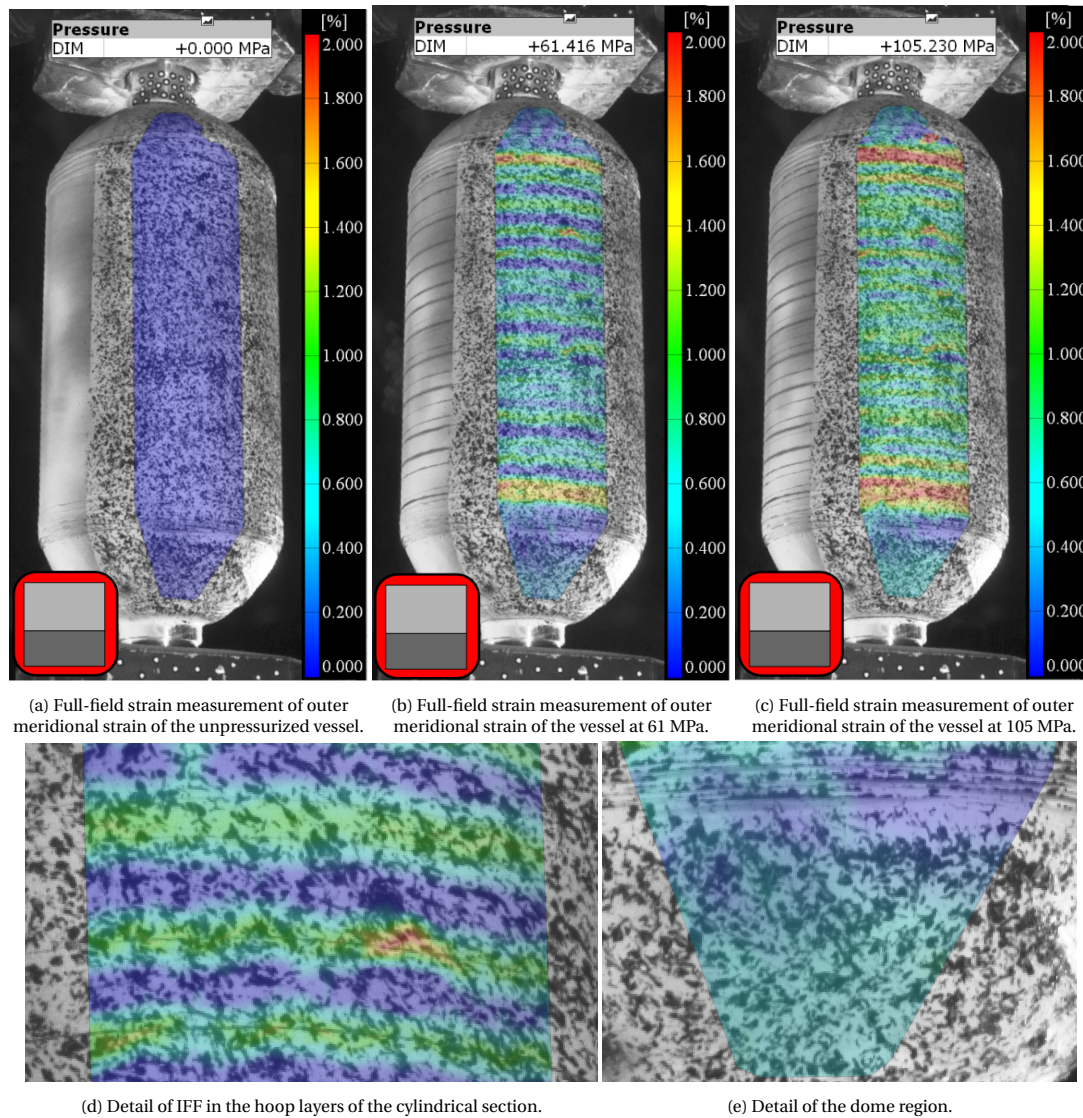


Figure 4.33: Full-field strain measurement of outer meridional strain of layout D at different pressure stages.

jected to a higher strain with respect to Figure 4.33b. Looking at the zoom of the area, represented in Figure 4.33e, it is not possible to detect the superficial crack, as it was with visual inspection. This could be caused by the optic system resolution and the small fracture surface created compared to the significant measuring volume. It can be concluded that for layout D it is possible to detect IFF the hoops layers using DIC, but not matrix cracking in the helicals visible in the domes.

To prove whether IFF is always detectable using DIC, it is necessary to investigate the layouts which do not have the hoops as outermost layers. Figure 4.34 shows the full-field meridional strain of the other layouts, taken at a pressure stage matching with the end of IFF in the hoops formation. For all the cases the overall strain is higher than zero and each vessel presents a specific strain distribution. Layouts B and C are characterized by higher strain in the cylindrical section, while A and F in the transition zone. No layout shows any significant higher strains stripes in the cylindrical section that can be linked to IFF. It can be concluded that IFF in the hoops is not detectable for all the layouts using DIC.

Figure 4.35 represents layouts B, C, A and F at the maximum internal pressure (75 MPa for A and 105 MPa for the others). As previously discussed for layout D, there is no possibility to detect the formation or to visualize matrix cracking taking place in the superficial helical layer with the DIC. For the identification of this type of damage, the best solution is using visual inspection combined with chalk powder. Information regarding the

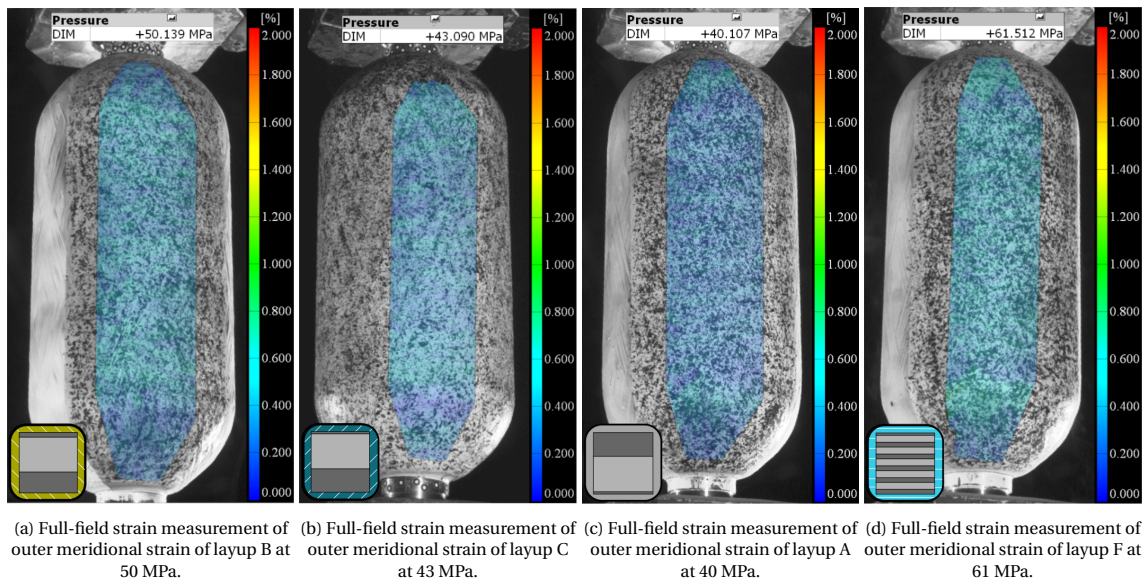


Figure 4.34: Full-field strain measurement of outer meridional strain of layups B, C, A and F respectively after IFF formation.

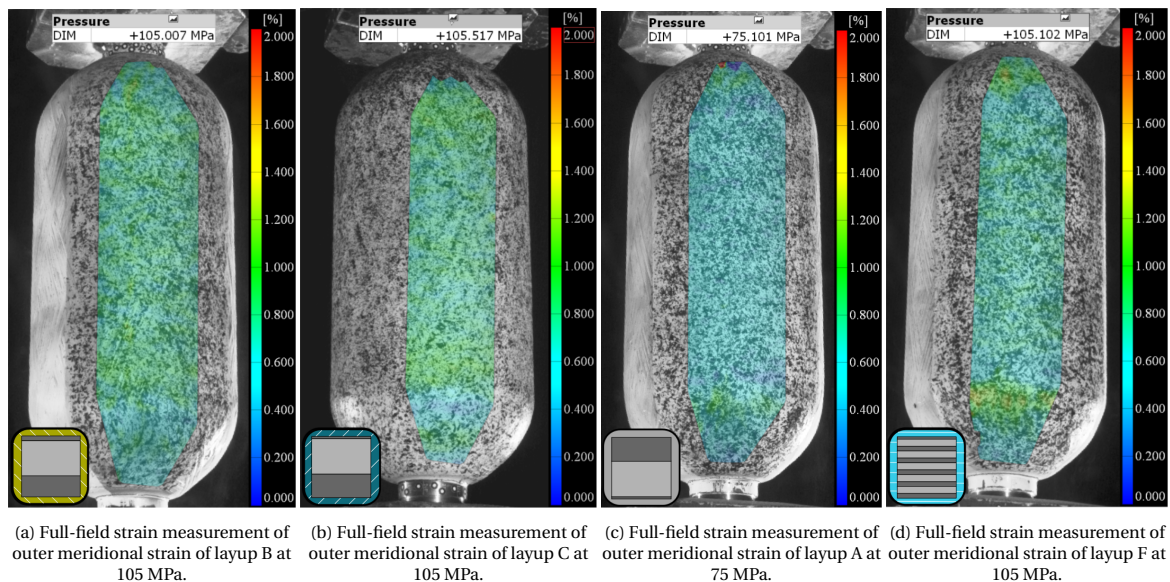


Figure 4.35: Full-field strain measurement of outer meridional strain of layups B, C, A and F at the maximum internal pressure.

superficial strains could be linked to the progression of matrix cracking in the top helicals. For layup B this type of damage was first detected in the cylindrical section and later in the transition zones and domes, as it was shown in Figure 4.22. This result is consistent with the strain distribution, being higher in the cylinder (Figure 4.35a). The opposite reasoning can be applied to layup F. The superficial marks are first appearing in the transition zones and later in the cylindrical section (Figure 4.28) in accordance to the location of the AEs. This is also in agreement with the superficial full-field meridional strains, shown in Figure 4.35d: the strain is higher in the transition zones. Considering layup A it is not easy to draw the same conclusions. Even if some low amplitude emissions have been localized in the domes and transition zones, they were not visible on the surface, as explained in Paragraph 4.2.4. It was concluded that the stress distributions could have played a role causing damage in the innermost helicals before the outermost ones. A research taking place simultaneously to the current investigation was studying the vessels from the analytical and optical point of view. It was observed that the strains in the transition zones were approximately constant all around the vessels for each configuration. This was not the case for layup A. When progressing with the pressurization, the transition zones presented few spots with significantly higher strains. An example is shown in Figure 4.36. The internal

pressure is about 98 MPa and in the transition zone the red spot reaches a strain of 1.856 % while in the rest of the transition zone, it is about 0.9 - 1.1 %. In these areas, delaminations between the hoops and the helicals

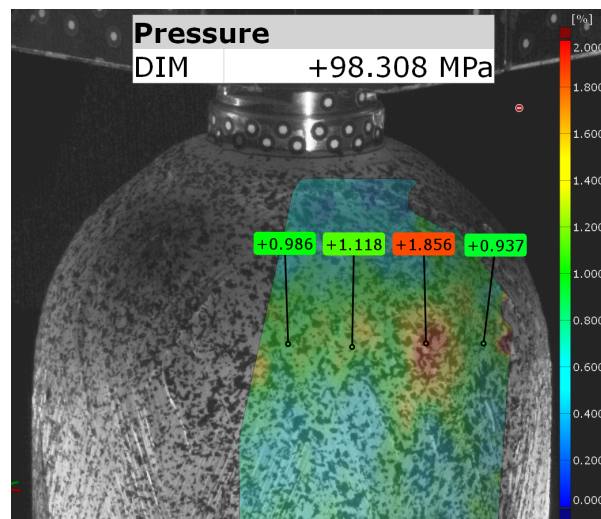


Figure 4.36: High strain spot in the transition zone of layup A.

have been detected after CT analysis. This is in agreement with what found by Szebényi and Hliva [83]. In their studies, they recreated delaminations adding some foils in the layup. They showed that where the foils had been added, the DIC was detecting a local higher strain. The fact that the higher strains are caused by the formation of another damage mechanism might be the reason why no superficial damage is seen. From literature (Figure 2.17) it was shown that delaminations are usually associated to emissions with an amplitude in between that of IFF and fiber failure. In the current case, the emissions taking place in the domes at the later stages present low amplitudes. More research on the topic is needed to have a definitive explanation of the events.

In conclusion it can be observed that DIC is able to clearly detect IFF in the hoops layers only if those are superficial and not covered by any other layer. This confirms what found at laminate level [55]. The residual axial displacement of the top bearing can be used as an indication of IFF occurrence in the hoops after the depressurization. IFF in the superficial helicals cannot be detected with DIC. Chalk powder and visual inspection are more suitable for the purpose. The superficial strains can be used to predict which areas will be affected by cracking in the outer helicals first. This is not the case when analyzing layup A. This vessel presented small spots of higher strain in the transition zone, which was not in agreement with the detected emissions distribution. It is supposed that those higher spots correspond to delaminations, as reported in literature [83] and in other studies performed in the department. If this was the case, it would not be in agreement with the literature regarding the AEs amplitude related to delaminations. They are usually associated with emissions of medium amplitude, while for the current case only low amplitude emissions are detected in the area. It is most likely the case that at these pressure stages the delamination is just started and does not cause an important energy release. Further research on the topic is needed in order to clarify the subject.

4.5. Positioning and Grouping Effect

In this paragraph will be summarized how the stacking sequence influences the acoustics behavior of a pressure vessel subjected to a pressurization test. The results described in the chapter will be further analyzed and compared to other layups previously tested in the department, presented in Paragraph 3.1.3. A representation of the totality of the analyzed stacking sequences is reported for simplicity in Figure 4.37. Each background color and pattern are representative of a stacking sequence and the same color code will be used for the data representation in the paragraph. Regarding the layups themselves, the dark gray represents the helical layers, while the lighter one the hoops. Layups E and B* (respectively Figures 4.37e and 4.37g) are not part of the current investigation but their characteristics are known from previous studies. Layup B* is exactly as layup B, but with seven hoop layers removed, thus with a total of 23 circumferentials. Layup E has the same amount of plies as the majority of the other layups (52 in total). Its hoop layers are divided into two

identical groups separated by helicals as shown in Figure 4.37e.

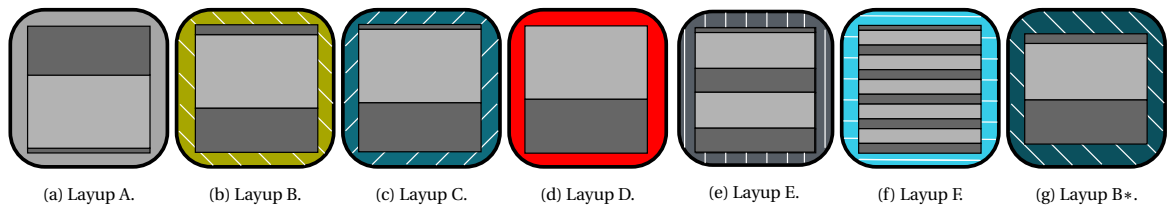


Figure 4.37: Pictorial representation of the seven layups of the investigation.

The goal is to find relationships between the different stacking sequences and the acoustic variables previously described. The variables are those presented in Paragraph 4.1 and are calculated using threshold I, thus considering only emissions with a sound pressure amplitude above 2 Pa. The focus will be on the link between the effect of grouping and positioning of the hoop layers in the laminate with respect to the acoustic emissions produced. This information could be beneficial whenever a new vessel with unknown layup will be tested in the department. The stacking sequence could be understood up to a certain level thanks to the found relationships.

4.5.1. Positioning

The first aspect analyzed is the effect of the positioning of the block of hoop layers. The layups studied are D, C, B and A which have the same amount of layers and a single block of 30 hoops, positioned at different depths in the laminate. They have respectively zero, one, two and 10 helical layers above the block of circumferentials. Figure 4.38 shows how the maximum sound pressure amplitude (A_{max}) and the pressure at which the first emission is detected ($P_{AE,start}$) are influenced by the positioning of the block of hoops. In each graph, the average values are shown, as well as the standard deviations.

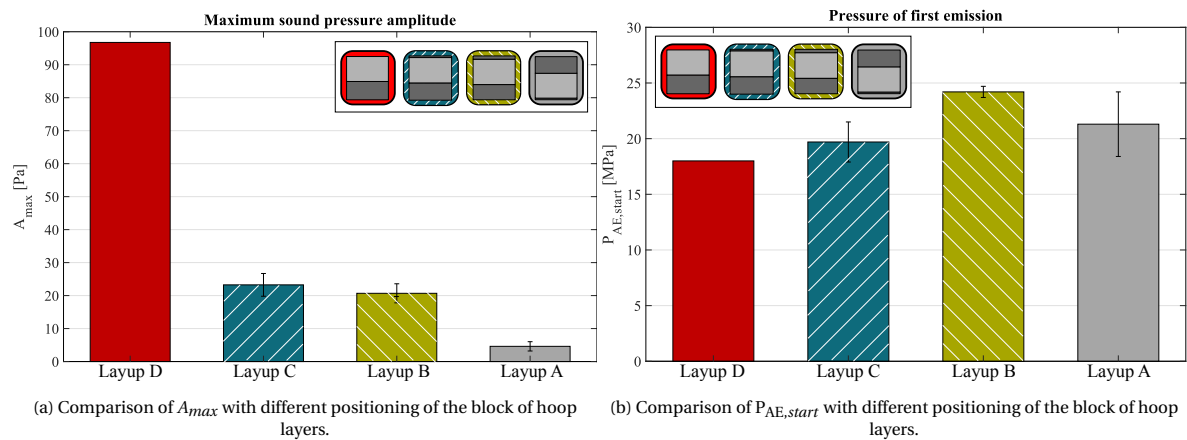


Figure 4.38: Comparison of A_{max} and $P_{AE,start}$ with different positioning of the block of hoop layers.

Looking at Figure 4.38a, it can be noticed that the maximum amplitude recorded is highly influenced by the location of the hoops. The more helical layers are positioned on top of the hoops, the lower is the maximum sound pressure amplitude recorded. This is in agreement with what found in literature at laminate level [30, 55]. It can be observed that there is a drop when passing from zero to one outer helical layer. This significant trend is not followed when moving another helical from the inside to the outside. In the latter case there is just a small decrease. A further drop in maximum amplitude is encountered when moving all the helicals except one. What causes such a high maximum amplitude for layup D are two effects, already presented in Paragraph 4.2.3. The first one is the attenuation caused by the presence of some layers wound above the crack. If this would be the only cause, a similar significantly high effect should be observed whenever adding another single layer. The main cause could be related to the possibility of the two sides of the crack to separate without restriction and to release an appreciable amount of energy. This is known as the free boundary

effect [28]. For all the other layups, the top helicals keep the sides of the cracks together, reducing the amount of energy released and the work done for the crack opening.

In Figure 4.38b it can be noticed that the hydraulic pressure at which the first emission takes place is slightly influenced by the positioning of the hoops. Considering D, C and B it can be observed that the more helicals are added on top of the block of hoops, the later the first emission is recorded. This could be explained by the fact that the top helical layers hold the hoops together and delay the cracks formation. If this was the only cause, $P_{AE,start}$ of layup A should be the highest, which is not the case. It must be considered that while layups D, C and B are similar in terms of stacking sequence: inner block of helicals, block of hoops and few or no helicals on top, layup A is significantly different, being the opposite of C. This must cause a completely different stress distribution through the thickness of the laminate that could be the reason why the trend is not followed. Due to the thick wall, the tangential stresses are higher in the inside of the vessel with respect to the surface. Since in layup A the hoops are positioned deeper in the laminate, they could crack earlier than the other configurations. Another variable that has been proven to influence the IFF formation is the presence of voids, as explained in Paragraph 4.3. In the department, some colleagues have investigated the porosity of the different layups. It was concluded that layups B and A have in the block of hoops in the cylindrical section a very similar void content percentage (respectively 2.19% and 2.03%). For this reason, the porosity should not play an important role in the formation of IFF in the hoops.

4.5.2. Grouping

The next aspects analyzed are the effects of the grouping of the hoop layers. In particular, two scenarios are evaluated. The first one is represented in Figure 4.39 and it studies how A_{max} and $P_{AE,start}$ are affected when comparing two vessels in which the only difference is in the number of hoop layers. Layups B and B* are exactly the same except that B has 30 hoops while B* only 23. The second case will evaluate the differences when comparing vessels with the same amount of hoops and helicals but having them split in multiple smaller blocks.

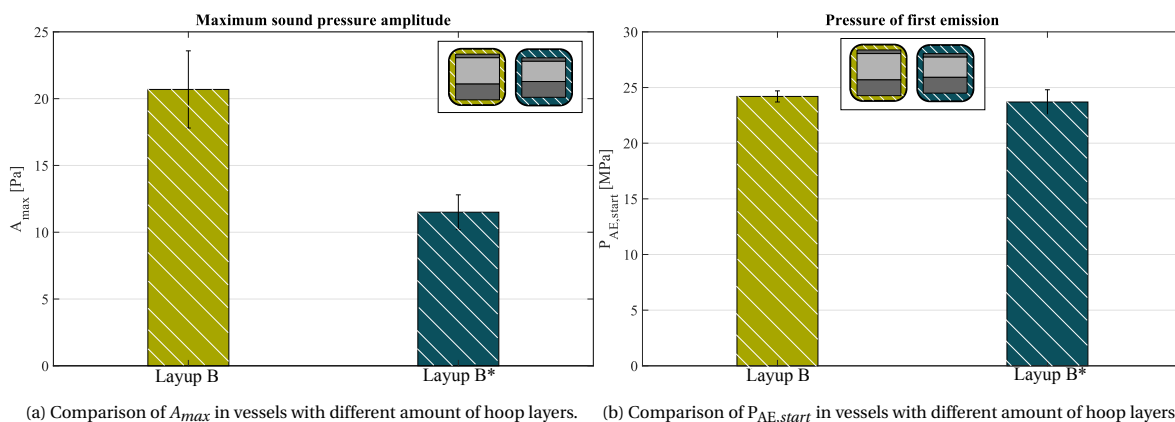


Figure 4.39: Comparison of A_{max} and $P_{AE,start}$ in vessels with different amount of hoop layers.

In Figure 4.39a it can be noticed that there is a difference in maximum sound pressure amplitude when changing the amount of stacked hoop layers. The less circumferential plies are stacked together, the lower is the amplitude of the AEs caused by IFF. More in detail, removing the 23% of hoops reduces the maximum sound pressure amplitude recorded of 44.4%. This fact can be linked to the length of the fracture surface created [30, 42, 68]. The shorter it is, the lower is the energy released.

Looking at Figure 4.39b, which shows the pressure at which the first emission is detected, it can be noticed that there is hardly a difference between the two layups. It could be concluded that the amount of hoop layers in the laminate (keeping the same positioning) does not influence the crack formation. This can be further proved comparing the amount of emissions detected (N_{hits}) in the two layups. This has already been investigated in the department in previous studies and it has been found that the emissions identified for layups B and B* are respectively (on average) 48 and 49 [42]. It could be concluded that the ratio between the num-

ber of circumferentials and helicals in a laminate does not have a significant difference in the formation of IFF in the hoops, up to a certain extent. This could also explain why $P_{AE,start}$ and N_{hits} have hardly differences.

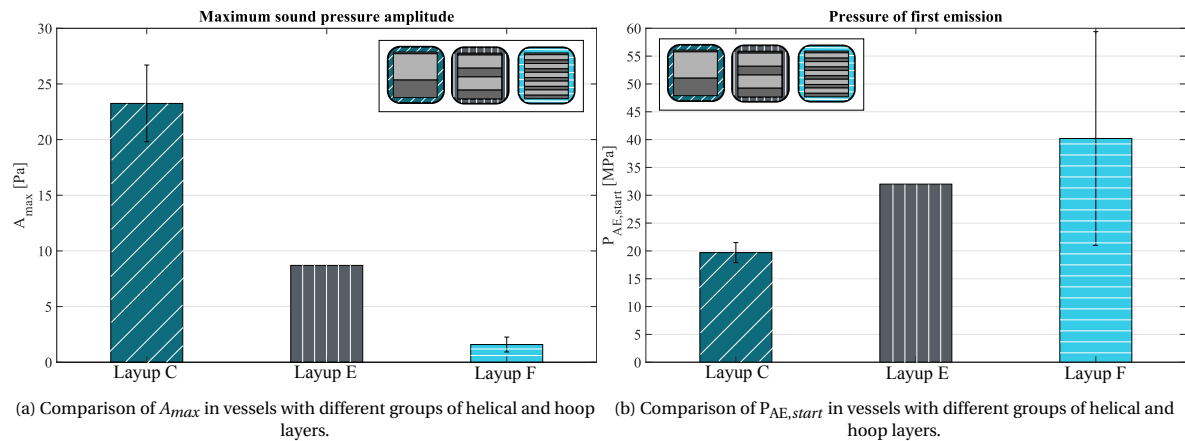


Figure 4.40: Comparison of A_{max} and $P_{AE,start}$ in vessels with different groups of helical and hoop layers.

The last comparison regards the different grouping of hoops and helicals. For the three considered vessels the ratio between them is the same as well as the amount of layers. The difference consists in the number of blocks of hoops created. In particular, layup C has only one group of 30 hoops, E has two of 15 and F has six blocks of five layers each. All the vessels have a single helical as outermost layer. Only one vessel of layup E has been tested, thus more specimens would be needed before drawing the final conclusions. However, since all the vessels of one layup follow a clear pattern regarding their acoustic behavior, it has been decided to insert it in the research. Regarding layup E, it must be taken into account that of the eight vessels analyzed, only three produced AEs with a sound pressure amplitude above 2 Pa. Furthermore, for all of them only a single hit has been detected and at different internal pressure. This factor might be a limit when analyzing $P_{AE,start}$ of this layup. It is also not possible to clarify whether the first detected emission in layup F corresponds to IFF taking place in the hoops or in the superficial helicals.

In Figure 4.40a it can be noticed that the maximum sound pressure amplitude recorded is affected by the grouping. The same trend observed before is repeated: the less hoops are stacked in a block and the lower is the AE amplitude. When halving the amount of hoops in a block, the sound pressure amplitude drops of 62.6%. As for the previous case and similarly to what found in literature, this effect can be related to the size of the fracture surface and the energy release associated to it [30, 42, 68]. For layup F it is not clear whether the emission with maximum sound pressure amplitude corresponds to IFF in the hoops or in the outermost helical layer, as already explained in Paragraph 4.3.3. The data provided can be used to give a qualitative overview on how the grouping of the hoop layers affects the acoustics but not quantitative results.

In Figure 4.40b it is represented the pressure stage at which the first emission is detected. The standard deviation for layup F is significantly high. This is the case because for only three of the eight investigated vessels it was possible to detect AEs with the given threshold and for each only a single peak was identified. Furthermore, for one of the three vessels the hydraulic pressure was not recorded, reducing the comparison to only two. For all the other vessels, the amplitude of the acoustic emissions produced was below 2 Pa. Again, it must be taken into account that for layup F it is not clear whether these detected emissions correspond to IFF located in the hoop or helical layers. Looking at the values given in Figure 4.40b it can be noticed that there is a significant difference between the layups. The more the groups, the higher is the hydraulic pressure at which the first emission is detected. One hypothesis that has been speculated is that the first emission recorded does not correspond to the first IFF in the hoops created in the laminate. Considering layup E it could be the case that the emissions detected are most likely produced by IFF present in the outermost blocks of hoops. As already shown in Paragraph 4.5.1, the deeper in the laminate the crack is formed, the lower is the sound pressure amplitude produced. Since the amplitude is also depending on the amount of hoops stacked, it is most likely the case that the cracks formed in the innermost block cannot be detected by the system. It might be speculated that the innermost blocks of hoops crack earlier than the outermost. Due to the small fracture

surface and the depth in the laminate, they produce a sound pressure amplitude that cannot be detected by the current system. For this reason, the first emission detected corresponds to IFF in the outermost block of hoops.

One study that is currently taking place in the department concerns the simulation of the layups. Even if this topic is not part of the current research, few results will be presented to verify whether the hypothesis can be validated. In the department, layup F has been simulated. Figure 4.41 shows the transverse failure index for each couple of hoop layers. The data are taken at a simulated hydraulic pressure of 35 MPa and at the axial symmetry plane of the vessel, so at half of the total length. This simulation is performed using a continuum shell formulation in the software Abaqus. Each vertical bar corresponds to a couple of hoop layers, thus each

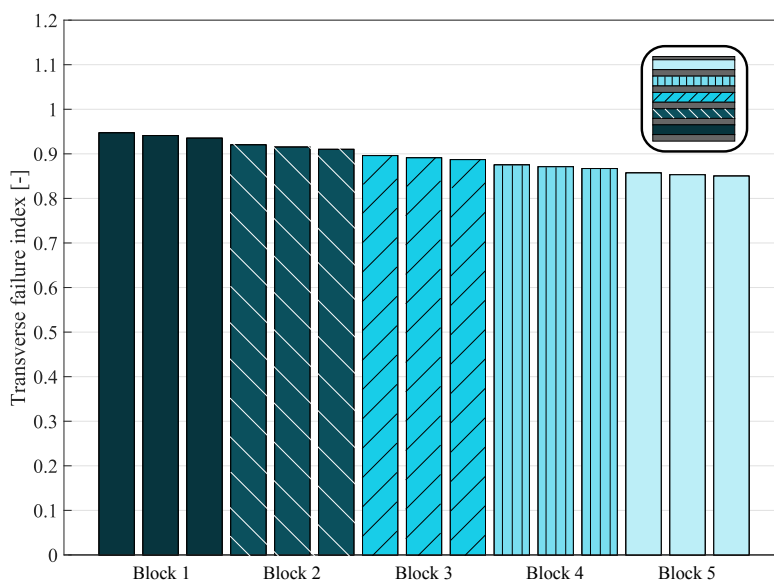


Figure 4.41: Transverse failure index simulated for each couple of hoops of layup F with continuum shell approach.

block of hoops in the laminate is represented with three bars of the same color and pattern. As shown in the pictorial representation of the layup, block 1 corresponds to the innermost block of hoops while block 5 to the outermost. The helical layers are not represented. When the transverse failure index is equal to one, it means that the couple of hoops has failed, thus that matrix cracking has taken place. Comparing the indices it can be noticed that it is higher for the innermost plies and it decreases when moving outwards. This means that, according to this formulation, IFF will take place in the deeper blocks first and the superficial one last. This finding reinforces the hypothesis. In more recent times, the vessel has been simulated using a solid element formulation instead of the continuum shell approach. This new formulation is more effective when modeling thick structures such as the CPVs of the current investigation. The results of this method are shown in Figure 4.42. Also in this case, these data correspond to a simulated internal pressure of 35 MPa and the representation is the same of the case above. The trend is exactly the opposite which makes the results in conflict with the previous findings. These data show that the hoop layers that will fail first are the most external ones, which is in disagreement with the previously mentioned hypothesis. However, this method is the one giving most realistic data for thick structures. It can be concluded that it is most likely the case that the hypothesis is incorrect and that the delay in the recording of the first emission must be associated to other effects.

One effect that could play a role in the delay of the detection of the first emission in the hoop layers could be the *in situ* strength as described by Kassapoglou [31]. This refers to “the varying strength of a ply perpendicular to the fibers” [31]. It has been studied that when the thickness of these plies increases, the *in situ* strength decreases. This could explain why IFF in the hoops is detected at earlier pressure stages in C when compared to E. This could also explain why all the layups with a single block of 30 hoops (D, C, B and A) have similar values of $P_{AE, start}$, as shown in Figure 4.38b. If this effect was playing such an important role, it should have also been noticed in the comparison of layups B and B*. This was not the case, thus it only plays a marginal role.

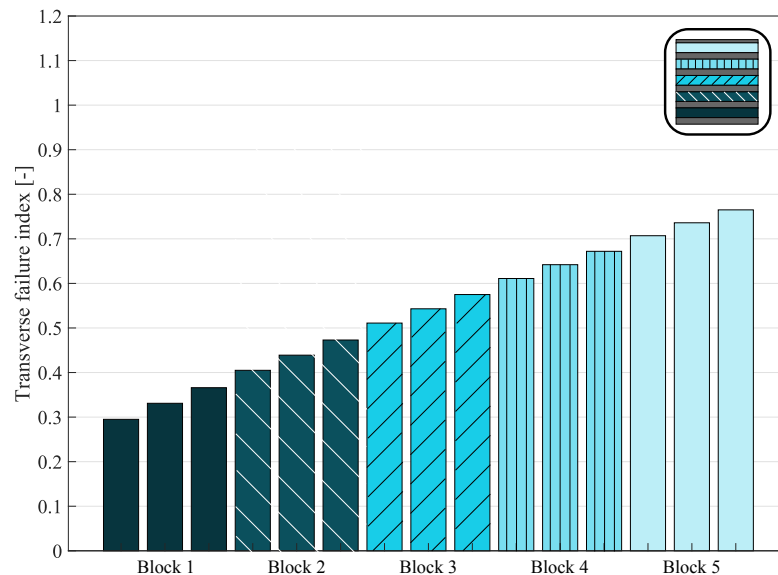


Figure 4.42: Transverse failure index simulated for each couple of hoops of layup F with solid elements.

Another effect that could play a side role is the porosity. Since voids could act as stress concentrations which cause cracks formation [29], a low porosity could link to a lower possibility of matrix cracking. When comparing the void content of layup B and F in the cylindrical section, they have significantly different values. For layup B it is 1.76%, while for F only 0.88%. However, it must be considered that the void content is calculated through chemical digestion. This means that the stated values also consider the superficial resin layer, thus could be distorted and not provide the effective void content. The effect of the porosity could be proven calculating the void content of the layups using, for example, CT scans.

It can be concluded that using the acoustic analysis on a CPV, it is possible to understand some characteristics of the layup if this is unknown. After the pressurization, the acoustic data must be post-processed with the existing tools, in particular having the `PeakFinder` set with threshold I. The first emission must be detected and its corresponding hydraulic pressure is taken. This value gives information regarding the layers grouping. If the first emission happens in an early pressure range, the hoops are most likely all stacked in a single block. The later during the pressurization the first emission is detected, the more blocks are the hoops divided in. This case is further characterized by a lowering of the maximum amplitude recorded. The pressure of the first emission does not give any information regarding the amount of hoops (as shown comparing layups B and B*) neither their positioning (A, B, C, D). These two characteristics can be understood checking the maximum sound pressure amplitude recorded during the test. If this value is high, it means that the block of circumferentials is not positioned in depth in the laminate and that the hoops are in high number. If this is low it means that either the block has a lower amount of hoops or that it is positioned more in depth in the laminate.

It must be pointed out that this study is limited to layups having the hoops wound at an angle of $+88.5^\circ$ and -88.5° and the helicals at $\pm 19.9^\circ$. In order to have accurate results it is more beneficial to compare the acquired data with already existing data of known layups.

4.6. Final Discussion

When internally pressurized during an EOL test, the CPVs examined in the current investigation are characterized by the formation of one damage mechanism: matrix cracking. An example can be seen in Figure 4.43a. In filament wound vessels, there is a difference in the characteristics of this damage according to the layer type in which it takes place. When a crack is formed in the helical layers, it tends to propagate in-plane and it gets stopped whenever the tow intersects another one. An example can be observed in Figure 4.43c. Since these layers are cross-ply, the tows intersect very often and for this reason the fracture created has limited length. This also reduces the possibility of the crack to propagate through the thickness of the lam-

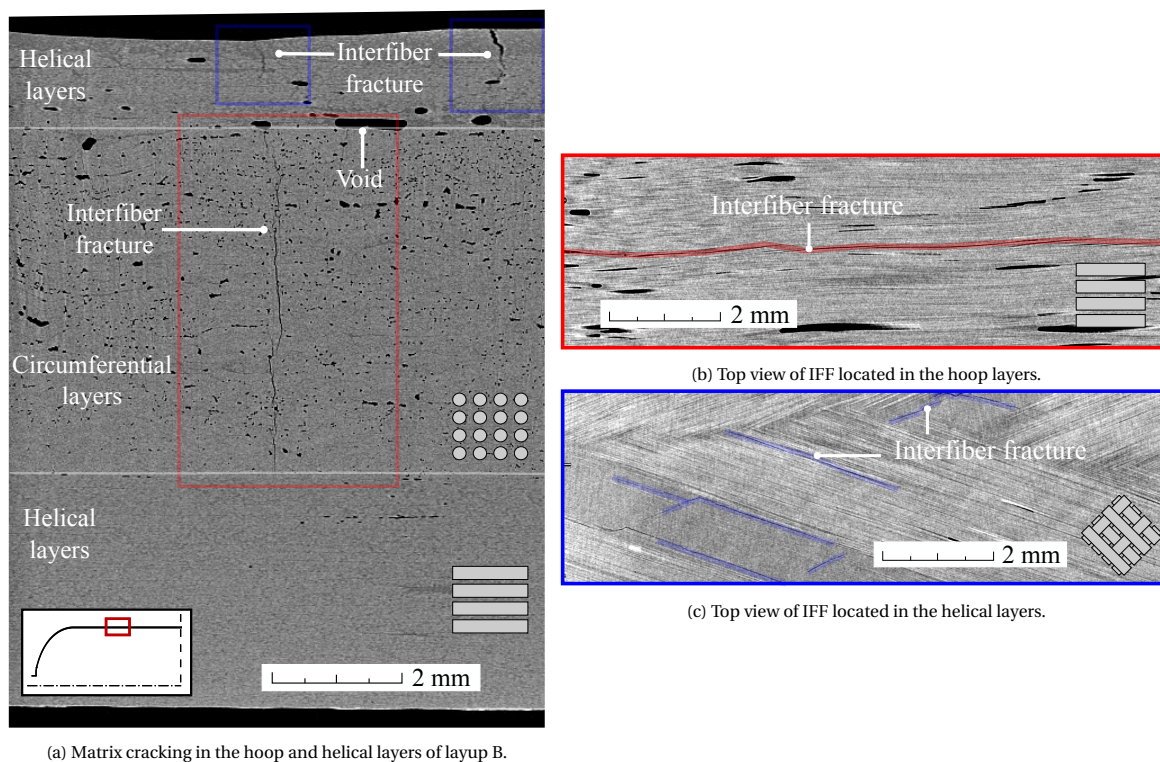


Figure 4.43: CT results of a specimen after an EOL pressurization up to 105 MPa.

inate, because the different orientations act as crack stoppers. Due to the limited fracture surface created, the acoustic emissions associated to this kind of damage are characterized by small amplitudes. When this damage takes place in the most superficial helical layer, it can be visually detected as a black mark if a layer of chalk powder is applied on the surface. However, it cannot be detected on a speckled surface using DIC. This could be caused by the resolution of the current system if compared to the small size of the crack. DIC is suitable to identify in which areas of the vessel it will first take place. It was shown that IFF in the superficial layer was found first in the areas where a higher superficial strain was calculated. Continuing the pressurization will lead to an increase of the strains and possible IFF formation also in areas where the calculated strains are lower. This damage takes place in the superficial layers when the pressurization is at about the middle stages, thus when some differences in superficial strain can be detected. This damage produces AEs with amplitudes usually below 2 Pa. These emissions can be detected with the systems used in the project for all the layups except for F. For this stacking sequence, the majority of the events are below the minimum set threshold and not detectable with the current systems. This is evident because at the end of the pressurization black marks are visible on the vessel surface but only a limited amount of emissions is identified. It is not clear why this layup has this characteristic. The hypothesis that it could be related to the lower superficial strain of this layup is not proven because this value is comparable with those of the other layups. The opposite trend is observed when considering A. More emissions than visible marks are detected when analyzing this configuration. The presence of multiple helicals as outermost layers in comparison to the other analyzed layups might be the cause. This led to the hypothesis that the emissions detected could be related to cracks taking place not only in the top helical, but also in the layers underneath. The CT scans confirmed the hypothesis, since cracks in multiple helicals have been detected. Another factor that could play a role is the absence of a resin layer on the surface of the vessel. This layer is present (with different thicknesses) in all the other layups. It is caused by the compaction effect that the hoop layers act on the inner helicals. This compaction compresses the inner helicals and reduces their porosity. As a consequence, the resin that is taken from the helicals flows towards the outside of the vessel during curing and gets distributed on the surface. Since for layup A the main block of helicals is located above the hoop layers, this compaction is absent and, as a consequence, also a top resin layer. This effect could contribute to explain the limited amount of visible marks.

Different considerations can be done when considering IFF that takes place in the hoop layers. The cracks

propagate both in-plane and through the thickness, as visible in Figures 4.43a and 4.43b. When they are formed, they quickly progress in-plane forming a complete ring around the vessel. This was evident observing layup D in which the hoops layers are the most external ones. This fact was also confirmed when analyzing the acoustic signal that this damage was creating. It was discovered that the microphones recording the maximum sound pressure amplitude of the emissions associated to this damage are positioned in different walls all around the testing chamber. The crack also grows through the thickness of the laminate. Since the hoops are wound with the same orientation, IFF can easily progress until where it encounters a helical ply, which acts as crack stopper [31]. This can be observed in Figure 4.43a. From the scans it is also possible to notice that the IFF located in the hoop layers is passing through at least one void in the majority of the cases. This could confirm what found in literature which states that the voids in a laminate could act stresses concentration that may cause the cracks formation [29]. Looking at layup E, it was possible to notice that the majority of the cracks in the hoop layers were located on the outer-most blocks. Due to compaction, the blocks positioned more internally in the layup presented a lower porosity and also less cracks. IFF in the hoop layers could be detected by the DIC analysis only in layup D in which the circumferential are the most external ones. This is the opposite of what stated above when considering IFF taking place in the helicals. This difference could be associated to the significant size of the fracture when compared to the measuring volume. Nevertheless, IFF in the hoops is not detected by the DIC when they are located below one or multiple helicals [55]. After the vessel depressurization, it is possible to understand whether IFF in the hoops has taken place, studying the residual axial displacement of the top boss thanks to DIC. After the vessel depressurization, a residual displacement can be measured. This can be linked to the closure of the cracks. After the depressurization the cracks might not close perfectly, leaving a small gap between the two sides. Summing all the gaps can lead to a measurable displacement. Acoustic emission analysis can provide more precise results. IFF that takes place in the hoops produces emissions which are usually characterized by higher amplitudes when compared to those located in the helicals. This is explained by the bigger size of the fracture surface which is associated to a higher energy release. Since the in-plane fracture size is comparable for all the layups (it forms a ring around the vessel), what causes differences is its progression through the thickness. It depends on both the amount of hoop layers stacked together and their position through the laminate. It was proven that vessels with more hoops stacked together produced emissions of higher amplitude when compared to those with less (e.g. layups B and B*). This confirms what studied at laminate level [30, 68] and what supposed by Torres Guijarro in the analysis of CPVs [42]. The AE sound pressure amplitude is also influenced by the position of the IFF through the laminate thickness: the deeper it takes place and the lower it will be due to attenuation. Also this fact proves what already discovered at laminate level [30, 55].

Another aspect that has been analyzed is the internal pressure at which the first emission is detected. This considers the emissions with a sound pressure amplitude above 2 Pa, according to the predefined thresholds (Threshold I). Figure 4.44 shows how this parameter and the maximum recorded amplitude vary according to the analyzed stacking sequences. Each mark corresponds to a specimen and those of the same color belong to the same stacking sequence. To make the understanding easier, the results of each layup are grouped in circles with shaded areas. It can be observed that the specimens of each stacking sequence are located in a specific area of the graph, which means that they all follow a pattern. This is true for all the layups except F. Its results are highly influenced by the threshold settings due to the low amplitude of the emissions that characterize this stacking sequence. The vertical axis of the graph represents A_{max} , while the horizontal $P_{AE,start}$. The majority of the layups are grouped in one area of the graph, except D which is positioned particularly far from the rest of the groups. It has a significantly higher maximum amplitude recorded. This is the case because it has the hoops in a single block and no helicals on top that can attenuate the acoustic wave. The free boundary effect also plays a role [28]. Layups B and C are similar with the difference that the latter has one helical moved towards the inside of the laminate. Their sound pressure amplitudes are similar (slightly higher for C), while the pressure of the first emission is not. This could be explained by the constraining effect of the top two helicals (layup B) that retard the crack formation when compared to C that has only one outer helical. Layup A is located at the bottom of the diagram, due to the deep position of the block of hoops that causes emissions of lower amplitudes. Layup B* is located just below B, in accordance to the consideration on the fracture surface size. Despite the seven less hoops, their $P_{AE,start}$ is similar. This shows that keeping the same stacking sequence but changing only the helicals to hoop ratio, the maximum sound pressure amplitude recorded is influenced but not the $P_{AE,start}$, at least for this case. Considering the layers grouping, keeping the helicals to hoops ratio and the number of layers unchanged, it can be noticed that both the variables are affected. In particular, a smaller fracture surface will produce emissions of lower amplitude and the

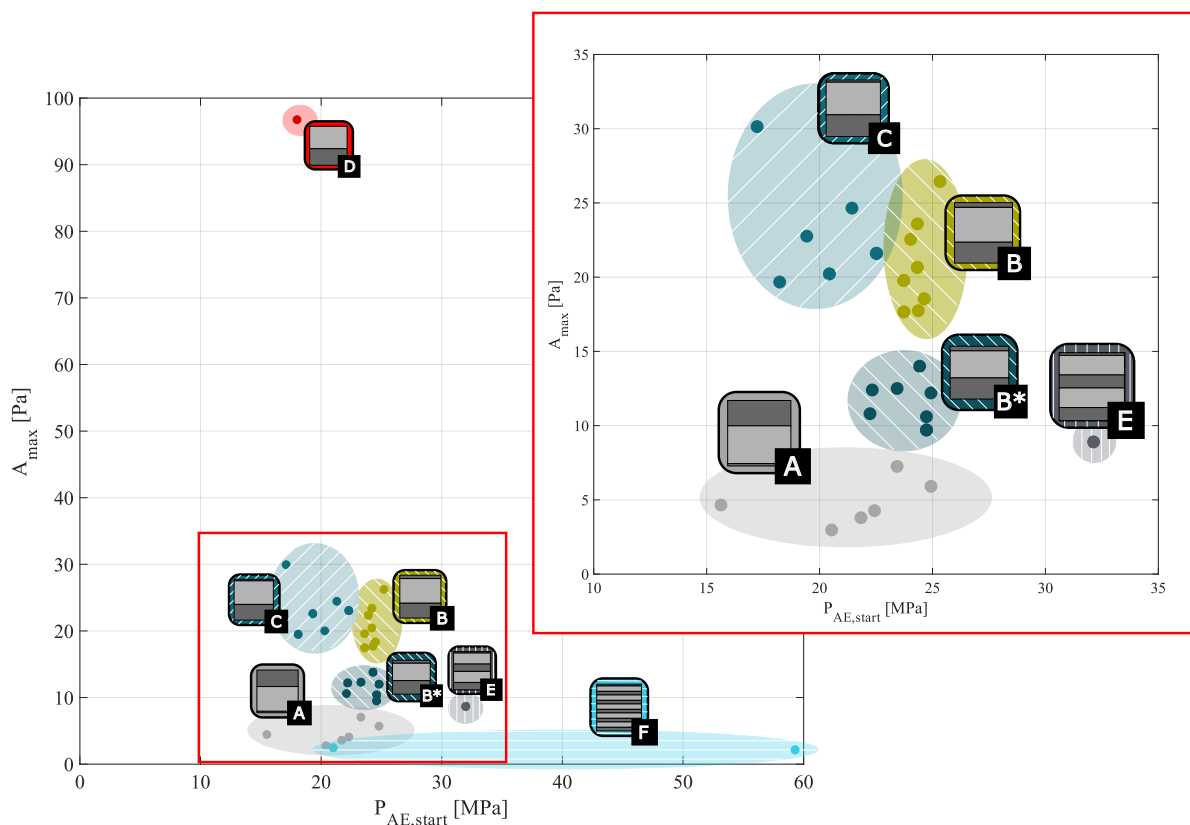


Figure 4.44: A_{max} and $P_{AE,start}$ of the totality of the analyzed vessels.

more groups are present, the later the first emission is detected by the system. It is not clear what causes the latter, but it was speculated that the in situ strength could play at least a side role. This effect is associated to “[...] the varying strength of a ply perpendicular to the fibers” [84]. The thicker these plies are and the lower is their in situ strength. This could lead to a premature crack formation. Nevertheless, if this was the only cause, a similar trend in $P_{AE,start}$ should take place when comparing layups B and B*, which is not the case. It can be concluded that this effect cannot be the only explanation. To explain the delay in detecting the first emission, it was speculated that the innermost block of hoops would have cracked first but due to the limited fracture surface and depth in the laminate, could not produce detectable emissions. For this reason, the first emissions identified are those produced by the outermost block that cracks later. Simulations performed by one colleague in the department showed that the transverse failure index in the hoop layers decreases when moving towards the inside of the laminate, invalidating the hypothesis. It is still not clarified the relation between grouping and the variable $P_{AE,start}$.

One layup that needs a more specific attention is F. It is characterized by emissions of very low amplitude, below 2 Pa. Even when the threshold of the PeakFinder tool is lowered to threshold II only few peaks can be detected. As for the other stacking sequences, it was possible to recognize emissions of higher amplitude (1 to 2 Pa) taking place first and some with amplitudes below 1 Pa taking place later in the pressurization. It was speculated that the emissions with higher amplitude (from 1 to 2 Pa) could correspond to IFF in the hoops. The amplitude of these emissions was consistent with the limited fracture surface due to the presence of only six hoops in each group. The peaks localization showed that they were not located uniquely in the cylindrical section (as it is for the other layups), but the majority of them was in the transition zone. Observing the vessel surface at the pressure stage just after the occurrence of these emissions, few black marks could be detected. It is not clear whether those emissions correspond to IFF in the outer helicals or in the hoops. Analyzing the CT scans of the specimen, this damage mechanism was found in both layers type, thus it could not be uniquely attributed to one of the two. The hypothesis that those emissions come from the hoop layer is reinforced by the CT scans, the emissions amplitude and the pressure of the first detected emission. The only peak above 2 Pa was detected later in the pressurization. This delay is consistent with the trend observed

comparing C and E (with respectively one and two blocks of hoops). When the blocks increase to five, if the pattern is followed, a further delay could be expected. The hypothesis that those emissions correspond to IFF in the outermost helicals is reinforced by the CT scans and the presence of black marks in the transition zone and few in the cylindrical section. The superficial strains calculated from the DIC show that this layup has higher strains in the transition zone. As already explained, the areas with higher superficial strains are those in which superficial IFF is first found. More research on this layup is needed to clarify the topic. It could be beneficial to use different acoustic sensors, such as piezo transducers, directly applied to the surface. With these, the attenuation through the air could be limited and maybe more precise information could be gathered.

One effect that is worth discussing is what takes place in the transition zone of layups B and C at early pressure stages. Some emissions of low amplitudes are localized in the transition zone, which is the area where the lower superficial strains are registered for these laminates. They do not produce visible marks in the chalk layer, thus the emissions must be linked to damage taking place internally. They could be caused by matrix cracking taking place where the hoops are tapered. During curing the circumferential layers can laterally slide due to the applied tension and resin flow, forming small empty spots in between the top and bottom group of helicals. These gaps can get filled by the resin that flows from the dome to the transition zones because of the important compaction effect of the helicals close to the boss. Some resin rich gaps can be created in the transition zone, which could crack at early pressure stages and generate acoustic emissions. Since the cracks are in between the top and bottom group of helicals, they cannot be visually identified. This hypothesis must be still validated.

Another interesting effect that does not follow the discovered pattern regards layup A. As already explained, IFF in the top helicals can be related to the areas with higher strains detected by the DIC. For layup A, the transition zones are the parts most strained of the vessel. No marks can be seen at the end of the pressurization on the chalk even though few emissions of low amplitude can be detected in those areas. It is not clear why this vessel does not follow the pattern, but one hypothesis has been speculated. This takes into account one study that has been investigated in the department. When continuing the pressurization of layup A it was discovered that some spots in the transition zone presented higher strains with respect to the rest of the area. These spots have been analyzed using CT and it was discovered that delaminations between the hoops and helicals were present. This is in agreement with what studied by Szabó [83] when recreating delaminations in composites adding some foils in between the layers. These “delaminations” were detected by the DIC as spots with higher strains. It must be considered that at laminate level, delaminations usually produce emissions with an amplitude in between that of IFF and fiber failure [40, 67, 69, 75]. The emissions detected in the transition zone of layup A are characterized by low amplitudes, which is in disagreement with literature. For this reason, it is not clear whether delaminations are formed later during the pressurization or if they produce emissions with a low amplitude.

5

Conclusion

In this chapter the main conclusions drawn from the investigation will be used to answer the research questions. In the study, a combination of optic and acoustic experimental characterization systems has been used to gain knowledge on the damage formation of CPVs when internally pressurized during a EOL test. It was also studied how different stacking sequences influence the acoustic parameters evaluated. A combination of 3D DIC and delay-and-sum beamforming algorithm have been used for the purpose. A total of seven layups have been analyzed, characterized by different grouping and positioning of the hoop and helical layers. The tests have been performed in a specially designed test chamber. The acoustic emissions have been localized on the vessel and the damage mechanisms have been inspected through CT scans.

1. How is the relation between the depth of interfiber-fracture and the maximum sound pressure amplitude?

Considering IFF that takes place in the hoop layers, the cracks propagate both in-plane (forming a full ring around the vessel) and through the thickness until where a change in layer orientation is encountered. A relation between depth of the damage and maximum sound pressure amplitude recorded has been found. The deeper in the laminate the failure takes place and the lower is the amplitude of the AE. This is caused by the signal attenuation that takes place when layers are located in between the acoustic source and the sensors. For the evaluation, four layups with a single block of 30 hoop layers located at different heights in the vessel have been studied. A slight decrease in amplitude has been encountered when analyzing vessels with respectively one and two helical layers in between IFF and the sensors. The amplitudes registered (averaged between multiple specimens) are respectively 23.65 and 20.69 Pa. When the hoop layers are the outermost plies (with no helicals on top), the maximum recorded amplitude is significantly higher than the other vessels, being 96.76 Pa. This important difference has been attributed to the absence of helicals that attenuate the signal and to the free boundary effect, which results in a high energy release during crack opening. The stacking sequence with the hoops positioned deeper in the laminate and with 10 helicals in between the IFF and the sensors is characterized by the lowest sound pressure amplitude recorded, being an average of 4.61 Pa.

2. How is the maximum sound pressure amplitude affected by the size of the created interfiber-fracture surface?

Considering IFF that takes place in the hoop layers, a relation between fracture surface size and maximum sound pressure amplitude recorded can be found. This fact has been evaluated compared different layups. In one case, layups with the same stacking sequence but a different number of hoop layers (thus also a different number of total plies) have been analyzed. In the second, layups with the same amount of plies but different grouping have been evaluated. For both situations it was concluded that the less circumferential plies are stacked together and the lower is the amplitude of the AEs recorded. It was noticed that when removing seven hoops (from 30 to 23) the maximum amplitude decreased from 20.69 to 11.50 Pa. When considering the second scenario, it was shown that when having only 15 circumferentials in one group, the sound pressure amplitude further decreased, up to 8.70 Pa. When considering the layup characterized by five groups of six hoops each, the maximum recorded amplitude (in average) was 1.59 Pa. It was not clear whether the AEs analyzed in the latter layup were caused by IFF located in the hoop or in the top helical

layers. One characteristic that was similar in all the stacking sequences analyzed was the presence of IFF in the outermost helicals. This damage is characterized by emissions of low amplitude (usually below 2 Pa). This can be associated to the limited size of the fracture surface. Since the helical layers are wound as cross-ply, the damage cannot grow through the thickness. The growth is also limited in-plane due to layers overlapping and changes in orientation.

- **How can acoustic features (e.g. maximum sound pressure amplitude) be associated to certain layup characteristics during an EOL pressurization of a CPV?**

When performing the first pressurization, the maximum sound pressure amplitude recorded in the pressure range 5-105 MPa provides information regarding the positioning and grouping of the hoop layers. A high amplitude can be related to the presence of a single block with a significant amount of hoops, located superficially in the laminate. A lower amplitude can be related to either a single block positioned deeper in the laminate or to blocks with less circumferentials. Another variable that can help to identify the layups is $P_{AE,start}$, which is defined as the internal pressure at which the first emission above 2 Pa is recorded. This can be related to the grouping of the layers and its value is higher when the plies are divided in more groups. A slight difference is encountered when considering layups with respectively zero, one and two helicals above the single block of hoops. It was concluded that the more helicals were positioned on top of the hoops and the higher was $P_{AE,start}$. This has been linked to the constraining effect of the top helicals for IFF formation in the hoops. This trend is not followed when the external helicals are 10. It is also shown that these parameters, together with N_{hits} (the number of peaks above 2Pa detected by the PeakFinder tool) are layup-specific. This is valid for all the examined stacking sequences except F, which is characterized by five blocks of six hoops, separated by helicals. The peaks emitted by this layup are, in the majority of the cases, not detectable with the current systems. This because their amplitude is lower than the predefined thresholds, which leads to significant standard deviations in the results. It can be concluded that the layups under investigation can be differentiated based on the acoustics parameters evaluated.

- **To which extent is it possible to characterize or differentiate damage mechanisms through the combination of delay-and-sum beamforming and DIC?**

During an EOL pressurization of seven different layups, it was possible to identify only one damage mechanism: IFF. Some differences could be observed according to the location in which it was taking place. IFF in the hoop layers causes emissions of higher amplitude, with differences according to circumferentials positioning and grouping in the laminate. IFF in the outer helicals is characterized by emissions with low amplitudes, usually below 1 Pa. When IFF takes place, it is always detectable with the delay-and-sum beamforming algorithm used and the post-processing tools used (with some exceptions for layup F). It is possible to use the post-processed data to understand to which stacking sequence (of the pre-examined ones), the vessel belongs to. It can be concluded that delay-and sum beamforming is suitable for damage characterization but it is not clear whether it can be used for differentiation. Nothing can be concluded regarding other damage mechanisms (such as delaminations or fiber failure), because they did not take place in the studied pressure range (5-105 MPa). On the other hand, DIC has been found to have a limited suitability for damage characterization and differentiation. With the use of DIC only, it was not possible to detect and localize IFF in the hoop layers, unless they were the most external ones. Nevertheless, tracking the axial displacement of the top boss, it was possible to evaluate some residual displacement after complete depressurization, which has been linked to this type of damage. Considering IFF taking place in the outermost helical layer, it was not possible to visualize it. This could be caused by the limited size of the related fracture with respect to the system resolution. The calculated superficial strain distributions could be used to understand in which vessel areas this damage would take place first (where the highest strains are computed). It has been shown that DIC is a suitable method to evaluate the most critical areas of the vessel and could give information regarding the formation of delaminations. The latter fact has not been proven in the current investigation, but in other projects taking place in the department. It can be concluded that the combination of DIC and delay-and-sum beamforming can provide clear information regarding the vessel state during an EOL pressurization test and can be considered suitable for the purpose.

6

Future Work

During the current investigation, new questions arose which could form the basis for future researches. The automation of the process could also be beneficial to speed up the analysis and make it user-independent. The topics and ideas developed are presented in the following list in form of questions.

1. Which emissions of layup F are associated with IFF in the hoops and which in the superficial helicals?

This is one of the unsolved questions of the current project. The emissions of layup F are characterized by low amplitudes, mainly below 2 Pa which detectability is highly dependent on the set threshold and on the acoustic system used. In this layup, only a limited amount of peaks have been detected and it was not possible to distinguish those associated to IFF in the hoops and those in the top helicals. To answer the question, it could be necessary to use more sensitive acoustic sensors, such as piezo electric sensors during the pressurization. Another option could be to use the same testing chamber and equipment but perform a stepped pressurization. This means to pressurize the vessel up to a certain level and depressurize it afterwards. Post-processing the acoustic data and performing a CT scan at each step is also needed. The acoustic data recorded at each step should be analyzed and it must be tried to associate it to the detected damage. Then, the same vessel should be pressurized up to a higher pressure stage and the process repeated. This could help to study the damage formation. It must be taken into account that the scan of the full specimen might not provide the needed resolution. In this case, multiple scans of smaller areas could be performed.

2. Layups B and C had the peculiarity to present some AEs of low amplitude localized in the transition zones at early pressure stages without showing any superficial damage. Can these emissions be associated to matrix cracking in the resin rich gaps present in the hoops tapering?

In the current research it was not verified whether the hypothesis is correct or not. Answering this question would lead to a better understanding of the damage mechanisms taking place in the vessels with these stacking sequences. The hypothesis could be proven cutting the transition zone of the tested layups B or C where the tapering is present and the emissions have been localized. CT scans should be performed afterwards. However, it might be not trivial to identify the failure mechanism, since multiple damages could be found. It might be beneficial to wind another vessel and pressurize it only up to 50 MPa. At this stage matrix cracking in the superficial helicals should have not taken place yet, thus the identification could be clearer. CT scans must be performed to verify the hypothesis that those emissions can be associated to cracks taking place in the resin rich gap, formed during curing. The scans can be used to also verify the slippage of the circumferential layers due to resin flow in the curing phase.

3. From the investigation it seemed that a trend was present between $P_{AE,start}$ and the hoops grouping. Can this trend be confirmed or invalidated?

During the investigation it was noticed that the more groups of hoops were present in the laminate and the later during the pressurization the first emission was detected. However, this pattern could not be clearly proven because only one vessel of layup E has been analyzed and because the data of layup F were highly dependent on the selected thresholds. Other two vessels of layup E (at least) should be manufactured and tested to provide more reliable results. In addition, it might be beneficial to manufacture some vessels of

a new layup with layers grouping in between E and F. It could have, for example, three blocks of 10 hoops each separated by blocks of three helicals. This layup should produce detectable emissions that should not be highly dependent on the set threshold as for layup F. These vessels should be pressurized up to 105 MPa and the data post-processed with the current tools. It could then be verified whether $P_{AE,start}$ is higher than that of E. Answering this question could provide a better understand of IFF formation in stacking sequences in which multiple groups of hoops and helicals are alternated.

4. Can damage mechanisms other than IFF be detected and differentiated using delay-and-sum beamforming and DIC?

Determining the acoustic and optic characteristics of other damage mechanisms would increase the knowledge on damage formation and progression in CPVs. Understanding the characteristics of severe damages such as delaminations and fiber failure could make their detectability easier during a pressurization. This could help to understand whether a vessel should be quality assured or discarded, due to potential safety issues. Knowledge on this topic could be obtained pressurizing the stacking sequences evaluated in the current investigation up to higher pressure stages. They could potentially present other damage mechanisms and their optic and acoustic characteristics should be recorded and post-processed with the tools used during the project.

5. Can manufacturing defects be recognized by the current systems?

This topic could be particularly beneficial in case mass-production is implemented and the manufacturing of each vessel cannot be constantly monitored by the operators. This investigation can be performed implementing manufacturing defects in the structure. The vessels must then be pressurized and it must be studied whether these defects could be identified using DIC and delay-and-sum beamforming.

6. How would the variables studied in the current project (A_{max} , $P_{AE,start}$, etc.) be affected if another or multiple winding angles are chosen for the helicals?

It might be the case that the vessels would require the helicals wound at an angle different from $\pm 19.9^\circ$ or even with multiple winding angles. It is necessary to study how the characteristics of IFF and other damage mechanisms are affected by this factor. Vessels with different winding angles of the helicals must be manufactured and tested. The optic and acoustic data must be post-processed with the tools used during the current project and compared with the present data. This would extend the knowledge gained with the current thesis.

7. Can the vessel preparation for the DIC be faster? Are there more efficient methods to apply the speckled pattern on the vessel?

The speckling of the vessel to perform DIC is one of the most time-consuming activities, which requires up to one hour for the researcher for a single vessel. It might be beneficial to study whether other methods can provide an accurate pattern, requiring less time. An example could be to replace the brush used for applying the black paint with a spray. A plastic foil in which small holes in random positions are carved must also be used. The foil could be taped to the vessel surface and sprayed with the black paint. Then it could be removed and used for multiple vessels. The preparation of such foil could require an extensive effort and precision and thus time. However, this could be beneficial when multiple vessels need to be tested, reducing the preparation time. The pattern created with this method must be checked using the GOM software and in particular the "Pattern Quality" tool.

8. Can the AEs localization process be speed up?

This is the most time-consuming and user dependent part of each test. Each emission requires up to three minutes of post-processing considering the vessel mesh loading, the beamforming and the saving process. For a vessel like C in which 246 emissions are beamformed, the localization could need up to 12 hours which means one and half or two working days. If the pressurization is continued up to burst, even more events will be detected and more time is needed just for this step. If multiple vessels of multiple stacking sequences are analyzed, many working weeks must be dedicated for this purpose. For this reason, it is beneficial to automate the process or at least some parts of it such as the mesh import and resizing. A MATLAB code could be implemented to perform the beamforming, even though this part is highly user-dependent. In fact, different time intervals must be selected according to the type of emission.

9. Can other features of the AE (such as frequency, rise time, duration, energy, count, etc.) help in the damage differentiation process? How are these parameters affected by the different damage mechanisms and stacking sequences?

Analyzing multiple AE features could improve the damage differentiation process. The different variables could be simultaneously monitored implementing a clustering algorithm. The characteristics of each damage mechanisms can be identified in a clearer way. This process could be done following the same steps performed during the current research but analyzing not only the amplitude of the emissions. To obtain those, multiple MATLAB code might be needed. A clustering algorithm can automatically associate the acoustic emissions of a vessel with the occurring damage mechanisms. The gained knowledge could also be used to implement a neural network that can take into account all the variables (damage mechanisms, defects, stacking sequence, etc.).

Bibliography

- [1] Regulation (eu) 2019/ 631 of the european parliament and of the council - of 17 april 2019 - setting co2 emission performance standards for new passenger cars and for new light commercial vehicles, and repealing regulations (ec) no 443 / 2009 and (eu) no 510 / 2011.
- [2] B. G. Pollet, S. S. Kocha, and I. Staffell. Current status of automotive fuel cells for sustainable transport. *Current Opinion in Electrochemistry*, 16:90–95, 2019. ISSN 24519103. doi: 10.1016/j.coelec.2019.04.021.
- [3] S. Carley, R.M. Krause, B.W. Lane, and J.D. Graham. Intent to purchase a plug-in electric vehicle: A survey of early impressions in large us cities. *Transportation Research Part D: Transport and Environment*, 18: 39–45, 2013. ISSN 13619209. doi: 10.1016/j.trd.2012.09.007.
- [4] C.E. Thomas. Fuel cell and battery electric vehicles compared. *International Journal of Hydrogen Energy*, 34(15):6005–6020, 2009. ISSN 03603199. doi: 10.1016/j.ijhydene.2009.06.003.
- [5] I. Staffell, D. Scamman, A. V. Abad, P. Balcombe, P. E. Dodds, P. Ekins, N. Shah, and K. R. Ward. The role of hydrogen and fuel cells in the global energy system. *Energy & Environmental Science*, 12(2):463–491, 2019. ISSN 1754-5692. doi: 10.1039/C8EE01157E.
- [6] A. R. Bunsell and A. Thionnet. Health monitoring of high performance composite pressure vessels. In *Comprehensive Composite Materials II*, pages 420–430. Elsevier, 2018. ISBN 9780081005347. doi: 10.1016/B978-0-12-803581-8.10041-4.
- [7] EU 406/2010. Commission regulation (eu) no 406/2010 of 26 april 2010 implementing regulation (ec) no 79/2009 of the european parliament and of the council on type-approval of hydrogen-powered motor vehicles.
- [8] M. Nebe, C. Braun, T. Gebhardt, D. Hülbusch, and F. Walther. Combining optical and acoustical characterization methods to investigate damage and failure mechanisms in composite pressure vessels. *ICFC 7 - the 7th International Conference of Fatigue of Composites*, 2018.
- [9] C.P. Fowler, A.C. Orifici, and C.H. Wang. A review of toroidal composite pressure vessel optimisation and damage tolerant design for high pressure gaseous fuel storage. *International Journal of Hydrogen Energy*, 41(47):22067–22089, 2016. ISSN 03603199. doi: 10.1016/j.ijhydene.2016.10.039.
- [10] H. Barthelemy, M. Weber, and F. Barbier. Hydrogen storage: Recent improvements and industrial perspectives. *International Journal of Hydrogen Energy*, 42(11):7254–7262, 2017. ISSN 03603199. doi: 10.1016/j.ijhydene.2016.03.178.
- [11] G. W. Mair. *Safety Assessment of Composite Cylinders for Gas Storage by Statistical Methods: Potential for Design Optimisation Beyond Limits of Current Regulations and Standards*. Springer International Publishing, Cham, 2017. ISBN 9783319497082. doi: 10.1007/978-3-319-49710-5. URL <http://dx.doi.org/10.1007/978-3-319-49710-5>.
- [12] L. Parnas and N. Katirci. Design of fiber-reinforced composite pressure vessels under various loading conditions. *Composite Structures*, 58(1):83–95, 2002. ISSN 02638223. doi: 10.1016/S0263-8223(02)00037-5.
- [13] M. Quanjin, M.M. Rejab, I.M. Sahat, M. Amiruddin, D. Bachtiar, J.P. Siregar, and M.I. Ibrahim. Design of portable 3-axis filament winding machine with inexpensive control system. *JOURNAL OF MECHANICAL ENGINEERING AND SCIENCES*, 12(1):3479–3493, 2018. ISSN 22894659. doi: 10.15282/jmes.12.1.2018.15.0309.
- [14] F.W. DuVall. Cost comparisons of wet filament winding versus prepreg filament winding for type ii and type iv cng cylinders. *SAMPE JOURNAL*, 37(1):38–42, 2001.

- [15] J. Rousseau, D. Perreux, and N. Verdière. The influence of winding patterns on the damage behaviour of filament-wound pipes. *Composites Science and Technology*, 59(9):1439–1449, 1999. ISSN 02663538. doi: 10.1016/S0266-3538(98)00184-5.
- [16] M. Lossie and H. van Brussel. Design principles in filament winding. *Composites Manufacturing*, 5(1): 5–13, 1994. ISSN 09567143. doi: 10.1016/0956-7143(94)90014-0.
- [17] L. Zu, S. Koussios, and A. Beukers. Design of filament-wound domes based on continuum theory and non-geodesic roving trajectories. *Composites Part A: Applied Science and Manufacturing*, 41(9):1312–1320, 2010. doi: 10.1016/j.compositesa.2010.05.015.
- [18] S. Koussios, O.K. Bergsma, and G. Mitchell. Non-geodesic filament winding on generic shells of revolution. *Proceedings of the Institution of Mechanical Engineers, Part L: Journal of Materials: Design and Applications*, 219(1):25–35, 2005. ISSN 1464-4207. doi: 10.1243/146442005X10184.
- [19] N. Akkus and G. Genk. Influence of pretension on mechanical properties of carbon fiber in the filament winding process. *The International Journal of Advanced Manufacturing Technology*, 91(9-12):3583–3589, 2017. ISSN 0268-3768. doi: 10.1007/s00170-017-0049-z.
- [20] C.C. Chan. The state of the art of electric, hybrid, and fuel cell vehicles. *Proceedings of the IEEE*, 95(4): 704–718, 2007. ISSN 0018-9219. doi: 10.1109/JPROC.2007.892489.
- [21] A. Kirubakaran, S. Jain, and R.K. Nema. A review on fuel cell technologies and power electronic interface. *Renewable and Sustainable Energy Reviews*, 13(9):2430–2440, 2009. ISSN 13640321. doi: 10.1016/j.rser.2009.04.004.
- [22] J. Franzen, S. Maus, and P. Potzel. Hydrogen storage in vehicles. In Detlef Stolten and Bernd Emonts, editors, *Hydrogen Science and Engineering*, pages 881–901. John Wiley & Sons, Incorporated, Berlin, GERMANY, 2016. ISBN 9783527674299.
- [23] B.W. Tew. Preliminary design of tubular composite structures using netting theory and composite degradation factors. *Journal of Pressure Vessel Technology*, 117, 1995. doi: 10.1115/1.2842141.
- [24] K. Magnucki, W. Szyk, and J. Lewiński. Minimization of stress concentration factor in cylindrical pressure vessels with ellipsoidal heads. *International Journal of Pressure Vessels and Piping*, 79(12):841–846, 2002. ISSN 03080161. doi: 10.1016/S0308-0161(02)00101-1.
- [25] P. Balicevic, D. Kozak, and T. Mrcela. Strength of pressure vessels with ellipsoidal heads. *Journal of Mechanical Engineering*, 54(10):685–692, 2008.
- [26] M. Madhavi. Design and analysis of filament wound composite pressure vessel with integrated-end domes. *Defence Science Journal*, 59(1):73–81, 2009. doi: 10.14429/dsj.59.1488.
- [27] M. Xia, H. Takayanagi, and K. Kemmochi. Analysis of multi-layered filament-wound composite pipes under internal pressure. *Composite Structures*, 53(4):483–491, 2001. ISSN 02638223. doi: 10.1016/S0263-8223(01)00061-7.
- [28] R. Talreja and C. Veer Singh. *Damage and Failure of Composite Materials*. Cambridge University Press, 2012. ISBN 978-0-521-81942-8 Hardback.
- [29] S.L. Ogin, P. Brøndsted, and J. Zangenberg. Composite materials. In *Modeling Damage, Fatigue and Failure of Composite Materials*, pages 3–23. Elsevier, 2016. ISBN 9781782422860. doi: 10.1016/B978-1-78242-286-0.00001-7.
- [30] M. Sause. *In situ monitoring of fiber-reinforced composites: Theory, basic concepts, methods, and applications*, volume 242 of *Springer Series in Materials Science*. Springer International Publishing, Cham, 2016. ISBN 9783319309538. doi: 10.1007/978-3-319-30954-5. URL <http://dx.doi.org/10.1007/978-3-319-30954-5>.
- [31] C. Kassapoglou. *Modeling the Effect of Damage in Composite Structures // Modeling the effect of damage in composite structures: Simplified approaches*. Aerospace Series List. Wiley, s.l., 2015. ISBN 9781119013211.

- [32] C. Li, F. Ellyin, and A. Wharmby. On matrix crack saturation in composite laminates. *Composites Part B: Engineering*, 34(5):473–480, 2003. ISSN 13598368. doi: 10.1016/S1359-8368(03)00020-9.
- [33] A. Afzaluddin, M. Jawaid, S. Mohd Salit, and M.R. Ishak. Physical and mechanical properties of sugar palm/glass fiber reinforced thermoplastic polyurethane hybrid composites. *Journal of Materials Research and Technology*, 8(1):950–959, 2019. ISSN 22387854. doi: 10.1016/j.jmrt.2018.04.024.
- [34] S. Carmignato, W. Dewulf, and R. Leach. *Industrial x-ray computed tomography*. Springer, Cham, 2018. ISBN 978-3-319-59571-9.
- [35] G.N. Hounsfield. Computerized transverse axial scanning (tomography): Part i. description of system. *British Journal of Radiology*, 46:1016–1022, 1973.
- [36] H.E. Martz, S.G. Azevedo, J.M. Brase, K.E. Waltjen, and D.J. Schneberk. Computed tomography systems and thier industrials applications. *International Journal of Radiation Applications and Instrumentation. Part A. Applied Radiation and Isotopes*, 41 (10-11):943–961, 1990.
- [37] A.E. Scott, M. Mavrogordato, P. Wright, I. Sinclair, and S.M. Spearing. In situ fibre fracture measurement in carbon–epoxy laminates using high resolution computed tomography. *Composites Science and Technology*, 71(12):1471–1477, 2011. ISSN 02663538. doi: 10.1016/j.compscitech.2011.06.004.
- [38] V. Crupi, G. Epasto, and E. Guglielmino. Computed tomography analysis of damage in composites subjected to impact loading. *Frattura ed Integrità Strutturale*, 5(17):32–41, 2011. ISSN 19718993. doi: 10.3221/IGF-ESIS.17.04.
- [39] A. Djabali, L. Toubal, R. Zitoune, and S. Rechak. An experimental investigation of the mechanical behavior and damage of thick laminated carbon/epoxy composite. *Composite Structures*, 184:178–190, 2018. ISSN 02638223. doi: 10.1016/j.compstruct.2017.09.069.
- [40] A. Djabali, L. Toubal, R. Zitoune, and S. Rechak. Fatigue damage evolution in thick composite laminates: Combination of x-ray tomography, acoustic emission and digital image correlation. *Composites Science and Technology*, 183:107815, 2019. ISSN 02663538. doi: 10.1016/j.compscitech.2019.107815.
- [41] P.A. Jolly, B. Sturzu, K. Hollstein, R. Singh, S. Thomas, P. Foote, and A. Shaw. Review of non-destructive testing (ndt) techniques and their applicability to thick walled composites. *Procedia CIRP*, 38:129–136, 2015. ISSN 22128271. doi: 10.1016/j.procir.2015.07.043.
- [42] A.I. Torres Guijarro. *Experimental and Analytical Determination of Interfiber Fracture Mechanisms and Patterns in Type IV Composite Pressure Vessels*. PhD thesis, Tu Delft, Delft, the Netherlands, July/2019.
- [43] D.H. Kang, C.U. Kim, and C.G. Kim. The embedment of fiber bragg grating sensors into filament wound pressure tanks considering multiplexing. *NDT & E International*, 39(2):109–116, 2006. ISSN 09638695. doi: 10.1016/j.ndteint.2005.07.013.
- [44] J. Degrieck, W. de Waele, and P. Verleysen. Monitoring of fibre reinforced composites with embedded optical fibre bragg sensors, with application to filament wound pressure vessels. *NDT & E International*, 34(4):289–296, 2001. ISSN 09638695. doi: 10.1016/S0963-8695(00)00069-4.
- [45] J.-C. Hao, J.-S. Leng, and Z. Wei. Non-destructive evaluation of composite pressure vessel by using fbg sensors. *Chinese Journal of Aeronautics*, 20(2):120–123, 2007. ISSN 10009361. doi: 10.1016/S1000-9361(07)60017-X.
- [46] X.F. Yao, L.B. Meng, J.C. Jin, and H.Y. Yeh. Full-field deformation measurement of fiber composite pressure vessel using digital speckle correlation method. *Polymer Testing*, 24(2):245–251, 2005. ISSN 01429418. doi: 10.1016/j.polymertesting.2004.05.009.
- [47] L.B. Meng, G.C. Jin, X.F. Yao, and H.Y. Yeh. 3d full-field deformation monitoring of fiber composite pressure vessel using 3d digital speckle correlation method. *Polymer Testing*, 25(1):42–48, 2006. ISSN 01429418. doi: 10.1016/j.polymertesting.2005.09.011.
- [48] M.A. Sutton, J. Orteu, and H.W. Schreier. *Image correlation for shape, motion and deformation measurements: Basic concepts, theory and applications*. Springer, New York N.Y., 2009. ISBN 9780387787473.

- [49] M.A. Sutton, W.J. Wolters, W.H. Peters, W.F. Ranson, and S.R. McNeill. Determination of displacements using an improved digital correlation method. *image and vision computing*, 1.3:133–139, 1983.
- [50] S. Geller, K. Holeczek, A. Winkler, T. Tyczynski, T. Weber, M. Gude, and N. Modler. Multiscale characterization and testing of function-integrative fiber-reinforced composites. In *Performance Testing of Textiles*, pages 155–176. Elsevier, 2016. ISBN 9780081005705. doi: 10.1016/B978-0-08-100570-5.00008-6.
- [51] GOM GmbH. Gom testing: Technical documentation as of v8 sr1: Digital image correlation and strain computation basics.
- [52] Y.H. Huang, L. Liu, F.C. Sham, Y.S. Chan, and S.P. Ng. Optical strain gauge vs. traditional strain gauges for concrete elasticity modulus determination. *Optik*, 121(18):1635–1641, 2010. ISSN 00304026. doi: 10.1016/j.ijleo.2009.03.002.
- [53] L.D. Rodrigues, J.L.F. Freire, R.D. Vieira, and J.T.P. Castro. Strain analysis of thin pipe pressure vessels using digital image correlation. *Journal of Mechanical Engineering and Automation*, 4(2):63–72, 2014. URL <http://article.sapub.org/10.5923.j.jmea.20140402.03.html#Ref>.
- [54] P. Gąsior, M. Malesa, J. Kaleta, M. Kujawińska, K. Malowany, and R. Rybczyński. Application of complementary optical methods for strain investigation in composite high pressure vessel. *Composite Structures*, 203:718–724, 2018. ISSN 02638223. doi: 10.1016/j.compstruct.2018.07.060.
- [55] F.E. Oz, N. Ersoy, and S.V. Lomov, editors. *In-situ damage monitoring and correlation with acoustic emission in CFRP composites*, 2017.
- [56] J.K. Burnett. *Theory and uses of acoustic emissions*. Materials science and technologies. Nova Science Publishers, New York, 2011. ISBN 1612099602.
- [57] ASTM E1316-01. Standard terminology for nondestructive examinations, 2002.
- [58] F. Dahmene, S. Yaacoubi, and M. E. L. Mountassir. Acoustic emission of composites structures: Story, success, and challenges. *Physics Procedia*, 70:599–603, 2015. ISSN 18753892. doi: 10.1016/j.phpro.2015.08.031.
- [59] A.K. Rao. Acoustic emission and signal analysis. *Defence Science Journal*, 40(1):55–70, 1990.
- [60] A. Bravo, L. Toubal, D. Koffi, and F. Erchiqui. Characterization of tensile damage for a short birch fiber-reinforced polyethylene composite with acoustic emission. *International Journal of Material Science (IJMSCI)*, 3(3):79–89, 2013.
- [61] R. Unnorsson. Hit detection and determination in ae bursts. In W. Sikorski, editor, *Acoustic Emission - Research and Applications*. InTech, 2013. ISBN 978-953-51-1015-6. doi: 10.5772/54754.
- [62] C.U. Grosse and M. Ohtsu. *Acoustic emission testing*. Springer, Berlin and London, 2008. ISBN 978-3-540-69895-1.
- [63] D. Valentin, P. Bonniau, and A.R. Bunsell. Failure mechanism discrimination in carbon fibre-reinforced epoxy composites. *Composites*, 14(4):345–351, 1983. ISSN 00104361. doi: 10.1016/0010-4361(83)90153-2.
- [64] J.M. Berthelot and J. Rhazi. Acoustic emission in carbon fibre composites. *Composites Science and Technology*, 37(4):411–428, 1990. ISSN 02663538. doi: 10.1016/0266-3538(90)90012-T.
- [65] S. Barré and M.L. Benzeggagh. On the use of acoustic emission to investigate damage mechanisms in glass-fibre-reinforced polypropylene. *Composites Science and Technology*, 52(3):369–376, 1994. ISSN 02663538. doi: 10.1016/0266-3538(94)90171-6.
- [66] S.-T. Kim and Y.-T. Lee. Characteristics of damage and fracture process of carbon fiber reinforced plastic under loading-unloading test by using ae method. *Materials Science and Engineering: A*, 234-236:322–326, 1997. ISSN 09215093. doi: 10.1016/S0921-5093(97)00226-8.

- [67] X. Zhuang and X. Yan. Investigation of damage mechanisms in self-reinforced polyethylene composites by acoustic emission. *Composites Science and Technology*, 66(3-4):444–449, 2006. ISSN 02663538. doi: 10.1016/j.compscitech.2005.07.013.
- [68] W.H. Prosser. Advanced ae techniques in composite materials research. *Journal of Acoustic Emission*, 14:1–11, 1996.
- [69] P.F. Liu, J.K. Chu, Y. Liu, and J.Y. Zheng. A study on the failure mechanisms of carbon fiber/epoxy composite laminates using acoustic emission. *Materials & Design*, 37:228–235, 2012. ISSN 02613069. doi: 10.1016/j.matdes.2011.12.015.
- [70] S.S. Russel and E.G. Henneke. Signature analysis of acoustic emission from graphite/epoxy composites. URL <https://ntrs.nasa.gov/search.jsp?R=19770023235>.
- [71] M. Suzuki, H. Nakanishi, M. Iwamoto, and E. Jinen. Application of static fracture mechanisms to fatigue fracture behavior of class a-smc composite. *Proceeding of the 4th Japan-US Conference on Composite Materials*, S., pages 297–306, 1988.
- [72] P.J. de Groot, P.A.M. Wijnen, and R.B.F. Janssen. Real-time frequency determination of acoustic emission for different fracture mechanisms in carbon/epoxy composites. *Composites Science and Technology*, 55(4):405–412, 1995. ISSN 02663538. doi: 10.1016/0266-3538(95)00121-2.
- [73] C.R. Ramirez-Jimenez, N. Papadakis, N. Reynolds, T.H. Gan, P. Purnell, and M. Pharaoh. Identification of failure modes in glass/polypropylene composites by means of the primary frequency content of the acoustic emission event. *Composites Science and Technology*, 64(12):1819–1827, 2004. ISSN 02663538. doi: 10.1016/j.compscitech.2004.01.008.
- [74] S. Huguet, N. Godin, R. Gaertner, L. Salmon, and D. Villard. Use of acoustic emission to identify damage modes in glass fibre reinforced polyester. *Composites Science and Technology*, 62(10-11):1433–1444, 2002. ISSN 02663538. doi: 10.1016/S0266-3538(02)00087-8.
- [75] N. Godin, S. Huguet, and R. Gaertner. Integration of the kohonen's self-organising map and k-means algorithm for the segmentation of the ae data collected during tensile tests on cross-ply composites. *NDT & E International*, 38(4):299–309, 2005. ISSN 09638695. doi: 10.1016/j.ndteint.2004.09.006.
- [76] R. Gutkin, C. J. Green, S. Vangrattanachai, S. T. Pinho, P. Robinson, and P. T. Curtis. On acoustic emission for failure investigation in cfrp: Pattern recognition and peak frequency analyses. *Mechanical Systems and Signal Processing*, 25(4):1393–1407, 2011. ISSN 08883270. doi: 10.1016/j.ymsp.2010.11.014.
- [77] A. Marec, J.-H. Thomas, and R. El Guerjouma. Damage characterization of polymer-based composite materials: Multivariable analysis and wavelet transform for clustering acoustic emission data. *Mechanical Systems and Signal Processing*, 22(6):1441–1464, 2008. ISSN 08883270. doi: 10.1016/j.ymsp.2007.11.029.
- [78] *Practical acoustic emission testing*. Springer, Tokyo, 2016. ISBN 978-4-431-55071-6.
- [79] B.B. Liao, D.L. Wang, M. Hamdi, J.Y. Zheng, P. Jiang, C.H. Gu, and W.R. Hong. Acoustic emission-based damage characterization of 70 mpa type iv hydrogen composite pressure vessels during hydraulic tests. *International Journal of Hydrogen Energy*, 2019. ISSN 03603199. doi: 10.1016/j.ijhydene.2019.02.217. URL <http://www.sciencedirect.com/science/article/pii/S0360319919308791>.
- [80] D. Döbler and G. Heilmann. Perspectives of the acoustic camera. *Internoise - The 2005 Congress and Exposition on Noise Control Engineering*, 2005.
- [81] M. Navvab, G. Heilmann, and A. Meyer. Simulation, visualization and perception of sound in a virtual environment using beamforming. *Berlin Beamforming Conference*, 2012.
- [82] F. E. Oz, N. Ersoy, and S. V. Lomov. Do high frequency acoustic emission events always represent fibre failure in cfrp laminates? *Composites Part A: Applied Science and Manufacturing*, 103:230–235, 2017. doi: 10.1016/j.compositesa.2017.10.013.

-
- [83] G. Szabényi and V. Hliva. Detection of delamination in polymer composites by digital image correlation-experimental test. *Polymers*, 11(3), 2019. doi: 10.3390/polym11030523.
- [84] C. Kassapoglou. *Design and analysis of composite structures: With applications to aerospace structures*. AIAA education series. b John Wiley & Sons and American Institute of Aeronautics and Astronautics, Reston Va. and United Kingdom, 1st ed. edition, 2010. ISBN 9781600867804.